

MECHANISMS FOR TRANSITION TO
TURBULENCE IN THE BOTTOM BOUNDARY
LAYER UNDER A SURFACE SOLITARY WAVE

A Dissertation

Presented to the Faculty of the Graduate School

of Cornell University

in Partial Fulfillment of the Requirements for the Degree of

Doctor of Philosophy

by

Mahmoud Mostafa kamel Saad Sadek

August 2015

© 2015 Mahmoud Mostafa kamel Saad Sadek

ALL RIGHTS RESERVED

MECHANISMS FOR TRANSITION TO TURBULENCE IN THE BOTTOM
BOUNDARY LAYER UNDER A SURFACE SOLITARY WAVE

Mahmoud Mostafa kamel Saad Sadek, Ph.D.

Cornell University 2015

Transition mechanisms to turbulence in the unsteady bottom boundary layer (BBL) driven by a soliton-like pressure gradient in an oscillating water tunnel (an approximation for the BBL under surface solitary waves) are investigated in a hydrodynamic instability context. This investigation aims to establish connections across theoretical and numerical analysis and the experimental findings of Sumer et al., 2010 (J. Fluid Mech. vol. 646, 2010,p. 207). Transition to turbulence in the surface solitary wave-driven BBL can take place according to two different scenarios. The primary scenario is associated with the classical transition resulting from the breakdown of the exponentially growing 2-D Tollmien-Schlichting waves. The alternative scenario consists of a characteristically different path to transition resulting from the formation of localized turbulent spots. The formation of these turbulent spots, which are the manifestation of an algebraic growth of infinite streamwise disturbance, i.e., zero streamwise wave number, leads to a bypass transition to turbulence.

In regards to the first scenario, a detailed map for the temporal instability is established. Both linear stability analysis and fully nonlinear two- and three-dimensional simulations using high-order numerical methods have been carried out. The process of delineation of the stability regions as a function of boundary layer thickness-based Reynolds number of the temporally evolving base flow, Re_δ consists of two parts. The first part aims to assess the lower limit

of the Re_δ range within which the standard, quasi-steady, linear stability analysis is applicable as it considers individual profiles sampled during the base flow transient evolution. Below this limit, transient linear stability analysis serves as a more accurate predictor of the stability properties of the base flow.

In the second step, above the Re_δ limit where the BBL is determined to be linearly unstable, the base flow is further classified as unconditionally stable, conditionally unstable or unconditionally unstable in terms of its sensitivity to the amplitude and the insertion time of perturbations. Two distinct modes of instability exist in this case: post- and pre-flow-reversal modes. At a moderate value of Re_δ , both modes are first observed in the wave deceleration phase. The post flow reversal mode dominates for relatively low Re and it is the one observed in Sumer *et al.* (*J. Fluid Mech.* vol. 646, 2010, p. 207). For Re above a threshold value of the base flow in the unconditionally unstable regime, the pre-flow reversal mode, which has a larger wavelength than its post-reversal counterpart, becomes dominant. In the same regime, the threshold Re_δ value above which instability is observed in the acceleration phase of the wave is also identified. In this case, the base flow velocity profiles lack any inflection point, suggesting that the origin of such an instability is viscous. Finally, the lower Re_δ limit above which quasi-steady linear stability analysis is valid may be independently obtained by adapting to the surface solitary wave BBL framework an instability criterion which links the average growth rate and wave event timescale, as previously proposed in studies of the instability of the interior of progressive and solitary internal waves. This part of the study is a recap to what have been published by Sadek *et al.* (2015).

For the second transition scenario, the linear stability analysis is reformulated in the non-modal framework where the three-dimensional nature of the

base flow is considered. By doing such a reformulation, an optimum initial disturbance is identified. Such a disturbance can lead to very large short-term energy growth that can not be captured by the classical modal stability analysis. The optimum initial disturbance is first calculated for different velocity profiles following a quasi-steady approach where the individual profiles are assumed steady within the wave event. Additionally, the resulting short-term maximum energy growth is determined as a function of the streamwise (α) and spanwise (β) wave number. It is shown that the maximum growth is associated with the disturbance with no streamwise dependence ($\alpha = 0$). The formation of streaks is simulated when the three-dimensional DNS is perturbed with the pre-determined optimum initial disturbance. In order to trigger the transition to turbulence, a secondary instability is required. The characteristics of this secondary perturbation is chosen in accordance with the flat plate boundary layer flow. This approach can successfully simulate the bypass transition. Sample result from a representative Re_δ case are presented in the thesis hereafter.

BIOGRAPHICAL SKETCH

Mahmoud Sadek was born in Giza, Egypt, on September 8th, 1983. He earned both bachelor's and master's degrees in Civil Engineering from Cairo University in 2005 and 2010 respectively. During the period 2005-2010, he also worked as a part-time consultant engineer in tunnelling and deep foundation design. In August 2010, he pursue his PhD in the civil and environmental engineering department at Cornell University.

Mahmoud's research interests include environmental fluid mechanics, high-order numerical methods, hydrodynamic instability theory, computational engineering, high accuracy spectral computational methods for high Reynolds number flows in complex geometries, and high performance parallel scientific computing.

In the memory of my father.

To my mother, my wife and my two daughters.

ACKNOWLEDGEMENTS

This work has multiple contributor to whom I am very grateful. From the academic side, this work would never exist without the help, guidance and friendship of my main advisor Prof. Peter Diamessis. I am also thankful to my co-advisor Prof. Philip Liu for his effort, support and motivation. My thanks extend to my third committee member Prof. Olivier Desjardins for the many constructive discussions, help and guidance. One pivot person to this work is Prof. Luis Parras, from the University of Malaga. I owe it to him to introduce me to the amazing world of non-modal stability analysis. I also want to extend my thanks to Profs. Jim Jenkinks and Todd Cowen for their help, learning and company.

I couldn't survive this experience without the friendship, company and support of my dearest EFMH colleagues. I was fortunate to start and finish my PhD with a wonderful group of colleagues, who enriched my PhD experience on both scientific and human level. Thank you Patricio Winckler, Jose Gonzalez, Blair Johnson, Qi Zhou and Nimish Pujara. I also want to extend my thanks to Sumedh Joshi, Ignacio Sepulveda, Gustavo Rivera, Jorge Escobar, Ammar Abdel Ghani, Chao Ann, Erika Johnson, Che-wei Chang, Allie King, Anil Asku, Yong Sung Park, Rafael Tinoco, Seth Schweitzer and Peter Lo. I was also fortunate to develop a friendship with Fahad Mohammed and Atle Jensen and their families. Finally, I want to thank all CEE staff, Nadine Porter, Jeannette Little, Jeff Daves, Cameron Wilkens, Paul Charles, Timothy Brock, Carl Cornell, Sutapa Chosh, Tania Sharpsteen who were very kind and helpful to me through those five years.

I also want to thank all my former professors in Cairo university as well as here in Cornell who contributed much in founding my scientific and engineer-

ing knowledge.

From the personal side, I am very grateful to my father and mother who provided me with the unconditional love and gave me everything without limit. I couldn't go through this experience without the support, care and understanding of my beloved wife and my two gorgeous daughters. I am always grateful to my two sisters, their husbands and kids for everything. Finally my thanks extend to my wonderful family in Egypt who suffered a lot with me through those five years out of their compassion and love. I also want to thank all our friend here in Ithaca for making our stay here an enjoyable experience.

TABLE OF CONTENTS

Biographical Sketch	iii
Dedication	iv
Acknowledgements	v
Table of Contents	vii
List of Figures	ix
1 Introduction	1
1.1 Motivation of the study	1
1.2 Literature review	1
1.2.1 General overview	2
1.2.2 Classical transition studies	6
1.2.3 Bypass transition studies	10
1.3 Objective and scope of the study	13
1.4 Structure of the dissertation	14
2 Problem Formulation and Governing Equations	15
2.1 Governing equations in the inviscid region	15
2.2 Governing Equations in the boundary layer	17
2.3 Linear stability analysis formulation	20
2.3.1 Governing equation of small disturbance	21
2.3.2 Modal analysis	23
2.3.3 Non-modal analysis	24
3 Numerical Methodology	31
3.1 Linear stability analysis	31
3.1.1 Quasi-steady analysis: Eigenvalue problem	31
3.1.2 Transient analysis: Initial value problem	32
3.2 Fully non-linear Simulation	33
3.2.1 Navier-Stokes splitting scheme	34
3.2.2 Spectral multidomain penalty methods	35
3.2.3 Spectral filtering, adaptive interfacial averaging	39
4 Sample Results	43
4.1 Classical Transition Analysis	43
4.1.1 Applicability of the quasi-steady linear stability analysis	43
4.1.2 Two-dimensional Direct Numerical Simulations	49
4.1.3 Three-dimensional Direct Numerical Simulations	58
4.2 Bypass Transition Analysis	60
4.2.1 Quasi-steady transient stability analysis	62
4.2.2 Three-dimensional Direct Numerical Simulation of streak formation	68

5 Discussion	77
5.1 Classical Transition	77
5.1.1 Mode of instability	77
5.1.2 Similarity with instability properties of other wave-driven transient flows	84
5.1.3 Breakdown of the two-dimensional coherent structure . .	86
5.2 Bypass Transition	88
5.2.1 Maximum amplification modes	88
6 Conclusion And Future work	91
6.1 Classical transition	91
6.2 Bypass transition	96
6.3 Future work	98
A Analytical solution for viscous boundary layer flows under weakly nonlinear transient wave	100
B Perturbation Kinetic Energy and Norms	101
Bibliography	103

LIST OF FIGURES

<p>2.1 Schematic (not to scale) of solitary wave of height H^* propagating in a constant water depth h^* with a wavelength l_0^*. $U_o^*(x^*, t^*)$ represents the free stream velocity. BBL is an estimate of the bottom boundary layer.</p> <p>2.2 Sketches of temporal variation of the normalized pressure gradient (dashed line) and free stream velocity (solid line) under a solitary wave at a fixed spatial location.</p> <p>2.3 Schematic of the energy growth variation for a general disturbance. The colour differentiate between the sets governing the behaviour at different time limit. The early initial trend, $t \rightarrow 0^+$, governed by the numerical abscissa (blue). The asymptotic trend, $t \rightarrow \infty$, governed by the least stable eigenvalue (magenta). In between, $0 < t < \infty$, the maximum transient energy growth, results of a resolvent norm size, is highlighted in red.</p> <p>3.1 Exponential filter functions $\sigma(k/N)$ for different filter orders p representative values. The mode number and total number of available modes (over the full domain in Fourier space and over a single subdomain in Legendre space) are denoted by k and N, respectively. The dashed vertical line indicates the normalized wavenumber beyond which the artificial dissipation of a second-order finite-difference scheme has a direct effect, as shown by Domaradzki et al. (2002)</p> <p>4.1 Growth contour of $\omega_i > 0$ for $Re_\delta = 211$ throughout the wave deceleration (thick solid line $\omega_i = 0$, contour value spacing $\Delta\omega_i = 0.001$ and $\omega_{i_{max}} = 1.28 \times 10^{-2}$). Horizontal dashed lines bound the modes with highest growth rates, i.e., $\alpha \in [0.43, 0.47]$. The table below the figure summarizes the following quantities: critical wave phase, critical wavenumber, maximum growth rate, wave phase of the maximum growth rate and the wavenumber with the maximum growth rate (see also section 2.3.2 for definitions).</p> <p>4.2 Time series for the normalized kinetic energy throughout the deceleration phase for $Re_\delta = 211$ for three wave numbers: $\alpha = 0.43$ (dashed line), 0.45 (solid line) and 0.47 (dotted line).</p> <p>4.3 Times series for the normalized vertical perturbation kinetic energy for $\alpha = 0.45$ throughout the deceleration phase for $Re_\delta = 330$ (dotted line), 350 (solid line) and 375 (dash line).</p> <p>4.4 Growth contour of $\omega_i > 0$ for $Re_\delta = 350$ throughout the wave deceleration (thick solid line $\omega_i = 0$, contour value spacing $\Delta\omega_i = 0.001$). Vertical dashed line indicates the start of the flow reversal. Table quantities are as defined in the caption of Fig. 4.1.</p>	<p>16</p> <p>18</p> <p>29</p> <p>41</p> <p>46</p> <p>47</p> <p>48</p> <p>48</p>
---	---

4.5	Growth contour of $\omega_i > 0$ for $Re_\delta = 920$ throughout the wave deceleration (thick solid line $\omega_i = 0$, contour value spacing $\Delta\omega_i = 0.001$). Table quantities are as defined in the caption of Fig. 4.1.	53
4.6	Time series of the normalized bed shear stress for $Re_\delta = 920$ at two different spatial locations. Solid lines represent DNS results whereas dashed lines represent laboratory measurements of SU10.	53
4.7	Time series of the normalized bed shear stress for $Re_\delta = 450$ for two case: the unperturbed case (i.e., analytical laminar solution, solid line) and perturbed case (dashed line)	55
4.8	Transient growth as characterized by sample curves of amplification factor G_W of the most unstable mode for the two categories of the unconditionally unstable regime. Dashed lines correspond to the growth of the $\lambda_x \approx 15$ mode whereas solid lines represent the $\lambda_x \approx 21$ mode.	58
4.9	Iso-contours of λ_2 for $Re_\delta = 1833$ case at different wave phase (ωt). The horizontal and vertical coordinates in each panel are normalized by the boundary layer thickness δ	61
4.10	Variation of \hat{t}_p for different ωt velocity profiles. Colours refer to the different ωt : -50° , -40° , -20° & 0°	63
4.11	Parameter study of the amplification factor G (normalized by the corresponding maximum value) as a function of the streamwise (α) and spanwise (β) wave number for six different base flow profiles of $Re_\delta = 1478$ case. the dark grey area in the $\alpha - \beta$ plane in Fig.4.11(f) corresponds to an asymptotic exponential growth.	64
4.12	Temporal variation of the amplification function $G(t_p)$ corresponding to the critical $(\alpha; \beta)$ combination, i.e., combination leading to the highest algebraic growth, for six different base flow profiles of $Re_\delta = 1478$ case. Critical $(\alpha; \beta)$ combination and corresponding base profile wave phase ωt are reported in the figure legend.	66
4.13	Comparison between amplification function $G(t_p)$ variation as a result of either algebraic or exponential growth for base profile corresponding to $\omega t = 20^\circ$ of $Re_\delta = 1478$ case. The dashed line, sample of exponential growth, corresponds to $(\alpha; \beta) = (0.3; 0)$. Whereas the solid line, sample of algebraic growth, corresponds to $(\alpha; \beta) = (0; 0.7)$. G -axis in log-scale.	66
4.14	Growth contour of $\omega_i > 0$ for $Re_\delta = 1478$ throughout the wave deceleration (thick solid line $\omega_i = 0$, contour value spacing $\Delta\omega_i = 0.001$). Table quantities are as defined in the caption of Fig. 4.1. Vertical dashed line corresponds to $\omega t = 20^\circ$	67

4.15	Normalized contour plot of the optimum initial disturbance shape in the y-z plane associated with the maximum energy amplification for velocity profile $\omega t = -25^\circ$ for $Re_\delta = 1478$ case. Upper panel (a) shows the wall normal perturbation velocity field \hat{w} , whereas panel (b) shows the wall normal vorticity field $\hat{\eta}$ (see 2.3.3 for definition). The vertical and spanwise coordinates in each panel are normalized by the boundary layer thickness δ	70
4.16	Initial distribution of the secondary instability employed in $Re_\delta = 1478$ case. The left panel shows the distribution of the streamwise velocity component of the secondary perturbation on x-y plane located at $z=0.25$. Whereas the vertical distribution of the same quantity at $(X, Y) = (20; 6)$ is shown in the right panel. Coordinates are normalized by the boundary layer thickness δ and velocity amplitude is normalized by the maximum free stream velocity U_{om} .	72
4.17	Iso-contours of λ_2 of the secondary instability initial distribution employed in $Re_\delta = 1478$ case. Coordinates are normalized by the boundary layer thickness δ .	73
4.18	Iso-contours of λ_2 of the secondary instability initial distribution employed in $Re_\delta = 1478$ case. Coordinates are normalized by the boundary layer thickness δ .	74
4.19	Iso-contours of λ_2 for $Re_\delta = 1478$ case at different wave phase (ωt). The horizontal and vertical coordinates in each panel are normalized by the boundary layer thickness δ .	76
5.1	Variation of the neutral curves ($\omega_i = 0$) as a function of Re_δ . The solid ellipse represents the locus of centers of the maximum ω_i of the different cases. The two vertical dashed lines correspond to the wave crest (left) and the flow reversal phase (right)	79
5.2	Growth contour of $\omega_i > 0$ for $Re_\delta = 4000$ throughout the wave deceleration (thick solid line $\omega_i = 0$, contour value spacing $\Delta\omega_i = 0.001$). Table quantities are as defined in the caption of Fig. 4.1.	80
5.3	Transient growth of G_W for $Re_\delta = 4000$. Dashed lines are for $M1$, i.e., $\lambda_x \approx 15$, whereas solid lines are for $M2$, i.e., $\lambda_x \approx 21$.	80
5.4	Growth contour of $\omega_i > 0$ for $Re_\delta = 6300$ throughout the wave deceleration (thick solid line $\omega_i = 0$, contour value spacing $\Delta\omega_i = 0.001$). The three vertical dash lines mark the different insertion phases. Table quantities are as defined in the caption of Fig. 4.1.	81
5.5	Transient growth of G_W for $Re_\delta = 6300$ for three different noise insertion phase cases: $\omega t_{ins} = 0^\circ$ (a), $\omega t_{ins} = 18^\circ$ (b) and $\omega t_{ins} = 30^\circ$ (c). $M1$ is represented by the dashed line whereas solid lines correspond to $M2$.	82

5.6	Visualization of the perturbation vorticity field (normalized by the corresponding maximum value) for $Re_\delta = 4000$ (Figs. 5.6(a) – (c)) and $Re_\delta = 8000$ (Figs. 5.6(d) – (f)) at different wave phase ωt . First row: linear stability analysis. Second and third rows: DNS results. In the DNS results, only a portion of the computational domain is shown. In the left column $M1$ is the dominant instability mode. In the right column $M2$ dominates. The horizontal and vertical coordinates in each panel are normalized by the boundary layer thickness δ	83
5.7	Non-dimensional average growth rate variation as a function of Re_δ . Stable, ●; Unstable, ■. Horizontal dash line represents the applicability limit of the quasi-steady linear stability analysis. . .	85
5.8	Iso-contours of λ_2 with hairpin vortex-like structures for $Re_\delta = 1833$ case at wave phase $\omega t = 75.5^\circ$. The horizontal and vertical coordinates in each panel are normalized by the boundary layer thickness δ	87
5.9	Temporal variation of the amplification function $G(t_p)$ of four different modes with no streamwise dependence $\alpha = 0$ and the different β are shown in the figure legend. The base flow profile corresponds to the wave phase $\omega t = -10^\circ$ of $Re_\delta = 1478$ case. The solid red line corresponds to the critical $(\alpha; \beta)$ combination. . . .	89
5.10	Max. growth amplification as a function of Re_δ . Different colours refer to different base flow ωt : -40°; -30°; -20°; -10° & 0°. Symbols corresponds to modes with $\alpha = 0$ & different β : 0.7 (□); 0.8 (▷); 0.9 (○) & 1.0(×). Fitting dashed lines comply with $G \propto Re_\delta^2$ relation.	90
6.1	Instability map of the BBL flow under solitary waves. The flow is classified in accordance to four criteria: quasi-steady steady linear stability analysis (upper bar), transient linear stability analysis (second bar from top), appearance of the vortex tubes (third from top) and dominant mode of instability (bottom bar).	93

CHAPTER 1

INTRODUCTION

1.1 Motivation of the study

Tsunami waves, which can be characterized as transient long waves, have a massively destructive impact on inundated coastal areas (e.g., 2004 Indian Ocean tsunami and 2011 Japan Tohoku tsunami). Two of the phenomena related to such events are the associated sediment deposition and sea bed erosion (e.g. Liu *et al.*, 2005; Yeh *et al.*, 2007) . Both of these phenomena bear crucial implications for the design of the off- and near- shore structures and for shoreline protection. These sediment-specific processes are mainly driven by the near-bed flow characteristics, i.e., turbulence and bottom stresses. To this end, an in-depth understanding of the near-bottom hydrodynamics and turbulence transition in the bottom boundary layer (BBL) under such waves is imperative, with the study of BBL instability being a prerequisite.

Therefore, in section 1.2, a detailed up-to-date review of the studies addressing the dynamics of the BBL under solitary wave is presented. Additionally, there will be a review of the studies addressing the stability properties of the BBL under solitary wave, in specific, as well as under other flow configurations.

1.2 Literature review

This section is divided into three parts: general overview, classical transition and bypass transition. The general overview summarizes the approach fol-

lowed, chronologically, to study the long waves as well as its induced boundary layer in the literature. Additionally, this summary includes the general assumptions and limitations that will be reflected on our study. The remaining two parts introduce the most relevant stability studies for the BBL under solitary waves and other similar transient base flows. Two main types of transition are considered in those stability studies. The first one, referred to as classical transition, results from the breakdown of the exponentially growing 2-D Tollmien-Schlichting waves. Whereas, in the second type, referred to as bypass transition, the flow undergoes an early transition to turbulence before the formation of those 2D coherent structures. One of the main possible scenario of this early transition, is the formation of localized turbulent spots, subsequent to the breakdown of organized streamwise elongated streaks, that expand spatially to finally alter the base flow state. This scenario is the one considered in this study and will be always referred to as the bypass transition. The classical transition of the flow is governed by the long-term, asymptotic behaviour of the disturbance, whereas the bypass transition is related to the short term behaviour as well be shown later in the text.

1.2.1 General overview

The solitary wave has been generally adopted as a canonical model of transient long waves in both experimental and theoretical studies since the 1970's. Although this idealization is not exactly representative of actual tsunami waves (Madsen *et al.*, 2008), Chan & Liu (2012) showed that the leading tsunami wave can be adequately modeled by a linear superposition of a number of sech^2 -wave forms. In this study, as an additional simplification, we will restrict our analysis

to the simple case where a single solitary wave is used to approximate small amplitude long waves typical of the coastal ocean.

Liu & Orfilla (2004) used a perturbation approach and the Boussinesq approximation to derive an analytical solution for the laminar viscous boundary layer flows under transient waves. Their analytical solution was based on the linearized boundary layer equations and can be found in Appendix (A). Subsequently, Liu, Park & Cowen (2007) extended this work to take into account the nonlinearity in the boundary layer equations and compared both analytical solutions, linear and nonlinear, with experimental data. They used particle image velocimetry (PIV) to measure the boundary layer velocity field under a solitary wave in a wave tank. They found good agreement between the theoretical solution and the experimental data. Another significant finding was that the boundary layer flow reverses its direction, and so does the bed shear stress, in the deceleration phase of the free stream velocity which always moves in the same direction of the wave propagation. The flow reversal is a result of the adverse pressure gradient which is established in the deceleration phase after the passing of wave crest. This pressure gradient gives rise to an inflection point in the velocity profile, which is a necessary but not sufficient condition for inviscid instability (Criminal *et al.*, 2003). In Liu *et al.* (2007) experiments, the free-stream Reynolds number, Re , of the experiments examined was $O(10^4)$ and the boundary layer flow was always laminar. Specifically, the free-stream Reynolds number is defined as

$$Re = \frac{a^* U_{om}^*}{v^*} \quad (1.1)$$

where U_{om}^* is the maximum wave-induced free-stream velocity, v^* is the fluid

viscosity and a^* is the half of the wave-induced water particle displacement in the free-stream region, which is the ratio of maximum free-stream velocity, U_{om}^* , to the wave angular frequency, ω^* (to be defined later).

Sumer *et al.* (2010), hereafter SU10, pursued the experimental investigation of the boundary layer evolution under solitary waves with higher Reynolds number. To overcome laboratory limitations in attainable Re , they mimicked the BBL flow under a solitary wave using a U-shaped water tunnel in which the flow was driven by a time-varying, spatially independent, pressure gradient induced by a soliton-like wave in the flow direction. In this regard, it is emphasized that no actual surface solitary wave is present in the particular experimental study. Using the one-dimensional transient flow to simulate the inviscid free stream velocity under long waves is a reasonable approximation because, for very long waves, the spatial variation of the pressure gradient is small and can be neglected. Using this approach, SU10 were able to increase their Reynolds number to a maximum value of $Re = 2 \times 10^6$ which is two orders of magnitude higher than the previously discussed studies. SU10 showed that the boundary layer flow characteristics changed with increasing Reynolds number from laminar ($Re < 2 \times 10^5$) to laminar with two-dimensional vortex tubes near the bed ($2 \times 10^5 \leq Re < 5 \times 10^5$), and finally, to a transitional regime characterized by the appearance of single/multiple turbulent spots ($Re > 5 \times 10^5$). However, due to the limitation of the experimental facility, SU10 were not able to reach a Reynolds number that is high enough for the BBL to become fully turbulent. SU10 demonstrated that their data agree well with the analytical solution of Liu & Orfilla (2004) and the previous wave tank measurements of Liu *et al.* (2007) for the laminar Re range ($Re < 2 \times 10^5$). In the transitional regime, $Re > 5 \times 10^5$, SU10 reported the appearance of turbulent spots, which appeared

as single or multiple spikes in the bed shear stress measurements concurrently with the vortex tubes. SU10 speculated that at higher Re , i.e., $Re > 2 \times 10^6$, the transition to turbulence can take place in the wave acceleration phase, although they could not explicitly reproduce it due to facility limitations. The mechanism behind the generation of the vortex tubes was interpreted by SU10 as the result of the inflectional-point shear layer instability similar to the observations of Carstensen *et al.* (2010) in oscillatory boundary-layer flows. It is worth noting that in their experiments, SU10 did not introduce explicitly any perturbation into their system but rather relied on the naturally available ambient disturbances in the laboratory environment.

Additionally, Carstensen *et al.* (2010) observed also the formation of locally, in time and space, distributed turbulent spots in their oscillatory base flow for $Re > 1.5 \times 10^5$. In order to rule out the dependence on the wall roughness conditions, they were able to reproduce the turbulent spots for the same base flow over rough bed but rather at a lower critical Reynolds number, $Re > 4.4 \times 10^4$ (Carstensen *et al.*, 2012). Mazzuoli *et al.* (2011) used DNS to replicate Carstensen *et al.* (2010) experiment and specifically the formation of the turbulent patches. They numerically induced the formation of those spots using "microscopic", $O(10^{-4})$, sinusoidally-shaped wall imperfections with a wavelength dependence in both span- and streamwise directions. However, no justification was given for their choice of these wavelength. In the following two subsections (i.e., 1.2.2 & 1.2.3) a general summary of both types of transition studies, for the base flow of interest or similar flow types, will be given.

1.2.2 Classical transition studies

Driven by the outcomes of Liu & Orfilla (2004) and Liu *et al.* (2007), Vittori & Blondeaux (2008) performed a three-dimensional direct numerical simulation (DNS) to simulate the boundary layer under a solitary wave. They discussed the dependence of the nature of the transition to turbulence on the ratio of wave amplitude to water depth. Following the SU10 study and motivated by their findings, Vittori & Blondeaux (2011) employed the same numerical tool, used in their previous (2008) study, to investigate the development of coherent structures in the boundary layer and the efficacy of the log-law of the wall in approximating the structure of the near-bed flow field for a range of wave amplitudes. They reported a qualitative agreement between their numerical results and the experimental observations of SU10. They suggested that the generated vortices result from the growth of Tollmien-Schlichting waves. In each of the two studies by Vittori & Blondeaux (2008 & 2011), the base flow was perturbed by inserting weak random noise, of a relative order of amplitude $O(10^{-4})$ with respect to U_{om}^* , into the initially quiescent velocity field. Both studies were unable to simulate the formation of the turbulent spots that appeared in the BBL of the SU10 experiment. The lower bound for the emergence of the coherent structures was estimated to be somewhere below $Re \lesssim 5 \times 10^5$. Moreover, the transition to turbulence was suggested to take place immediately above this cut-off, i.e., $Re > 5 \times 10^5$. They claimed that the discrepancy with the laboratory was due to the different sources of instability, i.e., bed roughness and vibrations, in the laboratory experiment in SU10. Furthermore, they indicated that the transition to turbulence and the formation of the coherent structures always took place in the wave deceleration phase. Later on, Scandura (2013) studied numerically the characteristics of the two-dimensional vortex tubes generated un-

der solitary waves within a range of Re equivalent to SU10 experimental range. Scandura used small-amplitude sinusoidally-shaped imperfections in the bottom boundary with a wavelength equivalent to the wavelength of the most unstable mode predicted from the linear stability analysis, as a source of disturbances. He showed that the mean spacing between the numerically developed vortex tubes is close to the one observed by SU10 for the range of Re and it was approximately constant for the range of the tested Re . The effect of the bottom wall perturbation is outside the scope of the investigation performed hereafter.

Ozdemir *et al.* (2003) carried out a number of three-dimensional direct numerical simulations to simulate the transition to turbulence in the BBL under a solitary wave for Re one order of magnitude higher than SU10. They inserted a two-dimensional random perturbation noise at the initial quiescent flow field with amplitudes varying between 1 to 20% of the maximum free stream velocity. Ozdemir *et al.* observed two possible instability mechanisms within a wave event: a short-lived non-linear long-wave instability that takes place during the acceleration phase for a large disturbance amplitude and a broadband linear instability which always takes place after the flow reversal during the wave deceleration phase. Moreover, they discussed the path of transition to nonlinear chaotic motions, i.e., turbulence, as a function of Re . They used a high order numerical model. Nevertheless, the transition to turbulence was always found to follow the breakdown of the spanwise rollers, i.e., vortex tubes, that results from the growth of the Tollmien-schlichting waves (T-S) in the deceleration phase. They divided the BBL flow under a solitary wave into four regimes: laminar, disturbed laminar, transitional and turbulent.

The observations of SU10 and previously discussed numerical studies indi-

cate that an aspect of the wave-induced BBL which merits further investigation are its instability properties, namely in the context of BBL response to externally imposed perturbations. The fundamental feature of these instability properties is the growth of 2D T-S waves which can be quantified, asymptotically, by solving the classical Orr-Sommerfeld (OS) equations for a single base flow profile. From the OS equations, the degree of perturbation amplification can be determined, either temporally or spatially, for steady parallel/nearly-parallel base flow velocity profile. A classical example of the application of such a temporal stability analysis to a BBL flow is the case of the zero-pressure-gradient flat plate boundary layer (e.g. Drazin *et al.*, 2004). Following SU10's assumptions, the BBL flow under solitary waves can be approximated, as previously indicated, as a sequence of temporally varying velocity profiles that are uniform in space,i.e., x-independent. This spatial uniformity satisfies the condition of the parallel base flow which allows the application of a temporal growth analysis focused on the OS equations instead of some other approach such as parabolic stability analysis (e.g., Herbert, 1997). Nevertheless, as further elaborated in the next section, the unsteadiness of the BBL base flow must to be accounted for in the stability analysis. To this end, two approaches are commonly used: Floquet theory and the quasi-steady approximation. The former is only appropriate for periodic base flows as previously done for a large number of relevant studies (e.g. Kerczek 1982 ; blennerhassett & Bassoum, 2002; Poulin *et al.*, 2003 and Luo & Wu, 2010). The latter, first introduced by Shen (1961) , relies on the assumption that the perturbation growth rate be faster than the rate of change of the base flow (e.g. Seminara & Hall, 1975 and Hall & Parker, 1976).

Blondeaux *et al.* (2012) were the first to carry out a quasi-steady linear stability analysis of the BBL flow at the bottom of a solitary wave using a "moment-

tary" criterion of instability founded on the previously mentioned assumption of a perturbation development time scale that is much smaller than the time scale of the wave. Their analysis indicates that the laminar flow is linearly unstable for a range of flow parameters smaller than those observed in the SU10 (i.e., in the laminar regime, $Re < 2 \times 10^5$). They suggested using the growth of the dimensionless kinetic energy per unit area of the flow perturbations as a measure for the flow transition from one regime to another (i.e., appearance of coherent structures). In their study, Blondeaux *et al.* (2012) reported fair agreement with the SU10 experiment in terms of the most unstable mode. However, the wave phase value at which the coherent structure appears in the experiment is much larger than the critical wave phase predicted by their linear stability analysis. We remark here that this difference could be caused by the fact that the perturbation amplitude needs some time to grow and reach a significant level in order to be observed, which contradicts the fundamental assumption of large separation between the time scale of the wave and that of the perturbation growth. In all these studies, instability is always observed in the deceleration phase for the range of wave parameters examined.

Recently, Verschaeve *et al.* (2014) performed spatial stability analysis of the boundary layer under surface solitary waves by solving the parabolic stability equation. This technique allowed them to take into account the non-parallel effect of the base flow when including the non-linear term in the boundary layer equations. They also compare those results to the quasi-steady profile analysis, i.e., the Orr-Sommerfeld equation. Their preliminary results suggest that the approximation made by all previously referenced studies, i.e., neglecting the non-linear effect and studying the problem from the temporal point of view, is valid for the range of Re where the instability is significant. Investigating this

problem in the spatial framework can be challenging in terms of ensuring the adequate resolution of the different modes of instability over a long domain.

1.2.3 Bypass transition studies

The term bypass is commonly used to refer to all other routes of transition to turbulence other than the classical one, i.e., breakdown of the 2D coherent structures due to a secondary instability (Morkovin, 1969). More recently, the term started to become mostly associated with a specific breakdown scenario where the transition is induced by free stream disturbances or for transition, observed in experiments, of asymptotically stable base flow such as for Plane Poisseuille flow or classical flat plate boundary layer as determined by the classical modal stability analysis (e.g. Schmid and Henningson, 2001).

The bypass transition can be divided into two stages. The first stage consists of the formation of elongated streaks of alternating high- and low- speed. The streaks amplitude grow to reach a sufficiently high value at which non- linear effects become important. At the end of this stage, a secondary instability of particular streaks develops which causes a localize breakdown into turbulent spots. The formation of turbulent spots and their growth leading to a fully turbulent boundary layer has been a subject of interest of multiple studies since the work of Emmons (1951) (e.g. Riley & Gad-el-Hak, 1985; Zaki, 2013)

In regards to zero-pressure gradient boundary layer studies, the literature is extensive. The size of the elongated streaks, also known as Klebanoff modes (Klebanoff, 1971; Kendall, 1991), is of the order of the boundary layer thickness. The explanation of the amplification of these streaks, was given by two

rather different approaches : rapid distortion theory (Phillips, 1969) or the linearly non-modal growth of the optimized initial disturbance (Butler & Farrell, 1992; Andersson *et al.*, 1999). From a physical point of view, the ability of the streamwise elongated vortices to mix high- and low-momentum fluid, creating the high and low streamwise velocity streaks, is attributed to the well-known lift-up effect (Landahl, 1980).

The connection between Klebanoff modes and breakdown to turbulence is not straightforward and its exploration has relied on DNS results (e.g. Jacobs & Durbin, 2001; Schlatter *et al.*, 2008) and experiments (e.g. Nolan & Walsh, 2012). Different attempts were made in order to explain this transition mechanism from different perspectives. Zaki & Durbin (2005) studied this mechanism from the point of view of the interaction of two, low- and high-frequency, free-stream vortical modes interaction. Using the same methodology, the effect of pressure gradients (Zaki & Durbin, 2006) and interaction between streaks and discrete instability waves (Liu *et al.*, 2008) were assessed.

As regards the onset of secondary instability¹, Hœpffner *et al.* (2005) performed a linear stability analysis, using the non-modal approach, to study the transient growth of perturbations imposed on the boundary layer streaks where the amplitude of these streaks is below the threshold at which the streaks are linearly unstable. They gauged the energy amplification that results from applying a time-dependent disturbance to the streaky base flow with either spanwise symmetric (varicose) or antisymmetric (sinuous) structure. From those two patterns, the sinuous mode produce higher transient energy growth. Alternatively, Vaughan & Zaki (2011) used DNS to assess the stability of boundary

¹Unless otherwise stated, the secondary instability will always refer to the perturbation causing the breakdown of the streaks and leading to the bypass transition.

layer streaks. They reported that the stability of the streaks is a result of the competition of two modes which they named inner and outer instability modes, in accordance to the wall normal location of their respective critical layers.

In regards to investigation of bypass transition for unsteady base flow, most of the studies, either experimental or theoretical, have focused on flows in pipes or channels: either oscillatory (e.g. Wygnanski & Champagne, 1973 ; Thomas *et al.*, 2011) or pulsatile (e.g. Stettler & Hussain, 1986 ; Fedele *et al.*, 2005 ; Zhao *et al.*, 2007).

On the other hand, the identification of turbulent spots and their lateral boundaries in the laminar flow has never been a straightforward matter (e.g. Schubauer & Klebanoff, 1956 ; Gad-el-hak *et al.*, 1981). Rehill *et al.* (2013) compared between six different detection criteria of the turbulent spot from DNS data for two different base flows. Within the six methos, the Q criterion² quantity based on the velocity gradient tensor, shows the least sensitivity for the zero free-stream case and the instantaneous turbulent dissipation criterion for the streaky boundary layer case. However, for both flow cases, the λ_2 criterion³ shows robustness in the identification of the full evolution process of the turbulent spot. The instantaneous wall-normal velocity criterion was classified as the most sensitive to threshold level for both flows.

² $Q = \frac{1}{2}(\|\Omega\|^2 - \|S\|^2)$. where S & Ω are the symmetric and the antisymmetric parts of the velocity gradient tensor.

³ λ_2 is the second largest eigenvalue of $S^2 + \Omega^2$. it is used to allocate vortex cores as the pressure is minimal in a 2D plane perpendicular to the vortex core (Jeong & Hussein, 1995).

1.3 Objective and scope of the study

The main objective of this study is to establish a deep and better understanding of the different scenarios for transition to turbulence in the BBL under solitary waves. For the sake of comparison with the laboratory observations of SU10, the base flow in this study will be approximated according to the corresponding U-tube experiment: the transient base flow is driven by an uniform soliton-like wave induced pressure gradient.

The first part of this study, will focus on the classical route of transition. For this type of transition, emphasis is placed on two-dimensional instability according to Squires theorem (Drazin, 2004). The outcome of this first effort consists of producing a detailed map of the 2D instability in the flow's parameter space for the BBL flow driven by a solitary wave. The first step towards establishing such a map is to assess the limits of applicability of the quasi-steady linear stability analysis proposed by Blondeaux *et al.* (2012), taking into account the time-dependent base flow. The next step consists of studying the variation in the resulting instability response as a function of the inserted noise characteristics (i.e., initial amplitude, insertion phase, etc.) for increasing Re using a fully non-linear two-dimensional pseudo-spectral code, which neither introduces nor amplifies any numerical noise. Additionally, the difference between the predicted instability in the theoretical/numerical studies and the one observed in the SU10 experiment is discussed in detail. Only two-dimensional analysis is performed. This allows one to reach a maximum Re higher than previous studies and to complete the stability map for the onset of two-dimensional instability.

In the second part of this study, the bypass transition is investigated. Ultimately, in order to study this type of transition, the three-dimensional nature of the flow has to be considered. This investigation consists of performing a three-dimensional linear stability analysis in order to identify the optimum initial noise distribution that induces the maximum transient growth for the unsteady base flow of interest. Fundamentally, this analysis will elucidate the formation of the low- and high- amplitude streaks observed by SU10. Accordingly, a fully non-linear three-dimensional pseudo-spectral code will be used to verify the results for the temporally evolving base flow. Additionally, using the 3D DNS code along with the appropriate secondary instability, the subsequent stage, i.e., evolution of the turbulent spot, can be replicated. Due to computational resource limitation, this study will focus on a specific Re value guided by the observation of SU10 .

1.4 Structure of the dissertation

The rest of this thesis is structured as follows. Chapter 2 presents the problem formulation and governing equations. In chapter 3 a brief description of different numerical approaches used in the discretization of the governing equations is given. In chapter 4, sample results are presented and then followed by a discussion in chapter 5. The conclusion is given in the last chapter 6. All of the chapters, will be divided into two main sections: one dealing with the 2D analysis and the corresponding classical transition while the other section will be devoted for the 3D analysis and the bypass transition.

CHAPTER 2

PROBLEM FORMULATION AND GOVERNING EQUATIONS

2.1 Governing equations in the inviscid region

Consider a two-dimensional solitary wave, that is uniform in the out of plane third dimension, of height H^* that propagates in a constant water depth h^* with a wavelength l_0^* . Hereafter, the (*) sign indicates dimensional quantity. The Cartesian coordinate system (x^*, z^*, y^*) is employed, where x^* points in the wave propagation direction, z^* is the vertical coordinate pointing upward with its origin at the bed and y^* is the horizontal spanwise direction perpendicular to the wave propagation direction. Under such a wave, the irrotational velocity field, i.e., $U_o^*(x^*, t^*)$, outside the boundary layer can be determined from potential flow theory (e.g. Grimshaw, 1971). A simple schematic for such a wave is illustrated in Fig.2.1

As indicated earlier in (1.3), this study will replicate the flow used in the U-tube experiment of SU10 as an approximation to the irrotational velocity component under a surface solitary wave. In this experiment, the generated free-stream velocity corresponds to the leading order solutions of Grimshaw's formulae under the assumption of a small amplitude wave, i.e., $(H^*/h^* \rightarrow 0)$, and neglecting the relatively small spatial variation at any location under a long wave. Accordingly, the unidirectional horizontal velocity field outside the boundary layer can be expressed as follows

$$U_0^*(t^*) = U_{0m}^* \operatorname{sech}^2(\omega^* t^*) \quad (2.1)$$

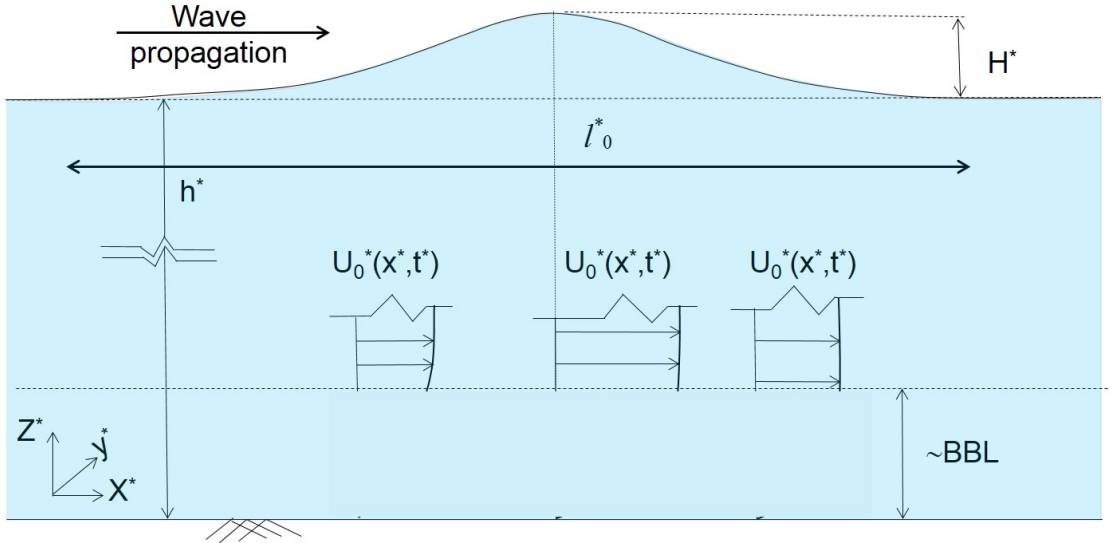


Figure 2.1: Schematic (not to scale) of solitary wave of height H^* propagating in a constant water depth h^* with a wavelength l_0^* . $U_o^*(x^*, t^*)$ represents the free stream velocity. BBL is an estimate of the bottom boundary layer.

where U_{om}^* is the wave amplitude defined as

$$U_{0m}^* = \sqrt{g^* h^*} \frac{H^*}{h^*}. \quad (2.2)$$

and g^* is the gravitational acceleration. The wave frequency ω^* is defined as

$$\omega^* = \sqrt{\frac{3g^* H^*}{4h^{*2}}} \quad (2.3)$$

and, hence, a wave period (T^*) can be defined as

$$T^* = \frac{2\pi}{\omega^*} \quad (2.4)$$

which can be considered as the characteristic time scale of the solitary wave event.

Hereafter, we will omit the (*) from the product $(\omega^* t^*)$ since this product is dimensionless. Strictly speaking, a solitary wave starts at $\omega t = -\infty$ and ends

at $\omega t = +\infty$. In the following discussion, we shall truncate the entire event to $-180^\circ \leq \omega t \leq 180^\circ$. The free stream starts from rest at $\omega t = -180^\circ$ and keeps accelerating until the maximum free stream velocity U_{om}^* is reached, at the crest, i.e., $\omega t = 0$. This acceleration stage is followed by a deceleration phase where the free stream velocity is reduced back to effectively zero due to an adverse pressure gradient.

Outside the BBL, the streamwise pressure gradient from the x-momentum equation is simply

$$\frac{1}{\rho^*} \frac{\partial p_0^*}{\partial x^*} = - \frac{\partial U_0(t^*)}{\partial t^*} = 2 U_{om}^* \omega^* \operatorname{sech}^2(\omega t) \tanh(\omega t) \quad (2.5)$$

where ρ^* is the fluid density. Fig. 2.2 shows a sketch of the free stream velocity normalized by the maximum free stream velocity (U_{om}^*) and the corresponding pressure gradient, normalized by the absolute maximum pressure gradient, under a solitary wave.

2.2 Governing Equations in the boundary layer

The Navier-Stokes (NS) equations describing the motion of a three-dimensional, incompressible flow in the BBL in vector notation are

$$\frac{\partial \vec{u}^*}{\partial t} = -(\vec{u}^* \cdot \nabla) \vec{u}^* - \frac{1}{\rho^*} \nabla p^* + \nu^* \nabla^2 \vec{u}^*, \quad (2.6)$$

$$\nabla \cdot \vec{u}^* = 0, \quad (2.7)$$

where \vec{u}^* represents the velocity vector and ν^* is the kinematic viscosity. In a three-dimensional domain (x^*, z^*, y^*) , the velocity vector has three components

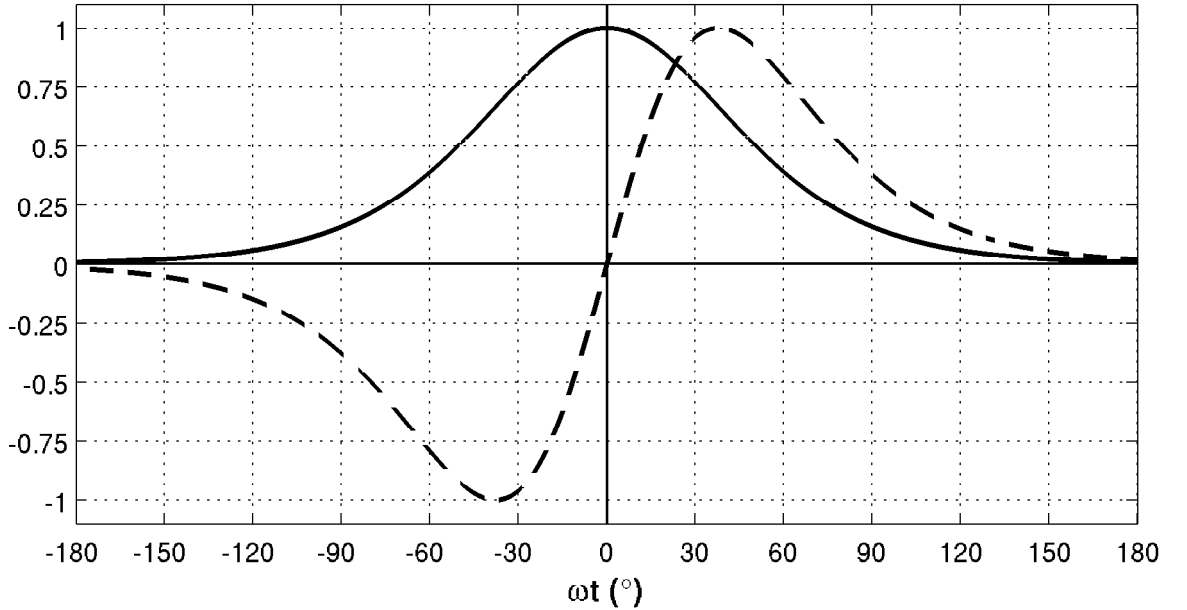


Figure 2.2: Sketches of temporal variation of the normalized pressure gradient (dashed line) and free stream velocity (solid line) under a solitary wave at a fixed spatial location.

(u^*, w^*, v^*) . u^* is the horizontal streamwise component in the x^* -direction; i.e., wave propagation direction; w^* represents the vertical component of the velocity vector in w^* -direction and (v^*) is the second horizontal velocity component but in the spanwise y^* -direction. In the two-dimensional problem, the domain coordinates reduce to (x^*, z^*) with a corresponding velocity vector of two components (u^*, w^*) . For the 3D problem, the gradient vector is $\nabla = (\frac{\partial}{\partial x^*}, \frac{\partial}{\partial z^*}, \frac{\partial}{\partial y^*})$ and reduces to $\nabla = (\frac{\partial}{\partial x^*}, \frac{\partial}{\partial z^*})$ in the 2D case.

Consequently, the total pressure (p^*) in Eqs. (2.6) can be divided into two parts

$$p^* = p_0^*(x^*, t^*) + p''^*(x^*, z^*, y^*, t^*) \quad (2.8)$$

where p''^* is the dynamic pressure that develops in response to the BBL flow and later to the velocity perturbation. As in the U-tube experiment, carried out by SU10, the flow is driven by a pressure gradient $\partial p_0^*/\partial x^*$ given in Eqs. (2.5) that is constant in space yet variable in time.

To nondimensionlize the problem, we use U_{om}^* as a velocity scale and the Stokes laminar boundary layer thickness δ^* ,

$$\delta^* = \left(\frac{2\nu^*}{\omega^*} \right)^{\frac{1}{2}}, \quad (2.9)$$

as a length scale .

Using the above length and velocity scales, the non-dimensional NS equations in the BBL in Cartesian coordinates are written as

$$\nabla \cdot \vec{u} = 0, \quad (2.10)$$

$$\frac{\partial \vec{u}}{\partial t} + (\vec{u} \cdot \nabla) \vec{u} = -\nabla p + \frac{1}{Re_\delta} \nabla^2 \vec{u}, \quad (2.11)$$

where the non-dimensional quantities are non-starred and the BBL Reynolds number based on the boundary layer thickness is

$$Re_\delta = \frac{\delta^* U_{om}^*}{\nu}. \quad (2.12)$$

We can express the relation between the BBL Reynolds number Re_δ and the free stream velocity based Reynolds number Re , defined in Eq. (1.1), as

$$Re_\delta = \sqrt{2Re}. \quad (2.13)$$

From Eqs. (2.2), (2.9) and (2.12), Re_δ can be expressed as

$$Re_\delta = \sqrt{\frac{16}{3} \frac{H^*}{h^*} \frac{h^*}{\delta^*}}. \quad (2.14)$$

From the equation above, in contrast to previous study of Blondeaux *et al.* (2012), it is clear that the parameter space of the problem in hand, following the assumptions in (2.1), collapses into a single parameter which is the Reynolds number Re_δ .

2.3 Linear stability analysis formulation

Linear stability analysis can be employed to study the stability of a BBL flow under the assumption that the base flow is parallel or nearly parallel. Accordingly, this section will be divided into two main parts.

The first part, focusing on modal analysis, is associated with the long-term asymptotic exponential growth and it involves a traditional quasi-steady linear stability analysis. This analysis is mainly performed in the two-dimensional framework and it is similar to the one carried out by Blondeaux *et al.* (2012) where a “momentary” criterion for instability and a “frozen” base flow are assumed and an eigenvalue problem is solved. Hence, in order to take into account the transient nature of the base flow, especially for the relatively low Re_δ regime, an initial value problem is solved in place of the eigenvalue problem.

The second part, focusing on non-modal analysis, considers the short term maximum transient growth of the disturbance associated with the formation of the streaks. For this analysis, one is inevitably required to consider the three-dimensional aspect of the base flow. The outcome of this analysis con-

sist of identifying the optimal initial disturbance that will potentially undergo the maximum transient growth and, hence, enable a bypass transition as manifested in the form of turbulent spots.

2.3.1 Governing equation of small disturbance

For the sake of completeness, a brief review of the derivation of perturbation evolution equations are presented hereinafter for a steady velocity profile (see Schmid & Henningson 2001) for further details). The flow field is decomposed into a laminar steady base flow and a fluctuating component as follows

$$p = P(x) + \tilde{p}(x, z, y, t), \quad (2.15)$$

$$\vec{u} = (U(z), 0) + (\tilde{u}, \tilde{w}, \tilde{v}). \quad (2.16)$$

In the above Eqs (2.15 & 2.16), the time dependence of the base flow is neglected and $P(x)$ & $U(z)$ represent the quasi-steady base flow mean pressure and velocity. The unperturbed horizontal velocity in the boundary layer for a specific ωt , i.e., $U(z)$, is calculated from the analytical solution of Liu & Orfilla (2004). The tilde indicates the fluctuating component and the uppercase letter represent the base flow. Substituting Eqs. (2.15) and (2.16) in Eqs. (2.10) and (2.11), subtracting the leading order balance of the base flow and neglecting the non-linear terms, results in the following linearized equations.

$$\frac{\partial \tilde{u}}{\partial x} + \frac{\partial \tilde{w}}{\partial z} + \frac{\partial \tilde{v}}{\partial y} = 0, \quad (2.17)$$

$$\frac{\partial \tilde{u}}{\partial t} + U \frac{\partial \tilde{u}}{\partial x} + w U' = -\frac{\partial \tilde{p}}{\partial x} + \frac{1}{Re_\delta} \nabla^2 \tilde{u}, \quad (2.18)$$

$$\frac{\partial \tilde{w}}{\partial t} + U \frac{\partial \tilde{w}}{\partial x} = -\frac{\partial \tilde{p}}{\partial z} + \frac{1}{Re_\delta} \nabla^2 \tilde{w}, \quad (2.19)$$

$$\frac{\partial \tilde{v}}{\partial t} + U \frac{\partial \tilde{v}}{\partial x} = -\frac{\partial \tilde{p}}{\partial v} + \frac{1}{Re_\delta} \nabla^2 \tilde{v}. \quad (2.20)$$

The ('') denotes derivative with respect to z . Eliminating the pressure terms in the above equations, the equation for the streamwise vertical velocity (\tilde{w}) is obtained as follows

$$\left[\left(\frac{\partial}{\partial t} + U \frac{\partial}{\partial x} \right) \nabla^2 - U'' \frac{\partial}{\partial x} - \frac{1}{Re_\delta} \nabla^4 \right] \tilde{w} = 0. \quad (2.21)$$

Equation (2.21) is sufficient to describe the two-dimensional flow field. However, in order to fully describe the three-dimensional field, an additional equation, together with (2.21), is needed. Thus, the most convenient equation is the one associated with the normal vorticity, $\tilde{\eta}$, that can be written as follows

$$\left[\frac{\partial}{\partial t} + U \frac{\partial}{\partial x} - \frac{1}{Re_\delta} \nabla^2 \right] \tilde{\eta} = -U' \frac{\partial \tilde{w}}{\partial y}, \quad (2.22)$$

where $\eta = \partial \tilde{u} / \partial y - \partial \tilde{v} / \partial x$.

The boundary conditions $\tilde{w} = \partial \tilde{w} / \partial z = \tilde{\eta} = 0$ both at the bed ($z = 0$) and in the far-field ($z \rightarrow \infty$) are required. In this study, the far field upper boundary of the domain of Eqs. (2.21 & 2.22) is fixed at $z = 15$ (dimensionless), which

is sufficiently far from the bed and at this location the flow can be reasonably assumed to be uniform in the vertical direction.

2.3.2 Modal analysis

In order to determine the most unstable mode, i.e. mode with highest exponential growth rate, a quasi-steady analysis is performed in the modal framework. According to Squire(1933), a two-dimensional disturbance is more unstable than its corresponding three-dimensional one, at a specific Re , for a steady parallel base flow in the asymptotic limit when ($t \rightarrow \infty$). Henceforth, the two-dimensional disturbance will only be considered for the eigenvalue problem. Following the classical modal approach (see Schmid & Henningson, 2001), the perturbation velocity is decomposed into normal modes as follows

$$\tilde{w} = \bar{w}(z) e^{i(\alpha x - \omega_p t)} \quad (2.23)$$

where α is the wavenumber in the x direction ($\alpha = \frac{2\pi}{\lambda_x}$, λ_x is the streamwise wavelength of the perturbation, which eventually determines the spacing between the resulting vortex tubes), \bar{w} is the perturbation wave-like amplitude and ω_p is the perturbation frequency ($\omega_p = \omega_r + i\omega_i$). Substituting Eq. (2.23) in Eq. (2.21) (equivalent to taking the Fourier transform in the horizontal directions), the well-known OS (Orr, 1907; Sommerfeld, 1908) equation is obtained

$$-i\omega_p [k_{2D}^2 - D_z^2] (\bar{w}) + [L_{OS}] (\bar{w}) = 0 \quad (2.24)$$

with the OS operator L_{OS} defined as

$$L_{OS} = iaU(k_{2D}^2 - D_z^2) + iaU'' + \frac{1}{Re_\delta} (k_{2D}^2 - D_z^2)^2. \quad (2.25)$$

In the equation above, D_z is the derivative operator, with respect to z . $k_{2D} = \alpha$ for the two-dimensional case. For the temporal stability analysis, ω_p is complex and it appears as the eigenvalue in the OS equation for each profile. If $\omega_i > 0$, this indicates an unstable mode (i.e., growth in time) whereas $\omega_i < 0$ corresponds to a decaying mode.

Five important quantities are used to characterize the instability properties of a particular Re_δ as estimated from quasi-steady linear stability analysis. The earliest time at which growth contours of ω_i cross the zero threshold towards monotonically increasing positive values is regarded as the critical wave phase, $\omega t_{(critical)}$ which has its corresponding critical wave number $\alpha_{(critical)}$. The maximum growth rate, $\omega_{i_{max}}$, occurs at $\omega t(\omega_{i_{max}})$ and for a corresponding wavenumber $\alpha(\omega_{i_{max}})$.

Recall, from section 1.2.2, that the main assumption of using the quasi-steady analysis for a transient base flow is that the perturbation growth rate is faster than the rate of change of the base flow. As will be shown in section 4.1.1, the applicability of this assumption will be tested for the particular BBL of interest by comparing both quasi-steady and transient 2D analysis.

2.3.3 Non-modal analysis

In order to evaluate the short-term perturbation dynamics, the perturbation evolution equations are to be reformulated in the non-modal frame. This can be simply done by assuming a more general form of the initial perturbation. Contrary to (2.23), solutions for the vertical perturbation velocity and normal

vorticity can be assumed as follows

$$\tilde{w} = \hat{w}(z, t) e^{i(\alpha x + \beta y)}, \quad (2.26)$$

$$\tilde{\eta} = \hat{\eta}(z, t) e^{i(\alpha x + \beta y)}, \quad (2.27)$$

where α , as previously mentioned in (2.3.3), is the streamwise wavenumber, β is the wavenumber in the y direction ($\beta = \frac{2\pi}{\lambda_y}$, λ_y is the spanwise wavelength of the perturbation, which eventually determines the spacing between the streaks), \hat{w} and $\hat{\eta}$ are the wave-like amplitudes. Substituting Eqs. (2.26 & 2.27) in Eqs. (2.21 & 2.22) respectively, following equations are obtained

$$\left[k^2 - D_z^2 \right] \frac{\partial \hat{w}}{\partial t} + [L_{OS}] \hat{w} = 0, \quad (2.28)$$

$$\frac{\partial \hat{\eta}}{\partial t} + [L_{SQ}] (\hat{\eta}) = -i\beta U' (\hat{w}), \quad (2.29)$$

where the OS operator L_{OS} and the squire operator L_{SQ} are now defined as

$$L_{OS} = i\alpha U \left(k^2 - D_z^2 \right) + i\alpha U'' + \frac{1}{Re_\delta} \left(k^2 - D_z^2 \right)^2, \quad (2.30)$$

$$L_{SQ} = i\alpha U + \frac{1}{Re_\delta} \left(k^2 - D_z^2 \right). \quad (2.31)$$

In the above system of equations, D_z is the derivative operator, with respect to z and $k = \sqrt{\alpha^2 + \beta^2}$ is the modulus of the wave number vector. From the incompressibility condition (Eq. 2.17) and the definition of \hat{w} and $\hat{\eta}$, the full perturbation velocity field can be recovered at any time using the following relation

$$\underbrace{\begin{pmatrix} \hat{u} \\ \hat{w} \\ \hat{v} \end{pmatrix}}_{\mathbf{q}} = \underbrace{\frac{1}{k^2} \begin{pmatrix} i\alpha D_z & -i\beta \\ 1 & 0 \\ i\beta D_z & i\alpha \end{pmatrix}}_{\mathbf{C}} \begin{pmatrix} \hat{w} \\ \hat{\eta} \end{pmatrix}. \quad (2.32)$$

Moreover, equations (2.28 & 2.29) may be recast in a more compact vector notation by simply introducing the vector

$$q = \begin{bmatrix} \hat{w} \\ \hat{\eta} \end{bmatrix}. \quad (2.33)$$

The linear initial value problem equations (2.28 & 2.29) can be then re-written as

$$\frac{\partial q}{\partial t} = M^{-1} L_1 q = \hat{L} q, \quad (2.34)$$

where

$$M = \begin{bmatrix} k^2 - D_z^2 & 0 \\ 0 & 1 \end{bmatrix}, \quad (2.35)$$

$$L_1 = \begin{bmatrix} L_{OS} & 0 \\ i\beta U' & L_{SQ} \end{bmatrix}. \quad (2.36)$$

For the initial value problem, eq. (2.34), its solution can be expressed in the matrix exponential form as follows

$$q = \exp(\hat{L} t) q_0, \quad (2.37)$$

where q_0 is simply the initial condition vector, i.e., $q(t=0) = q_0$. Contrary to the modal analysis that focus on the perturbation amplitude, the kinetic energy would be a better measure of the short term perturbation amplification. The way to construct a standard Eulerian L_2 norm as an energy measure will be shown in more details in Appendix (B).

As indicated earlier, the main goal for the non-modal analysis is to find an optimum initial condition that leads to the maximum amplification of the perturbation kinetic energy. In other words, the interest is in identifying the maximum amplification, $G(t)$, of some initial perturbation energy over some given

time interval for different perturbation initial conditions. Hence, $G(t)$ can be defined as follows

$$G(t) = \max_{q_0} \frac{\|q(t)\|^2}{\|q_0\|^2} = \max_{q_0} \frac{\|F \exp(\hat{L} t) F^{-1} F q_0\|^2}{\|F q_0\|^2} = \|F \exp(\hat{L} t) F^{-1}\|^2, \quad (2.38)$$

where F is the result for a Cholesky decomposition of the matrix M (see Appendix (B for more details). Redefining the original operator, \hat{L} , as $FLF^{-1} = L$, the maximum amplification $G(t)$ is simply

$$G(t) = \|\exp(L t)\|^2. \quad (2.39)$$

Note that $G(t)$ is a result of an optimization over different initial conditions, q_0 . In other words, at any time t , the maximum possible energy amplification, $G(t)$, corresponds to a different specific initial condition q_0 . The matrix exponential solution given in (2.39), can be treated in three different ways, each of which describes a specific growth trend. Hereafter, these three different approaches will be briefly described (see Schmid 2007 for more details).

Traditionally, the *least stable mode* of L reveals *the asymptotic growth* trend ($t \rightarrow 0$). This least stable mode can be found using an eigen-value decomposition of L , i.e., $L = V \Lambda V^{-1}$, and hence the most unstable mode is considered as a characteristic quantity of the exponential operator

$$G(t) = \|\exp(L t)\|^2 = \|V \underbrace{\exp(\Lambda t)}_{\substack{\text{spectral} \\ \text{analysis}}} V^{-1}\|^2. \quad (2.40)$$

The spectral analysis, used to find the least stable eigen-mode, ignores any information about the eigenfunction of L contained in V . Hence, the least stable mode is only representative of the norm of the matrix exponential at all time when V is a unitary matrix, i.e., it has orthogonal eigenvectors. The matrix operator with a set of orthogonal eigenfunctions is referred to as normal

(Trefethen & Embree 2005). For a non-normal matrix operator, as in the case of L , a set of non-orthogonal eigenfunctions exist (Reddy et al. 1993) and the temporal behaviour of $G(t)$ is not well-represented by the least stable mode especially in terms of the intermediate and initial time limit. Alternatively, the concept of *numerical abscissa* (Trefethen & Embree 2005) is used to describe the early initial transient behaviour at $t = 0^+$. This numerical abscissa can be determined following an expansion of the energy growth rate about $t = 0^+$ for the matrix exponential solution (Schmid & Henningson 2001; Trefethen & Embree 2005). The aforementioned two trends, describe the initial and the asymptotic behaviour of the energy amplification. For the intermediate temporal behaviour, the $\varepsilon - \text{pseudospectra}$ approach (Trefethen 1997) is adopted to quantify the maximum transient energy growth (Schmid, 2007). In order to illustrate the different between those three sets, the variation of the energy growth of a general disturbance over time is shown as a schematic in Fig.2.3 (similar to Figure 3 in Schmid, 2007). In this schematic, the slope of the initial growth, that is governed by the numerical abscissa, is highlighted in blue. Whereas the asymptotic growth trend, governed by the least stable eigenvalue, is highlighted in magenta. Finally, the maximum reachable energy amplification, identified using the $\varepsilon - \text{pseudospectra}$ approach, is highlighted in red. In regards to the bypass transition, as will be shown late in the text, the focus will be of the intermediate time range to predict the maximum transient amplification.

As $G(t)$ is the representative function of the maximum energy amplification at any time t over all possible initial conditions, it is crucial to recognize the optimum initial perturbation associated with an amplification $G(t^*)$ at the given time, t^* . This initial condition can be recovered using the singular value decomposition (SVD) of the matrix exponential evaluated at time $t = t^*$ (Trefethen &

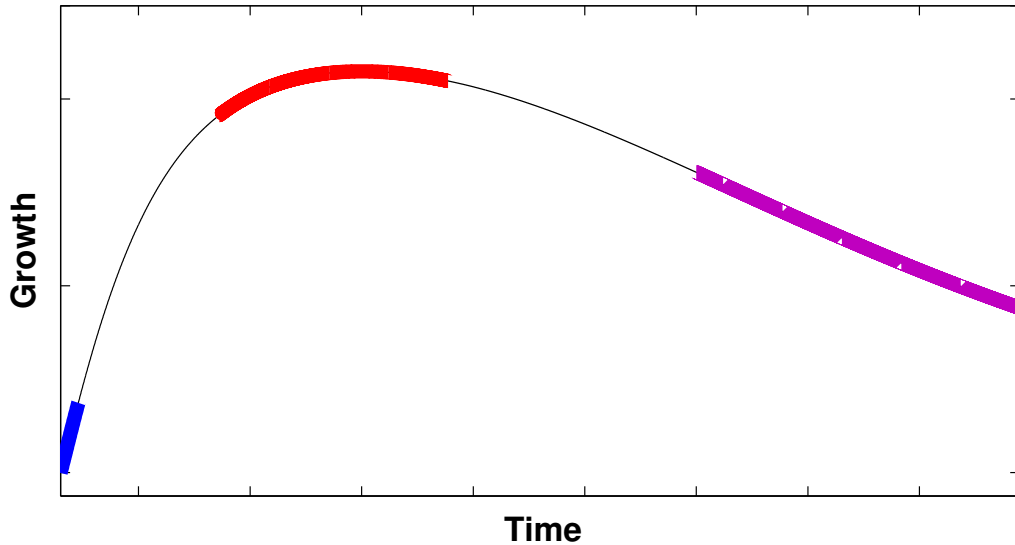


Figure 2.3: Schematic of the energy growth variation for a general disturbance. The colour differentiate between the sets governing the behaviour at different time limit. The the early initial trend, $t \rightarrow 0^+$, governed by the numerical abscissa (blue). The asymptotic trend , $t \rightarrow \infty$, governed by the least stable eigenvalue (magenta). In between, $0 < t < \infty$, the maximum transient energy growth, results of a resolvent norm size, is highlighted in red.

Embree 2005) as follows

$$S V D [exp(L t^*)] = Y \Sigma W^H \quad (2.41)$$

$$\Rightarrow exp(L t^*) W = Y \Sigma. \quad (2.42)$$

As can be interpreted from Eq. (2.42), $\Sigma(1, 1)$ represents $G(t^*) = \|exp(L t^*)\|$, the optimal initial condition is the left principal singular vector $\vec{w}_{op} = W(:, 1)$ and the output condition, i.e., after amplification, is the right principal singular vector $\vec{y}_{out} = Y(:, 1)$.

Transient analysis of the two-dimensional modal modes

In order to evaluate the effect of the transient nature of the base flow on the previously identified asymptotic mode, the perturbation evolution equation is reformulated similar to the initial value problem (2.34). Nevertheless, for a two-dimensional perturbation velocity is ought for

$$\tilde{w} = \widehat{w}(z, t) e^{i(\alpha x)}. \quad (2.43)$$

Note here, that Eq.(2.43) is equivalent to Eq.(2.26) with $\beta = 0$. Substituting Eq. (2.43) in Eq. (2.21), the general form of the linear initial value problem equation can be re-written, similar to Eq. (2.34), as follows,

$$\frac{\partial \widehat{w}}{\partial t} = L_1^n \widehat{w}, \quad (2.44)$$

where $L_1 = -L_{OS} / [k^2 - D_z^2]$. It must be emphasized that this transient analysis can be only performed for one mode at a time. To monitor the energy growth of the perturbation with time, the vertical perturbation kinetic energy q_{2D} is introduced and, for this two-dimensional case, can be calculated from the integration of $\widehat{w}(z, t)$ over the domain volume V as follows

$$q_{2D}(t) = \frac{1}{2} \int_V \widehat{w}^2(z, t) dV \quad (2.45)$$

CHAPTER 3

NUMERICAL METHODOLOGY

Since the presentation of our results first explores the linear stability analysis, the corresponding numerical tools are considered first here, followed by an overview of the computational scheme used within the fully nonlinear flow solver.

3.1 Linear stability analysis

For the numerical solution of either the classical eigenvalue problem, Eq. (2.24), or the initial value problem, Eqs. (2.34 & 2.44), a Chebyshev collocation method (Boyd 2013) is used in the discretization of the linear operators of the vertical velocity perturbation in Eq. (2.21), i.e., D_z^2 and D_z^4 , on Gauss-Lobato-Chebyshev grid points (GLC), as recommended by Orszag (1971), in order to ensure high accuracy. In the afterwards sections (3.1.1 & 3.1.2), a brief description on solving both eigenvalue and initial value problems will be given. For the initial value problem, the focus will be on the transient analysis associated with the 2D modal analysis.

3.1.1 Quasi-steady analysis: Eigenvalue problem

After assuming a wavelike solution for the perturbation, according to Eq. (2.23) the Orr-Sommerfeld equation (2.24) is solved to find the asymptotic solution for the individual frozen base velocity profiles under the “momentary” condition of

instability proposed by Blondeaux *et al.* (2012). The solution of such an equation consists of computing $\omega_i > 0$ according to (2.24)

$$i\omega_p(\bar{w}) = [k^2 - D_z^2]^{-1} [L_{OS}](\bar{w}) = L_1(\bar{w}) \quad (3.1)$$

This equation is solved for each individual base flow velocity profile, assuming that it is steady, and supplies a growth rate, ω_i , as a function of the perturbation wave number α .

3.1.2 Transient analysis: Initial value problem

Alternatively, for the initial value problem associated with the 2D modal modes, the evolution of the base flow is first sampled over equally spaced intervals of small duration $\Delta(\omega t) = 0.1^\circ$ within which it is safe to assume that the base flow is nearly steady. The length of this interval, i.e., $\Delta(\omega t)$, can be translated into an equivalent perturbation growth time, i.e., t_p , using the problem time scale (i.e., δ^*/U_{0m}). Within this $\Delta(\omega t)$ interval, the linear operator L_1 is considered constant for an individual mode. The Cranck-Nicolson scheme is then used in the temporal discretization of Eq. (2.44), using an equal time step of Δt_p to proceed from step n to step $n + 1$ for the each of the total interval time t_p as follows

$$\frac{\widehat{w}^{n+1} - \widehat{w}^n}{\Delta t_p} = \frac{1}{2} (L_1^n \widehat{w}^{n+1} + L_1^n \widehat{w}^n) \quad (3.2)$$

This approach takes into account the effect of the transient nature of the base flow on the cumulative growth of the perturbation. Recall that this analysis is only performed for a single streamwise mode. However, in this type of analysis, the transient growth is highly dependent on the vertical structure of the

initially inserted perturbation fields and on how close it may be to the most unstable eigenvector. To eliminate any resulting ambiguity, the evolution of the perturbation that is ultimately reported is the ensemble average over a total number of N simulations each of which has a different initial perturbation field with a random spatial distribution.

3.2 Fully non-linear Simulation

The two- and three- dimensional fully non-linear governing equations (2.10) and (2.11) are solved in a computational domain equivalent to an idealized box, corresponding to a fixed observer under the wave, where the velocity field is driven by a forcing term given by Eq. (2.5). The lateral domain boundaries are periodic boundary conditions whereas the top and the bottom boundaries are free-slip and no-slip boundary conditions, respectively. The resulting velocity field is then perturbed at an appropriately chosen time of insertion with a prescribed numerical noise field

The numerical method used to solve the problem governing equations is a spectral multidomain penalty method model (Diamessis *et al.* 2005). This pseudo-spectral model has been used to examine similar boundary layer flows associated with internal solitary waves (Diamessis & Redekopp, 2006), albeit in a rather different problem geometry. More details regarding the numerical model will be outlined in (3.2.1 - 3.2.3).¹

The spatial discretization relies on a Fourier discretization in the horizontal direction where N_x is the total number of equally spaced grid nodes in the span-

¹Taken from Appendix B of Diamessis and Redekopp 2006.

wise direction, and on a Legendre-polynomial-based single/multidomain discretization in the vertical. Additionally, explicit spectral filtering is employed in both spatial directions to eliminate any spurious numerical noise and preserve the high accuracy of the model (see section (3.2.3) for more details). In all simulations, the horizontal grid spacing, Δx , is less than $\delta/3$. In the vertical direction, at least between 12 and 15 grid nodes are located within one Stokes thickness δ to enable sufficient resolution of the developing BBL and of the subsequently generated vortex tubes.

For the purpose of validation, the numerical results of laminar cases, i.e., simulations in the absence of any external perturbation, are in a very good agreement with the analytical solution (see Appendix A).

3.2.1 Navier-Stokes splitting scheme

For the temporal discretization of eqs. (2.6 & 2.7), a high-accuracy pressure projection scheme is used (Karniadakis *et al.* 1991). According to this scheme, if one integrates eqs. (2.6 & 2.7) in time from level t_n to t_{n+1} the following semi-discrete equations, decomposed into three fractional steps for \mathbf{u} , are obtained (Diamessis *et al.* 2005):

$$\frac{\hat{\mathbf{u}} - \sum_{q=0}^{J_i-1} \alpha_q \mathbf{u}^{n-q}}{\Delta t} = \sum_{q=0}^{J_e-1} \beta_q \mathbf{N}(\mathbf{u}^{n-q}) , \quad (3.3)$$

$$\frac{\hat{\mathbf{u}} - \hat{\mathbf{u}}}{\Delta t} = -\nabla \phi^{n+1} , \quad (3.4)$$

$$\frac{\gamma_0 \mathbf{u}^{n+1} - \hat{\mathbf{u}}}{\Delta t} = \nu \mathbf{L}(\mathbf{u}^{n+1}) . \quad (3.5)$$

In the above, the forcing term, i.e., transient pressure gradient given in Eqs. (2.5), have been absorbed into the non-linear operator $\mathbf{N}(\mathbf{u})$ (see Eq. 2.11 for definition of linear and non-linear operator). The values of the coefficients α_q , β_q and γ_0 for the 3rd order backward differentiation-stiffly stable (BDF3-SS3) scheme of equations (3.3)-(3.5) may be found in (Karniadakis *et al.* 1991). The quantity ϕ^{n+1} :

$$\int_{t_n}^{t_{n+1}} \nabla \tilde{p} dt = \Delta t \nabla \phi^{n+1} . \quad (3.6)$$

is an intermediate scalar field that ensures that the final velocity \mathbf{u}^{n+1} is incompressible. In eq. (3.4), it is assumed $\nabla \cdot \hat{\mathbf{u}} = 0$ and the Poisson equation is solved for the pressure:

$$\nabla^2 \phi^{n+1} = \nabla \cdot \left(\frac{\hat{\mathbf{u}}}{\Delta t} \right) . \quad (3.7)$$

The boundary conditions for \mathbf{u} are enforced in eq. (3.5). Equation (3.7) utilizes the high-order accuracy dynamic boundary condition (karniadakis *et al.* 1991):

$$\frac{\partial \phi^{n+1}}{\partial z} \Big|_b = \sum_{q=0}^{J_e-1} \beta_q \mathbf{N}(\tilde{w}^{n-q}) \Big|_b - \sum_{q=0}^{J_e-1} \beta_q [\nu \nabla \times (\nabla \times \tilde{w})]^{n-q} \Big|_b . \quad (3.8)$$

where $|_b$ denotes $z = 0, H$ and the coefficients β_q have the same value as in the SS3 scheme of eqs. (3.3)-(3.5).

The splitting procedure for $\tilde{\rho}$ consists of two steps analogous to eqs. (3.3) and (3.5). The boundary conditions are enforced in the corresponding diffusive step.

3.2.2 Spectral multidomain penalty methods

In most of the cases simulated throughout this study, specially for the two-dimensional case, only a single vertical domain, i.e., no subdomains, is em-

ployed to avoid any numerical instability that may be introduced due to discontinuity at the subdomain interface in the highest Re cases considered. That said, the spectral multidomain penalty methods will be described ahereafter for the sake of completeness.

In under-resolved simulations, the absence of any artificial dissipation in the spectral discretization scheme leads to instabilities due to aliasing effects (Gottlieb & Hesthaven 2001) closely linked to under-resolved numerical/physical boundary layers (Deville *et al.* 2002). Specifically, Gibbs oscillations develop, which are most pronounced at the physical boundaries and subdomain interfaces and may generate catastrophically interacting artificial internal waves in a stratified flow. The crux of penalty methods (Hesthaven & Gottlieb, 1996; Hesthaven, 1997) lies in the fact that numerical instabilities arise in under-resolved simulations because boundary/patching conditions are explicitly enforced and there is no provision that the equation solved is satisfied arbitrarily close to the boundary/subdomain interface. By collocating a linear combination of the equation and boundary/patching conditions (the latter multiplied by a penalty term) at the corresponding spatial locations, the penalty method produces a smooth numerical solution with near-negligible error at the boundaries and interfaces. The spectral accuracy of the numerical scheme is negligibly impacted and one may compute stably the high Re internal dynamics of the flow without having to resolve the thin numerical/viscous physical boundary layers.

In terms of the splitting scheme outlined in section (3.2.1), the penalty method is applied at two different levels in the incompressible Navier-Stokes equations. The explicit non-linear term advancement is treated as a hyperbolic equation whereas the implicit viscous term treatment as a parabolic equation

(all subsequent equations in this section, i.e., (3.2.2), are written as a function of the u -velocity perturbation for the sake of demonstration and without loss of generality):

$$\frac{\partial u}{\partial t} = \mathbf{N}(u) , \quad (3.9)$$

$$\frac{\partial u}{\partial t} = v\mathbf{L}(u) . \quad (3.10)$$

The temporal derivatives in the equations (3.9)-(3.10) are only approximations to those appearing in eqs. (3.3)-(3.5). In both cases, the patching conditions are such that C_0 and C_1 continuity is enforced only weakly since the interface of two adjacent subdomains corresponds to the same location in physical space but to two separate grid-points. Thus, the penalty method is inherently discontinuous and it is this weak continuity on the numerical grid that allows for a more stable and smooth numerical solution at the subdomain interfaces.

Consider first eq. (3.9). The boundary conditions, imposed strictly in eq. (3.5), are not incorporated in the penalty treatment of the hyperbolic problem, which focuses solely on the subdomain interfaces. The penalty formulation of (3.9), in *physical space*, for each subdomain of index- k and uniform order $N_k = N$ is:

$$\frac{\partial u^k}{\partial t} = \mathbf{N}(u^k) - \tau_1^k Q_k^-(z_i^k) \left[\alpha u_0^k - g_1^k(t) \right] - \tau_2^k Q_k^+(z_i^k) \left[\gamma u_N^k - g_2^k(t) \right] , \quad (3.11)$$

where

$$Q_k^-(z_i^k) = \delta_{i0}, \quad Q_k^+(z_i^k) = \delta_{iN} . \quad (3.12)$$

here δ_{ij} is the Kronecker delta function with subscript i corresponding to the collocation point z_i^k . The terms in brackets represent appropriate patching conditions (Diamessis *et al.* 2005). The values of the coefficients α , γ , τ_1^k and τ_2^k are

determined by treating each individual subdomain as a single domain whose interfaces support patching conditions that act as open boundary conditions through which information is exchanged with adjacent subdomains. Essentially, the patching conditions are treated as localized open boundary conditions where each subdomain experiences “inflow” or “outflow” depending on the value of the vertical interfacial velocities W_0^k and W_N^k at the previous timesteps (Hesthaven & Gottlieb, 1996; Hesthaven, 1997; Diamessis *et al.* 2005).

The penalty formulation of (3.10) is significantly different from that of (3.9) due to its parabolic nature. After some manipulation (Diamessis *et al.* 2005), the discrete form of (3.10) may be written in Fourier space for an individual longitudinal wavenumber k_x as:

$$u - \epsilon D^2 u = \epsilon \frac{\hat{u}}{\nu \Delta t} = F , \quad (3.13)$$

where u is the value of the velocity at timestep $n + 1$. The small parameter ϵ is defined as:

$$\epsilon \equiv (k_x^2 - \frac{\gamma_0}{\nu \Delta t})^{-1} . \quad (3.14)$$

The penalty formulation of (3.13) is now:

$$\begin{aligned} & \epsilon D^2 u - u + F \\ & - \tau_1^k Q_k^-(z_i^k) \left[\alpha u_0^k - \beta \epsilon \frac{\partial u_0^k}{\partial z^k} - g_1^k(t) \right] \\ & - \tau_2^k Q_k^+(z_i^k) \left[\gamma u_{N_k}^k + \delta \epsilon \frac{\partial u_N^k}{\partial z^k} - g_2^k(t) \right] = 0 , \end{aligned} \quad (3.15)$$

where $Q_k^-(z_i^k)$ and $Q_k^+(z_i^k)$ are defined in (3.12). Again, the terms in the brackets represent appropriate patching/boundary conditions determined, in this case, by the elliptic nature of (3.13). At the physical boundaries, $g_1^1(t)$ and $g_2^M(t)$ are determined by the problem physical boundary conditions. The coefficients

α, β, γ and δ are set to one at each subdomain interface, and at the physical boundaries their values are set to satisfy the physical boundary conditions. The coefficients τ_1^k and τ_2^k for the discretized equations are determined by the type of the boundary/patching condition (Dirichlet, Neumann, Robin) under consideration (Hesthaven & Gottlieb, 1996; Diamessis *et al.* 2005).

Finally, the penalty treatment of (3.13) is applied to the Poisson equation for the pressure (3.7) in spectral space for any given longitudinal Fourier wavenumber k_x because (3.7) is a one-dimensional Helmholtz equation, as is the equation from which (3.13) originated .

3.2.3 Spectral filtering, adaptive interfacial averaging

Penalty methods are most effective in the vicinity of subdomain interfaces. To ensure stability of an under-resolved simulation in the subdomain interiors spectral filtering is used. In each subdomain, any function $f(z)$ may be approximated as (Boyd 2013):

$$f(z) = \sum_{j=0}^{N_k-1} \tilde{f}_j P_j(z) , \quad (3.16)$$

where \tilde{f}_j is the amplitude of the j -th Legendre mode and $P_j(z)$ the j -th order Legendre approximating polynomial (Boyd 2013). The filtered solution f^F may now be expressed in terms of the modes of the numerical solution as:

$$f^F(z_i) = \sum_{j=0}^{N_k-1} \sigma(k_j) \tilde{f}_j P_j(z_i) , \quad (3.17)$$

where k_j is the j -th discrete Legendre mode. In this study, an exponential filter function $\sigma(k_j)$ is used (Gottlieb & Hesthaven 2001):

$$\sigma(k) = \begin{cases} 1, & 0 \leq k \leq k_c , \\ \exp\left[-\alpha\left(\frac{k-k_c}{N-k_c}\right)^p\right], & k_c \leq k \leq N . \end{cases} \quad (3.18)$$

where p is the filter order, k_c the filter lag and $\alpha = -\ln \varepsilon_M$ with ε_M being the machine precision. In all simulations considered in this paper, $k_c = 0$. Application of the filter function (3.18) is equivalent to introducing a p -th order hyperviscous operator in the governing equations (Boyd 1998; Gottlieb & Hesthaven 2001). The hyperviscous operator is multiplied by an artificial viscosity $\epsilon_N \approx (1/N^{p-1})$ (Don *et al.* 2003). The advantage of the explicit application of a spectral filter is that it avoids the additional stiffness and subsequent timestep limitations of a hyperviscous term.

An analogous filtering procedure is applied in Fourier space. In the incompressible spectral simulations in this study, spectral filtering is applied at three levels when advancing the solution from time level (n) to level $(n+1)$ as described in detail in (Diamessis *et al.* 2005). The order of the Legendre and Fourier filters is the same in all three levels.

As shown by the spectral filter functions in figure 3.1, spectral accuracy is preserved because the direct effect of the filter never extends below the top 50% of the numerical solution modes in Fourier space and the first 8-9 Legendre modes in each subdomain. That is, the accuracy of the scheme remains at least $O(\Delta z)^8$ in the vertical direction while exponential convergence of the solution is always guaranteed in the horizontal. Use of an explicit spectral filter does imply an unavoidable reduction of effective Reynolds number. However, such a

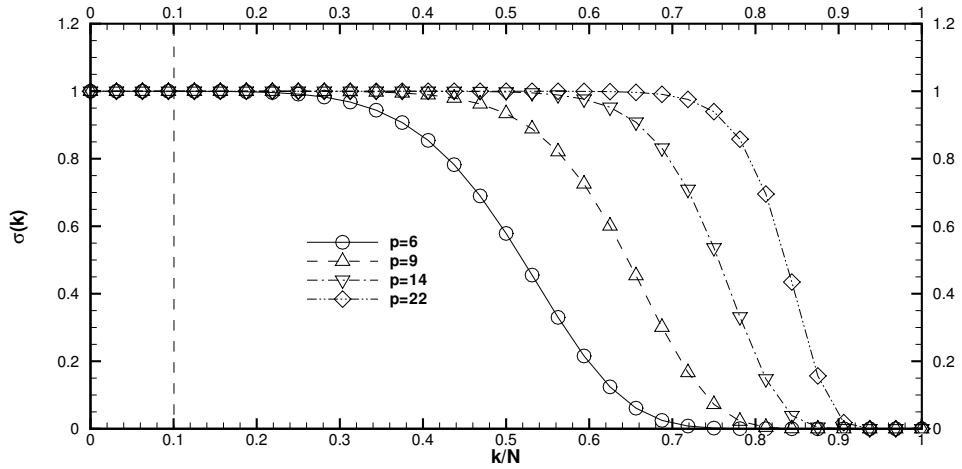


Figure 3.1: Exponential filter functions $\sigma(k/N)$ for different filter orders p representative values. The mode number and total number of available modes (over the full domain in Fourier space and over a single subdomain in Legendre space) are denoted by k and N , respectively. The dashed vertical line indicates the normalized wavenumber beyond which the artificial dissipation of a second-order finite-difference scheme has a direct effect, as shown by Domaradzki et al. (2002)

consequence is not only limited to higher-order methods (Levin *et al.* 1997; Slinn & Riley 1998). Low-order finite difference schemes are not damping-free, even if no filter is used. In fact, for resolutions typically employed in high Reynolds number simulations, their inherent artificial dissipation affects a broader range of resolved scales (Domaradzki *et al.* 2002) than the spectral filter functions in figure 3.1, thereby reducing even more the effective Reynolds number. In addition, no explicit control is possible over the amount of artificial dissipation introduced into the numerical solution. On the contrary, spectral filtering does possess this capability of explicit control as the filter order may be adjusted to damp adequately, but not excessively, any numerical noise due to under-resolution.

Caution is admonished in using the artificial viscosity coefficient , ϵ_N suggested by Don *et al.* (2003) to compute an effective Reynolds number (Winters & D' Asaro 1989). Such an attempt would imply attaching a physical significance to the spectral filter beyond its numerical role as a damper, especially when it is not totally clear what units should be assigned to the hyperviscosity in the vertical direction where the form of the corresponding hyperviscous operator is quite complex (Boyd 1998; Don *et al.* 2003). Computing the actual effective eddy viscosity as a function of numerical mode is quite an involved process (Domaradzki *et al.* 2002) which extends beyond the scope of this study.

CHAPTER 4

SAMPLE RESULTS

4.1 Classical Transition Analysis

The presentation of our results, in the context of modal analysis, is structured by our intention to illustrate the instability properties and associated dynamical response of the transient BBL under examination as a function of increasing Re_δ , much in alignment with the approach of SU10. First, the limits of applicability of the quasi-steady linear stability analysis, as a means of interpretation of the perturbation growth characterisers in the linear regime, are explored in the context of the transient nature of the base flow. The fully nonlinear solver is then used to examine the non-linear phase of BBL evolution which consists of the formation of vortex tubes and any interactions among them. Having demonstrated agreement with SU10's findings, we extend our study to a higher Re_δ , with a focus on the connection between the spacing of the observed vortex tubes and the most unstable mode as established through both linear stability analysis and fully nonlinear simulations.

4.1.1 Applicability of the quasi-steady linear stability analysis

In their study, Blondeaux *et al.* (2012) suggest that for small wave non-linearity (corresponding to small values of H^*/h^* , which they indicate to be the critical parameter determining the stability characteristics of the solitary wave-induced BBL) the "momentary" criterion of instability is not applicable. Hence, in this regime, quasi-steady linear stability analysis is not expected to provide accurate

results. However, the precise upper bound of this regime, expressed in terms of H^*/h^* , was not specified by Blondeaux *et al.* (2012).

In this regard, the scaling introduced in Eqs. (2.11 - 2.14) indicates that, at least for the transient BBL examined in this study, Re_δ is the sole non-dimensional parameter governing its instability response. To illustrate the presence of an upper bound of Re_δ , below which quasi-steady linear stability analysis is not applicable, the case with $Re_\delta = 211$ (equivalent to $Re = 2 \times 10^4$) is now examined with an emphasis on the disagreement between the quasi-steady and time-dependent approach. The applicability criterion is to be formally defined in the next page.

Quasi-steady asymptotic stability analysis is used to construct the contour map for $\omega_i > 0$ throughout the wave deceleration phase as shown in Fig. 4.1. Recalling the definitions in section 2.3.2, the maximum growth rate is $\omega_{i_{max}} = 0.0128$ and the critical wave phase occurs at $\omega t_c \approx 40^\circ$. The critical wave phase happens after the flow reversal which takes place at $\omega t \approx 30^\circ$ for all cases.

The next step is to solve the initial value problem associated with the transient analysis for the same case, i.e., $Re_\delta = 211$. As pointed out before, this type of analysis is only performed for an individual mode at once. Hence, we shall show the results for the first destabilized mode, i.e., the critical wavenumber, $\alpha_{(critical)} = 0.44$, as identified by the quasi-steady analysis. Across all Re_δ , the highest growth rates modes, i.e., $\alpha(\omega_{i_{max}})$, always lies within the range of $\alpha \in [0.43, 0.47]$. The critical wave number for $Re_\delta = 211$ happens to also be in this range as shown in Fig. 4.1.

The default approach for the transient stability analysis is to insert the per-

turbation at $\omega t = 0^\circ$ since any growth is only anticipated during the wave deceleration phase for this relatively low Re_δ value. The amplification factor, G_{2D} , is examined as a measure of the growth of the inserted perturbation amplitude. G_{2D} is defined as the kinetic energy based on the vertical velocity component, $q_{2D}(t)$, normalized by the initial energy level, $q_{2D}(t_0)$, at the time of insertion.

The evolution of the amplification factor for three modes representative of the highest growth rate α -interval defined above is shown in Fig. 4.2. The inserted perturbation amplitude undergoes an initial steep decay ($0^\circ \leq \omega t \leq 4^\circ$), and is then followed by a mild decay up to $\omega t = 100^\circ$ and then remains nearly constant. Although the quasi-steady analysis indicates a considerable perturbation growth, the transient analysis shows no growth but instead a continuous decay. Results from the corresponding two-dimensional DNS for this case, initialized with a low-amplitude white noise spectrum, (not shown here) confirm this continuous decay.

Having illustrated the disagreement between quasi-steady and transient stability analysis at a particular value of sufficiently low Re_δ , the lower limit of applicability of the former as a reliable descriptor of the instability of the transient BBL flow is identified through a series of numerical experiments over a range of gradually increasing Re_δ . The following applicability criterion is specifically proposed: The quasi-steady analysis is deemed to be valid if the degree of perturbation growth is such that, at least by the end of the wave event, the perturbation amplitude exceeds its original value. In other words, the amplification factor of the inserted perturbation has to become equal to one within the period of the solitary wave. Nevertheless, satisfaction of such a criterion does not guarantee the formation/appearance of vortex tubes as will be elaborated in section

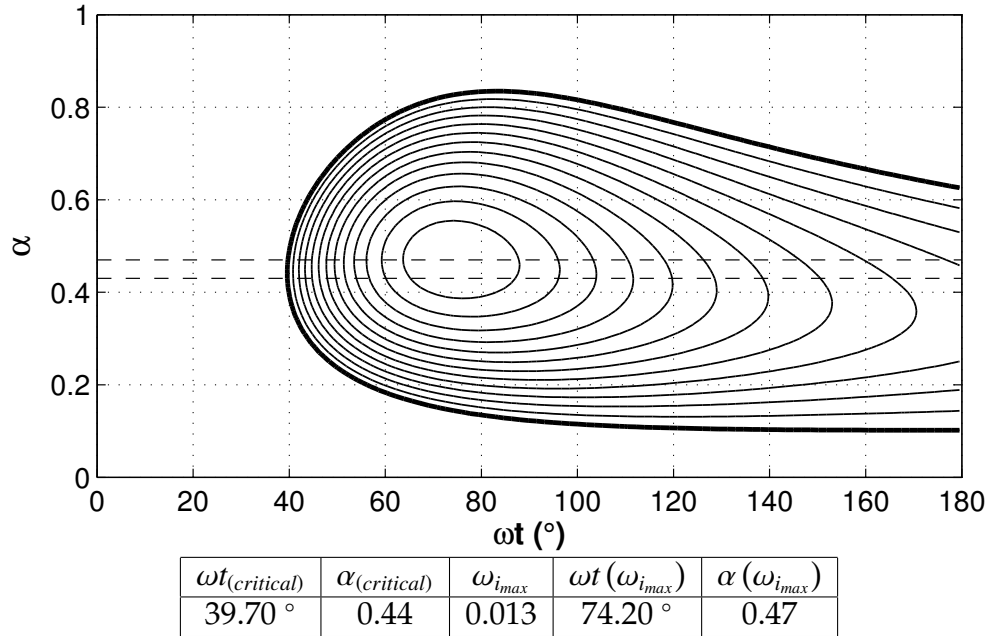


Figure 4.1: Growth contour of $\omega_i > 0$ for $Re_\delta = 211$ throughout the wave deceleration (thick solid line $\omega_i = 0$, contour value spacing $\Delta\omega_i = 0.001$ and $\omega_{i_{max}} = 1.28 \times 10^{-2}$). Horizontal dashed lines bound the modes with highest growth rates, i.e., $\alpha \in [0.43, 0.47]$. The table below the figure summarizes the following quantities: critical wave phase, critical wavenumber, maximum growth rate, wave phase of the maximum growth rate and the wavenumber with the maximum growth rate (see also section 2.3.2 for definitions).

4.1.2.

A representative example of amplification factor G_{2D} evolution curves for different Re_δ is shown in Fig. 4.3. The proposed criterion is first satisfied at $Re_\delta = 350$. The growth rate contour for this Re_δ case is shown in Fig. 4.4. What is interesting in this last figure, is that the critical wave phase is $\omega t_{(critical)} \approx 30^\circ$ when the flow reversal takes place. Therefore, a consequence of the amplification factor based criterion is that the applicability of the quasi-steady linear stability analysis for the transient base flow is intimately linked to the neutral curve crosses the near-bed flow reversal development threshold , i.e., $\omega t \approx 30^\circ$.

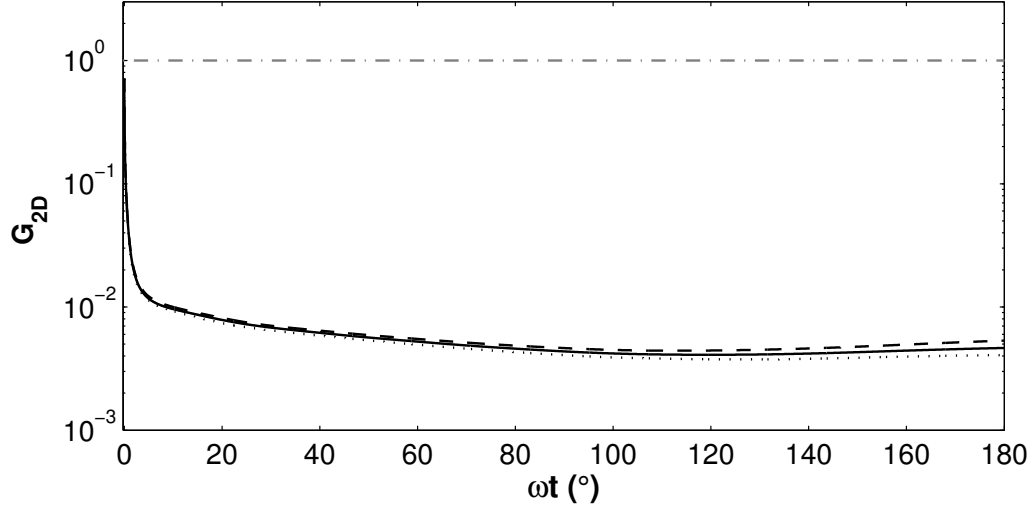


Figure 4.2: Time series for the normalized kinetic energy throughout the deceleration phase for $Re_\delta = 211$ for three wave numbers: $\alpha = 0.43$ (dashed line), 0.45 (solid line) and 0.47 (dotted line).

The applicability limit defined earlier is confirmed using DNS, which shows trends equivalent to those in Fig. 4.3. In DNS, the amplification factor of different individual modes are monitored. The modes are isolated by Fast Fourier transformation (FFT) the data in the streamwise direction at every time.

The next question is whether the T-S waves of instability can grow adequately to be noticeable, i.e., vortex tubes actually form. This happens when the amplitude of the velocity perturbation reaches the same order of magnitude of the base flow. In this case, the non-linearity will take over and will re-distribute non-negligible energy across different modes giving rise to the formation of vortex tubes. Vortex tube formation is, of course, hard to identify using any of the linear stability analysis alone since we neglect the non-linear term [Eqs. (2.18) and (2.19)] and, consequently, any kind of interaction among individual modes. The correct reproduction of nonlinear effects motivates the use of DNS to fur-

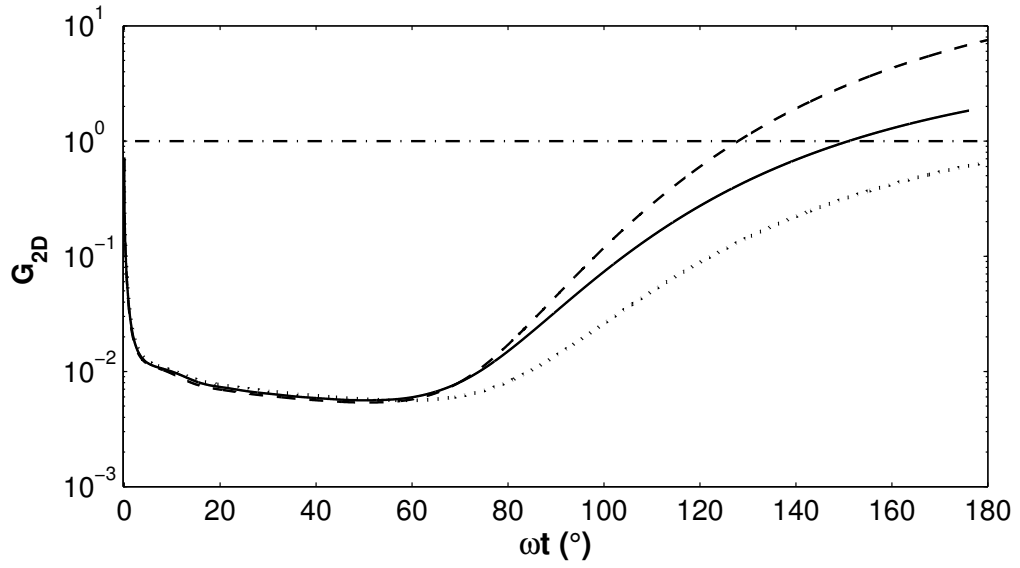


Figure 4.3: Times series for the normalized vertical perturbation kinetic energy for $\alpha = 0.45$ throughout the deceleration phase for $Re_\delta = 330$ (dotted line), 350 (solid line) and 375 (dash line).

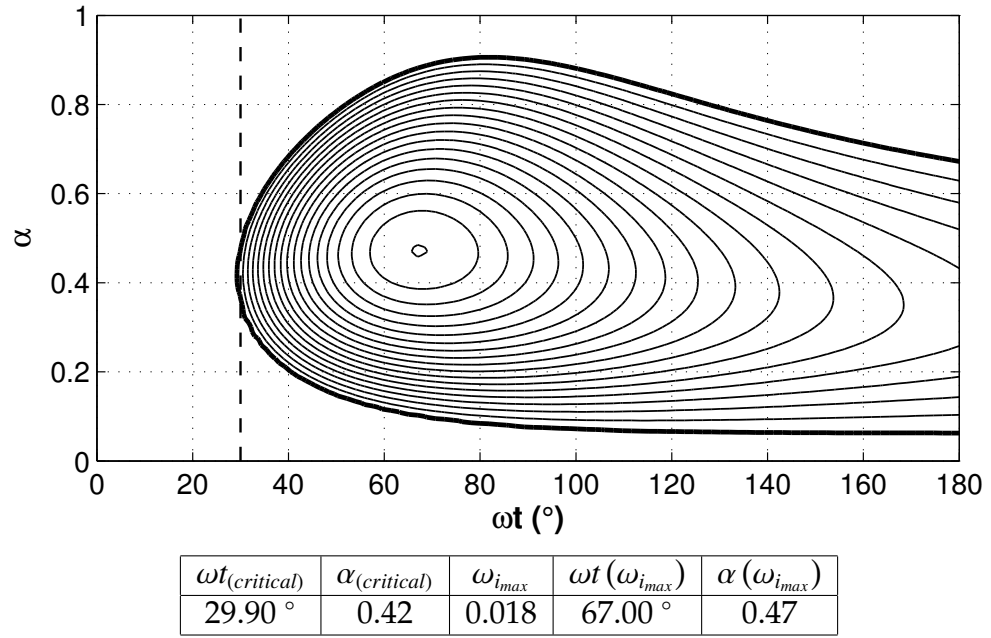


Figure 4.4: Growth contour of $\omega_i > 0$ for $Re_\delta = 350$ throughout the wave deceleration (thick solid line $\omega_i = 0$, contour value spacing $\Delta\omega_i = 0.001$). Vertical dashed line indicates the start of the flow reversal. Table quantities are as defined in the caption of Fig. 4.1.

ther explore the parameter range identified as linearly unstable.

4.1.2 Two-dimensional Direct Numerical Simulations

In this analysis, the goal is to identify the Re_δ limit above which the velocity perturbation will grow to an order of magnitude comparable to the base flow. The base flow then deviates from its laminar state as a result of the formation of coherent vortex structures. To trigger the instability in the numerical simulations, white noise is inserted with a prescribed small amplitude. This approach allows the reproduction of a wide range of possible instability modes. The inserted noise is designed to satisfy the divergence-free condition which already holds for the base flow. A sensitivity analysis (not shown here) has indicated that the two most important parameters associated with the introduced noise are its initial amplitude and insertion phase.

It is important to note that the initial amplitude of the inserted perturbation has to be much smaller than that of the base flow at the time of insertion. However, this was not the case in some previous studies (e.g. Vittori *et al.* 2011; Ozdemir *et al.* 2013). Use of a high initial amplitude noise , as compared to the base flow at the time of insertion, can induce some premature non-linear effects and can modify the linear instability response of the base flow in the wave deceleration phase. In this regard, the experiments of SU10, where presumably any ambient perturbations are relatively weak, did not report any deviation from the laminar state throughout the acceleration phase for their Re_δ value range, as indicated by their time series of the bed shear stress.

On the other hand, in the DNS, the insertion phase of the perturbation

can significantly impact the time of appearance of the vortex tubes. For instance, when a small perturbation is inserted at the wave initiation phase, i.e., $\omega t = -180^\circ$, the perturbation amplitude will undergo a steady viscous decay throughout the acceleration phase, namely for relatively lower Re_δ values. In this case, the perturbation amplitude at the critical wave phase is very small. Although the perturbation will eventually grow after this point, it will not be able to reach the order of magnitude of the base flow within the time scale of the wave event and the vortex tubes will never form.

Similarly, SU10 adopted the deviation of base flow from its laminar state and the associated flow structure to serve as a basis for the classification of the BBL flow under solitary wave. Such a deviation results from the base flow interaction with the same order of magnitude perturbation. This particular, more qualitative, classification is motivated by the capacity to observe the manifestation of the well-developed perturbation, in the form of generated vortex tubes, instead of identifying instability more quantitatively, as done using linear stability analysis through its focus on perturbation growth rates (section 4.1.1). Accordingly, in the discussion that follows, the linearly unstable regime of flow behaviour, earlier identified from the transient stability analysis, will be redivided into three regimes:

- Stable or Laminar (S) : no vortex tubes are formed regardless of the perturbation growth.
- Conditionally Unstable (CU) : the formation of the vortex tubes within the wave event is conditional on the initial perturbation amplitude and insertion phase.
- Unconditionally Unstable (UU) : vortex tubes are formed regardless of the

perturbation characteristics (i.e., initial amplitude or insertion time).

In the following sections, the results of the two-dimensional DNS analysis will be presented as an additional confirmation of this qualitatively/visually-based classification which is consistent with SU10's observations.

Conditionally Unstable Regime ($450 < Re_\delta < 1900$)

During the initial stage of this study, a general destabilization technique similar to what was adopted in some of the previous numerical studies (e.g. Vittori & Blondeaux, 2011; Ozdemir *et al.*, 2013) was considered.

As elaborated in the previous section, no perturbations are inserted at the very initial wave phase, i.e., $\omega t = -180^\circ$. When low in amplitude, these perturbations simply decay due to viscosity and cannot trigger any instability in the deceleration phase, whereas, when high, these perturbations can induce unrealistic non-linear instability during the acceleration phase that may have some effect on the subsequent deceleration phase instability as reported in a previous study (e.g. Ozdemir *et al.*, 2013).

Instead, the perturbation with the desired amplitude is inserted at the wave crest, i.e., $\omega t = 0^\circ$, as is done in the transient linear stability analysis (section 4.1.1). The extensive sensitivity analysis performed (not shown) has also indicated that inserting the noise at the initial stage or at the crest will result in the same response provided that the base flow is stable from the linear stability point of view. Additional numerical experimentation on our side, has shown that the appropriate maximum relative initial amplitude of the inserted perturbation is $O(10^{-3})$ to avoid the non-linear modification of the base flow.

Experimental results and observations at $Re_\delta = 920$ (equivalent to test number 8 in SU10, $Re = 4.4 \times 10^5$) provide a benchmark for comparison with numerical results for the conditionally unstable regime. For this specific Re_δ value, SU10 report the formation of an array of vortex tubes late in the deceleration phase. They also provide the time series of the bed shear stress measurement of this test case. In the corresponding numerical simulation, a maximum initial perturbation amplitude of $O(10^{-3})$, was inserted at the wave crest phase. The formation of vortex tubes near the bed was observed at $\omega t = 80^\circ$. The distance between two successive vortex tubes, which originate from the most unstable mode, for this Re_δ value case is $\lambda_x \approx 14.5$, which corresponds to $\alpha_x = 2\pi/\lambda x \approx 0.43$. SU10 reported an average spacing between the vortex tubes $\lambda_{sumer} \approx 14$ for this same range of Re_δ which is in good agreement with the distance obtained from our numerical simulations.

From the linear stability point of view, $\alpha_x = 2\pi/\lambda x \approx 0.43$ is in close proximity to both the critical wavenumber and the one having the largest growth rate (Fig. 4.5; See also the discussion on highest growth rate modes interval in section 4.1.1). An even more rigorous comparison is offered in Fig. 4.6, which shows the time series of both measured and calculated bed shear stress. The DNS time series of bed shear stress, sampled at different locations along the bed, agrees well with the corresponding time series from the experiment. Moreover, the phase at which the bed shear stress starts to deviate from the laminar solution, i.e., $\omega t \approx 80^\circ$, is related to the roll-up phase of the vortex tubes.

The other point to address here is the determination of the lower limit of this instability regime where vortex tubes are observed in the deceleration phase. Moreover, the source of any discrepancy with the experiment is also pursued.

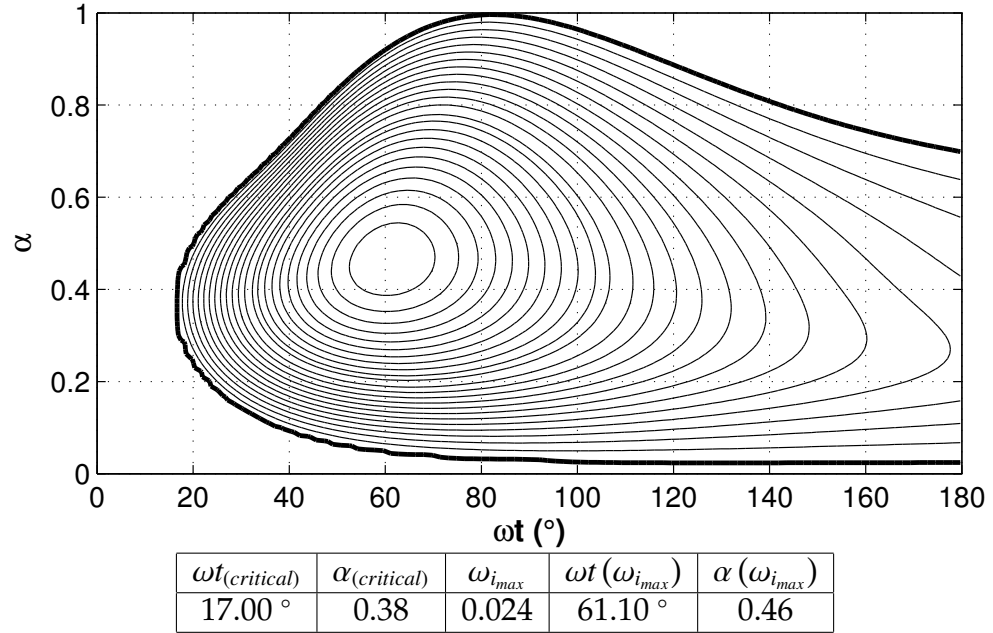


Figure 4.5: Growth contour of $\omega_i > 0$ for $Re_\delta = 920$ throughout the wave deceleration (thick solid line $\omega_i = 0$, contour value spacing $\Delta\omega_i = 0.001$). Table quantities are as defined in the caption of Fig. 4.1.

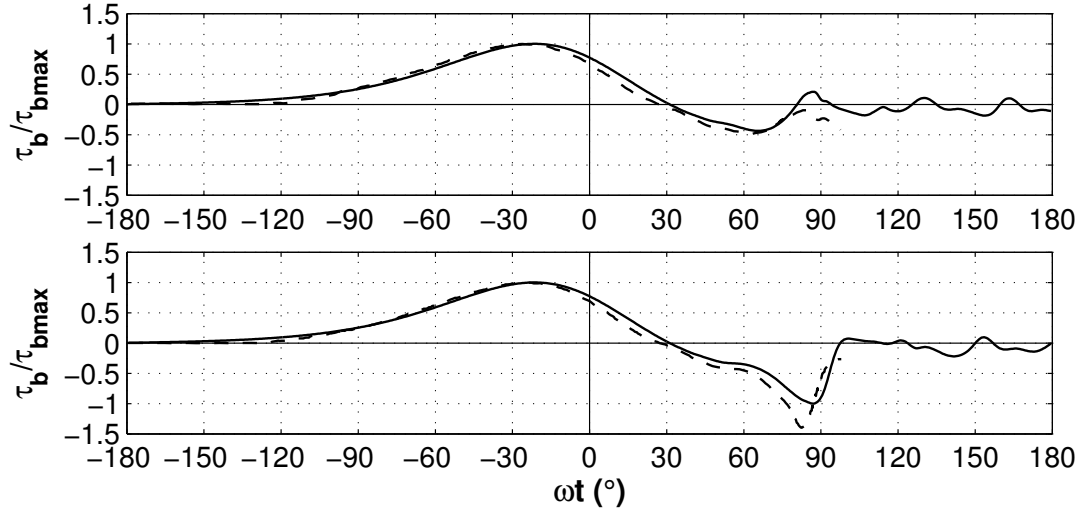


Figure 4.6: Time series of the normalized bed shear stress for $Re_\delta = 920$ at two different spatial locations. Solid lines represent DNS results whereas dashed lines represent laboratory measurements of SU10.

SU10 identified the lower limit of this regime, i.e., laminar flow with vortex tubes, as $Re = 2 \times 10^5$ ($Re_\delta = 630$). In contrast, Vittori & Blondeaux (2008 & 2011) identified a slightly higher Reynolds number limit, $Re = 5 \times 10^5$ ($Re_\delta = 10^3$). Vittori and Blondeaux suggested that the reason for their higher limit was due to presence of additional external sources of perturbations in the experiment (i.e., vibration, etc.). Although one may partially agree with this explanation, an additional interpretation behind their lack of observation of vortex tubes at lower Re is due to the insertion of their initial $O(10^{-4})$ perturbation into the initially quiescent velocity field, at $\omega t = -180^\circ$. Hence the perturbation undergoes a strong viscous decay in the acceleration phase as explained earlier. This interpretation has been confirmed by the subsequent work of Ozdemir *et al.* (2013) who also inserted the perturbation at the initially quiescent velocity field and observed the vortex tubes only when the amplitude of the initial perturbation was relatively high (approximately 20% of the max free stream velocity U_{0m}).

As for the different Re_δ limit identified by SU10 compared to Vittori & Blondeaux (2008 & 2011), and apparently this study, a more rigorous explanation may be offered. Following the same approach adopted for $Re_\delta = 920$, i.e., inserting the maximum possible perturbation amplitude $O(10^{-3})$ at the crest, the time series of the DNS bed shear stress is plotted against the laminar solution (Liu *et al.*, 2007) for $Re_\delta = 450$ case in Fig. 4.7. This figure is very similar to figure number 6 in SU10 where they compared the time series of the measured bed shear stress to the analytical laminar solution for $Re = 9.4 \times 10^4$ ($Re_\delta = 430$) case. SU10 disregarded their measurements/visualizations for $\omega t > 100^\circ$ due to the experimental limitation particular to the generation mechanism of the base flow driven by a soliton-like wave induced pressure gradient. In Fig. 4.7, the bed shear stress indeed follows exactly the laminar solution up to $\omega t = 100^\circ$.

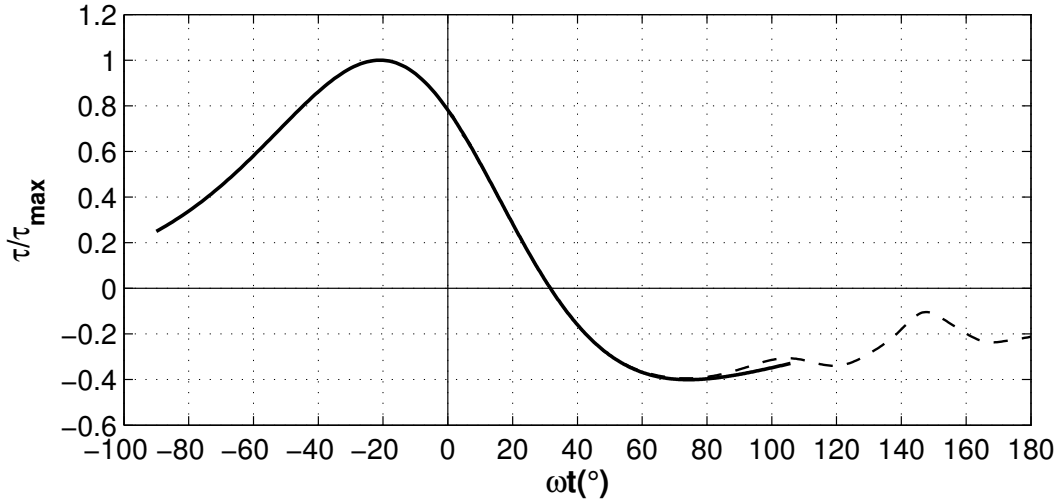


Figure 4.7: Time series of the normalized bed shear stress for $Re_\delta = 450$ for two case: the unperturbed case (i.e., analytical laminar solution, solid line) and perturbed case (dashed line) .

This explains why this Re case was classified by SU10 to be laminar.

However, the distortion observed in the DNS bed shear stress for $\omega t > 100^\circ$, reveals an interaction between the amplified perturbation and the base flow. This interaction manifests itself in a significant distortion of the near-bed parallel shear layer giving rise to the very initial stages of formation of a coherent vortex tube. According to our classification of instability regimes in the beginning of section (4.1.2), this Re_δ value is considered unstable. For any $Re_\delta \gtrsim 450$, with $O(10^{-3})$ perturbations introduced at $\omega t = 0^\circ$, vortex tubes arrays are expected to form as the result of the breakdown of the shear layer within the time scale of the wave event.

Unconditionally Unstable Regime ($Re_\delta > 1900$)

In this regime, the perturbation is inserted into the initially quiescent velocity field of the wave, i.e., $\omega t = -180^\circ$; viscous decay is not sufficiently strong to damp perturbation growth. Very low amplitude perturbation must be used in order to avoid the excitation of any non-linear instability in the acceleration phase. The non-dimensional relative initial perturbation amplitude is $O(10^{-12})$ to $O(10^{-8})$. To determine the lower Re_δ bound of this regime, a series of numerical runs were performed while increasing Re_δ . Since only the two-dimensional onset of instability and the formation of the coherent structures leading to the classical transition to turbulence are of interest, the base flow and perturbation are uniform in the spanwise direction. Hence, the formation of the turbulent spots, which can be an alternative mechanism to transition as observed in SU10, can not be simulated.

Starting with $Re_\delta = 1900$, the growth rate of the perturbation is high enough that the vortices will eventually evolve regardless of the initial amplitude of the perturbation as explained before. The unconditionally stable regime can be further divided into two main sub-regimes where the difference between them will be discussed later. The first sub-regime is for the interval $1900 < Re_\delta < 5000$, whereas the second sub-regime is for the interval $Re_\delta > 5000$. In the first sub-regime, the dominant unstable perturbation mode, i.e., the mode that sets the spacing between the generated vortex tubes, was found to be also the mode with the highest growth rate as computed by the quasi-steady linear stability analysis.

This mode has a wavelength of $\lambda_x \approx 15$ and it predominantly grows after the flow reversal. In the second sub-regime, i.e., $Re_\delta > 5000$, the wave length

of the most unstable mode increases to $\lambda_x \approx 21$. This wavelength corresponds to the first destabilized mode, although it is not necessarily the fastest growing one. This longer mode predominantly grows before the flow reversal phase (i.e., $\omega t < 30^\circ$). When $Re_\delta \geq 7900$, the base flow starts to be destabilized in the acceleration phase of the wave, before the occurrence of the adverse pressure gradient and the associated formation of the inflectional point in the velocity profile. Such an instability response suggests a viscous origin of the instability, similar to what is observed in the plane Poiseuille or Blasius boundary layer flows (see Criminale *et al.* 2003 for details).

The evolution of the amplification factor G_W of each of the most unstable modes for the different Re_δ cases is shown in Fig. 4.8 . G_W is the equivalent of the amplification factor G_{2D} used earlier in the transient linear stability analysis (section 4.1.1), although it is defined for a particular mode of interest and not for the entire flow field. The dotted curves in Fig. 4.8 represent the transient variation of G_W for dominant perturbation wavelength, i.e., $\lambda_x \approx 15$, in the first sub-regime, i.e., $1900 < Re_\delta < 5000$. The solid curves are representative of the transient variation of G_W in the second sub-regime, i.e., $Re_\delta > 5000$, where the wavelength of the most unstable mode is $\lambda_x \approx 21$. As shown in this figure, G_W undergoes a consistent growth until it reaches a plateau at the time when the coherent vortex tubes forms. The figure also shows that the growth rate of the most unstable mode increases as the base flow Re_δ increases, which agrees with the quasi-steady linear stability analysis (e.g. Figs. 4.4 and 4.5).

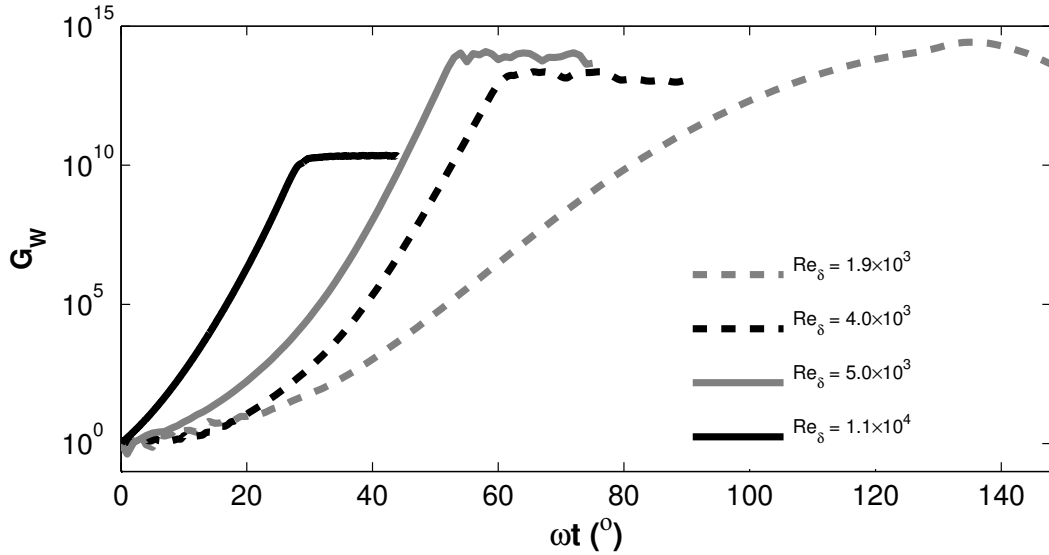


Figure 4.8: Transient growth as characterized by sample curves of amplification factor G_W of the most unstable mode for the two categories of the unconditionally unstable regime. Dashed lines correspond to the growth of the $\lambda_x \approx 15$ mode whereas solid lines represent the $\lambda_x \approx 21$ mode.

4.1.3 Three-dimensional Direct Numerical Simulations

The last element, related to the classical transition scenario, is the breakdown of the developed vortex tubes due to the secondary spanwise instability. In order to elucidate the breakdown process of the vortex tubes, a characteristic flow case, $Re_\delta = 1833$, will be presented as an example.

The computational domain, for this $Re_\delta = 1833$ case, is of size equal to $64 \times 16 \times 29$ non-dimensional units along (x, y, z) directions, respectively. The grid size is chosen to be small enough to allow for the formation of smaller scale instabilities with respect to the secondary spanwise one, though not for the full spectrum of turbulent motions. Because the flow is evolving with time, the maximum wall shear stress of the unperturbed laminar case, that takes place

at $\omega t = -20^\circ$ (see Fig.4.7), is used a representative value to express the grid resolution in terms of the wall, $+$, units. However, the actual value of the bed shear stress, at the wave phase that corresponds to the transition to turbulence, deemed to be smaller.

For this specific flow case of $Re_\delta = 1833$, the grid size in both uniform stream- and spanwise periodic directions are $\Delta x^+ = \Delta y^+ = 11.5$. In the non-homogeneous wall-normal direction, the minimum grid spacing is $\Delta z^+ = 0.22$, adjacent to the bed, and the maximum spacing is $\Delta z^+ = 14.1$, located at the mid-height of the domain (equivalent to $z^+ \approx 662$). Furthermore, six points exist within the viscous sub-layer ($z^+ \leq 5$). The order of the Legendre and Fourier filters is 8 & 10, respectively (see section 3.2.3).

According to the earlier classification in section (4.1.2), this Re_δ case lies on the limit between the conditionally and unconditionally unstable regimes. Hence, the instability is triggered following the established method described earlier, i.e., the base flow is perturbed just before the wave crest, inserted at $\omega t = -2^\circ$ in this specific case. However the inserted perturbation has slightly different specifications. The major difference is related to the induction of the secondary instability which requires that the inserted perturbation has a spanwise dependence. Therefore, the inserted perturbation has two components: a streamwise noise with an initial non-dimensional amplitude of the order of $O(10^{-4})$ and a secondary spanwise periodic noise of initial amplitude of $O(10^{-6})$.

In general, the breakdown process involves four successive stages. The process starts with the formation of the 2D coherent structure as an outcome of the development of the Tollmien-schlichting wave (T-S), i.e. streamwise perturbation, followed by the induction of a spanwise secondary instability. The mat-

uration of this secondary instability results in the deformation of the equally spaced vortex tubes which eventually breaks down into a chaotic flow field.

In order to illustrate these stages, a series of snapshots of the evolution of the λ_2 -contours (see section 1.2.3 for definition) are shown for the characteristic $Re_\delta = 1833$ case in Fig 4.9. In Fig.4.9(a), the 2D vortex tubes, uniformly extended in the y -direction, are equally spaced in the streamwise direction. Fig.4.9(b) illustrates the development of a secondary streamwise instability. This instability can be viewed as the instability of the developed vortex tubes interacting with the wall and the image vortex beneath it. This may be some form of elliptic instability linked to the interaction of two vortices (e.g. Sipp & Jacquin, 2003; Meunier *et al.*, 2005). Further work is needed to verify this conjecture. In the middle row of Fig.4.9, i.e.,(c & d), the secondary spanwise periodic instability grows to the extend that it starts to disrupt the spanwise uniformity of the vortex tubes and gives rise to the formation of tangles of vortex filaments. The non-linearity of the flow enhances the formation of these tangles of vortex filaments which, eventually, interact among each other leading to a chaotic state as shown in Fig.4.9(e & f). Some of those vortex filaments takes the form of Λ -shaped vortices. This will be discussed in more detail later in chapter (5).

4.2 Bypass Transition Analysis

The main aspect of this section is the identification of the optimum initial disturbance that will eventually leads to the formation of streamwise streaks. These streaks breakdown, in response to a secondary instability, and evolve to form localized turbulent spots that eventually leads to the bypass transition.

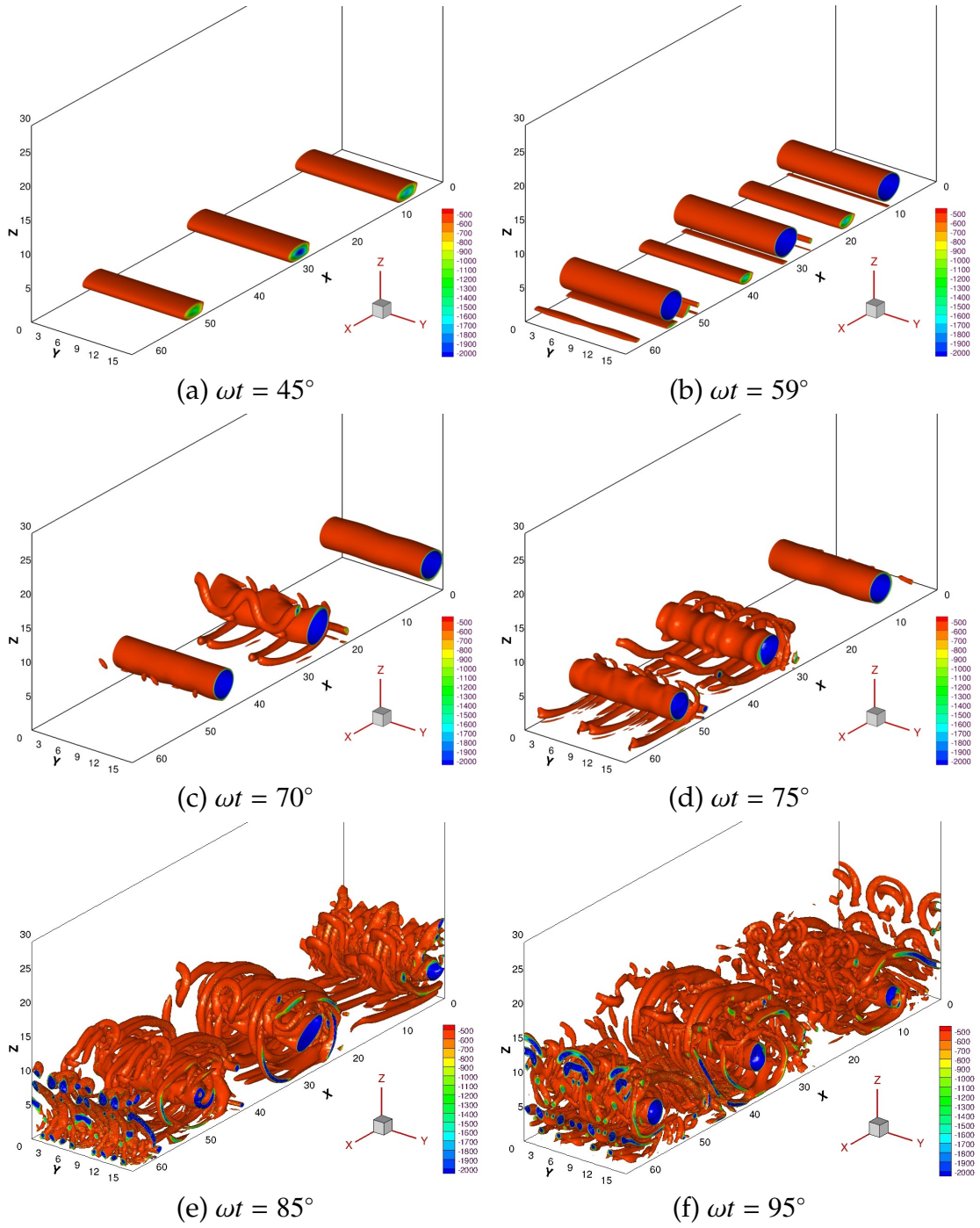


Figure 4.9: Iso-contours of λ_2 for $Re_\delta = 1833$ case at different wave phase (ωt). The horizontal and vertical coordinates in each panel are normalized by the boundary layer thickness δ .

The non-modal linear stability analysis is first employed to characterize this initial disturbance and also to demonstrate that, for the transient base flow of interest, an infinite streamwise disturbance, i.e., $\alpha = 0$, can have a significant short-term algebraic growth even when the base flow is deemed to be asymptotically stable as per the eigenvalue analysis. The next step consists of perturbing the base flow, in the DNS, using the identified optimum disturbance and quantifying the overall energy growth and hence the formation of the streaks.

4.2.1 Quasi-steady transient stability analysis

Similarly to the two-dimensional case, the first step in studying the transient growth of the different modes consists of performing a quasi-steady profile analysis. In this analysis, the base flow, i.e., a specific ωt profile, is assumed steady over a total time span \hat{t}_p that is linked to the non-dimensional wave period, T , according to the following relation

$$\hat{t}_p = \left(1 - \frac{\omega t}{180}\right) \times \frac{T}{2} \quad (4.1)$$

where $T = T^* \times (U_{0m}^*/\delta^*)$ (see sections 2.1 & 2.2 for definition). This transformed non-dimensional time scale, t_p , is employed in the linear transient stability analysis. A schematic that shows the variation of \hat{t}_p with respect to the different ωt -profiles is highlighted in Fig. 4.10 for base flow profiles sampled at different ωt .

Recall from sec. 2.3.3, the main goal of the non-modal analysis is to identify the temporal variation of the amplification factor, G , for different combination of stream- and spanwise wavenumbers, i.e., $(\alpha; \beta)$, respectively, and hence identify the most critical combination, in terms of energy amplification, for a specific

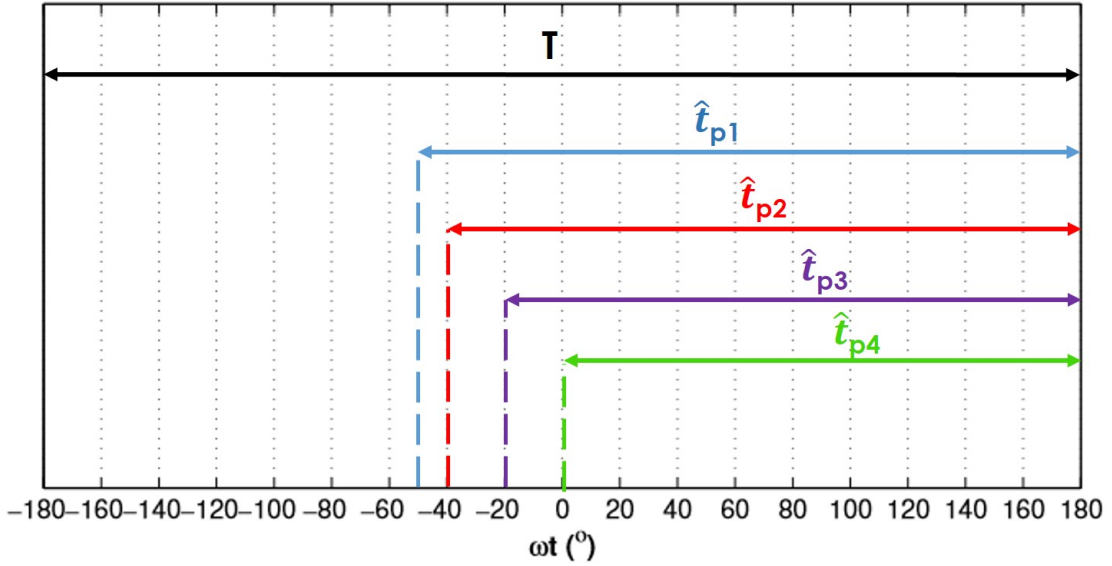


Figure 4.10: Variation of \hat{t}_p for different ωt velocity profiles. Colours refer to the different ωt : -50° , -40° , -20° & 0° .

profile. Accordingly, a parametric study of transient growth for a characteristic sample for $Re_\delta = 1478$ case is shown hereafter. Fig. 4.11 portrays the variation of the amplification factor (G) contours, normalized by the corresponding maximum value, as function of $(\alpha; \beta)$ for six different base flow profiles. In terms of higher energy amplification, the predominance of the streamwise independent structures, i.e., $\alpha = 0$ is observed in Fig.4.11(a-e), specially when no exponential growth is expected, i.e., the base flow is asymptotically stable. The dark gray area in $\alpha - \beta$ plane, shown in Fig.4.11(f), indicates much higher amplification values that results from an asymptotic exponential growth for those parameter combinations.

The critical $(\alpha; \beta)$ combination; i.e., combination with the maximum energy amplification factor G_{max} ; can be identified from the contour sub-plots for each profile. Throughout the time span $0 \leq t_p \leq \hat{t}_p$, the temporal variation of the amplification function $G(t_p)$, for the six different critical $(\alpha; \beta)$ combinations, is

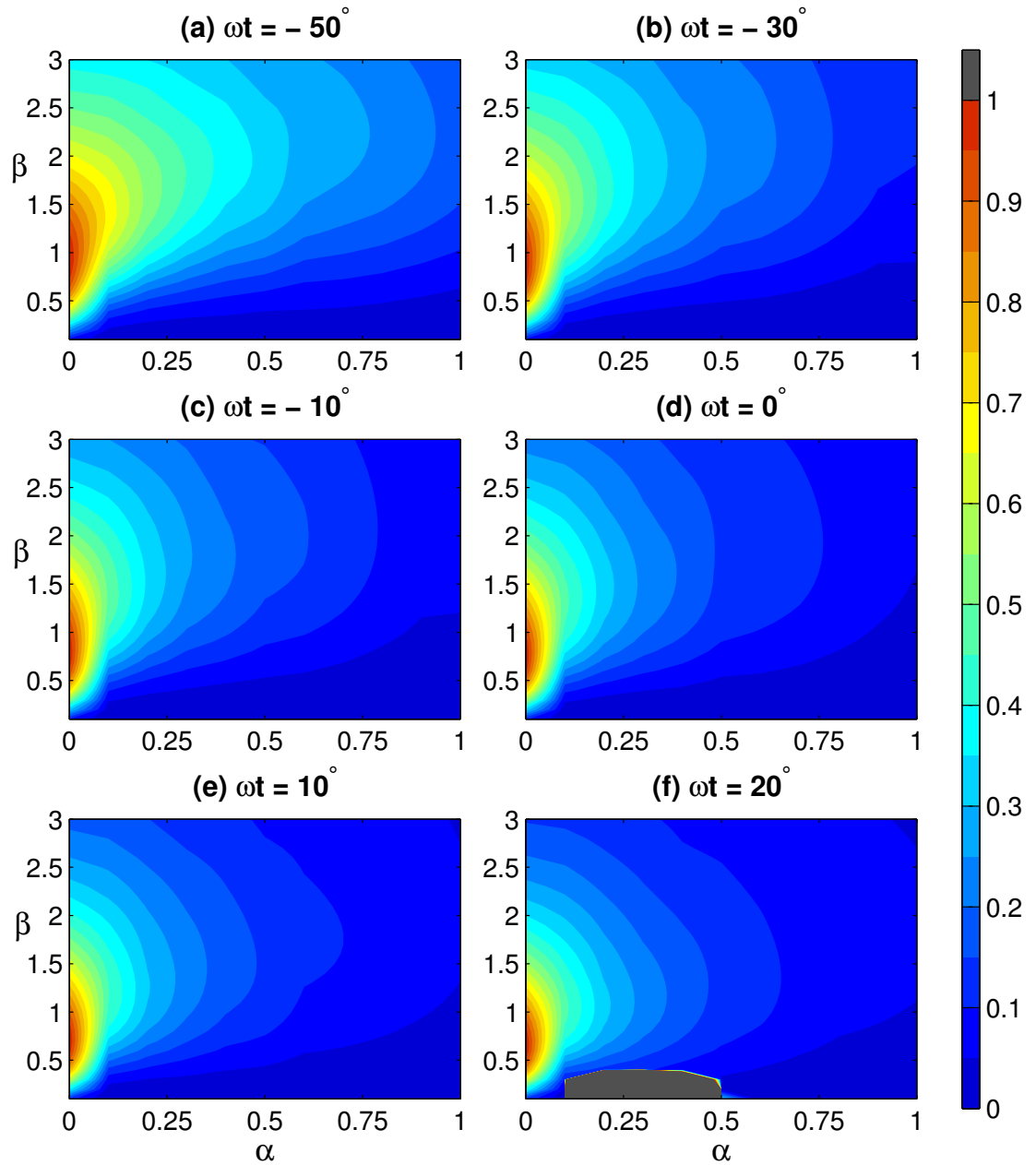


Figure 4.11: Parameter study of the amplification factor G (normalized by the corresponding maximum value) as a function of the streamwise (α) and spanwise (β) wave number for six different base flow profiles of $Re_\delta = 1478$ case. the dark grey area in the $\alpha - \beta$ plane in Fig.4.11(f) corresponds to an asymptotic exponential growth.

presented in Fig. 4.12. However, for the base flow profile case corresponding to $\omega t = 20^\circ$, the amplification function $G(t_p)$, shown in Fig. 4.12, represents the maximum algebraic growth rather than the asymptotic growth that produces a much higher values (dark grey region highlighted in Fig.4.11(f)). The last two figures, i.e., Figs. 4.11 & 4.12, reveal a few important features:

- An appreciable energy amplification can take place even if the base flow is asymptotically stable, i.e., in the wave acceleration phase (see Fig. 4.14).
- The highest transient energy amplification response is associated with perturbation modes with no streamwise dependence ($\alpha = 0$) in contrast to classical results from the modal stability analysis.
- Across the different base flow profiles, the highest transient energy amplification is associated with ($\alpha = 0$) and $\beta \in [0.7, 1.0]$. This point will be addressed in more details in 5.2.1.
- The non-modal instability stimulates an early, i.e., in the short term, high amplification growth followed by an asymptotic decay. Hence, the base flow is deemed to be stable according to the classical eigenvalue analysis which is focused on the long term behaviour of the base flow. This high initial energy growth, using an appropriate secondary instability, can lead to non-linear state as will be showed later (e.g. 4.2.2).

The last feature is illustrated in Fig. 4.13 where the difference between algebraic and exponential amplification is shown for the base profile corresponding to $\omega t = 20^\circ$ of $Re_\delta = 1478$ case. For the sake of completeness, the two-dimensional, i.e., $\beta = 0$, asymptotic growth rate contour for this $Re_\delta = 1478$ case is presented in Fig. 4.14. This figure shows that the mode with the highest

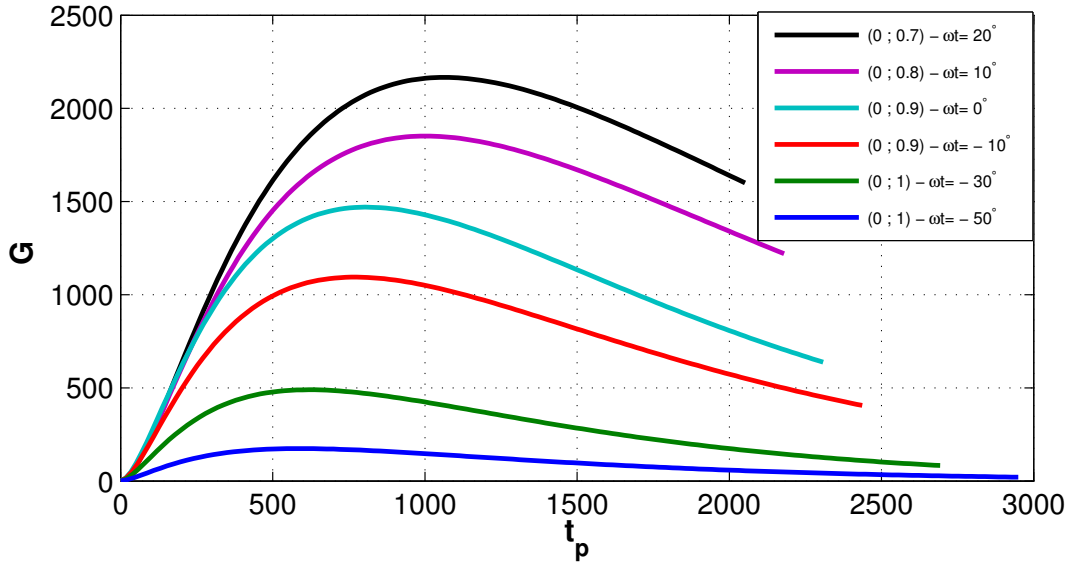


Figure 4.12: Temporal variation of the amplification function $G(t_p)$ corresponding to the critical $(\alpha; \beta)$ combination, i.e., combination leading to the highest algebraic growth, for six different base flow profiles of $Re_\delta = 1478$ case. Critical $(\alpha; \beta)$ combination and corresponding base profile wave phase ωt are reported in the figure legend.

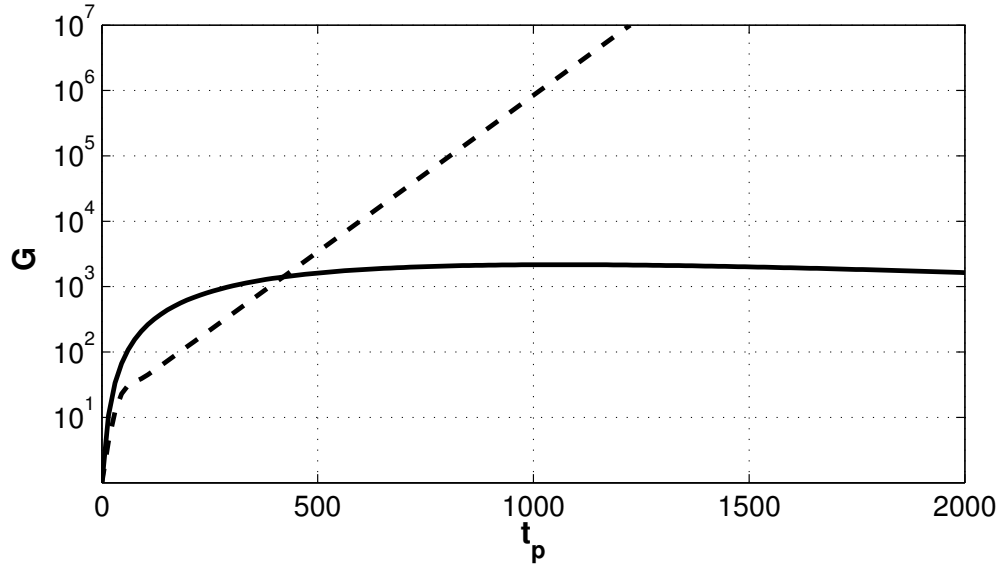


Figure 4.13: Comparison between amplification function $G(t_p)$ variation as a result of either algebraic or exponential growth for base profile corresponding to $\omega t = 20^\circ$ of $Re_\delta = 1478$ case. The dashed line, sample of exponential growth, corresponds to $(\alpha; \beta) = (0.3; 0)$. Whereas the solid line, sample of algebraic growth, corresponds to $(\alpha; \beta) = (0; 0.7)$. G -axis in log-scale.

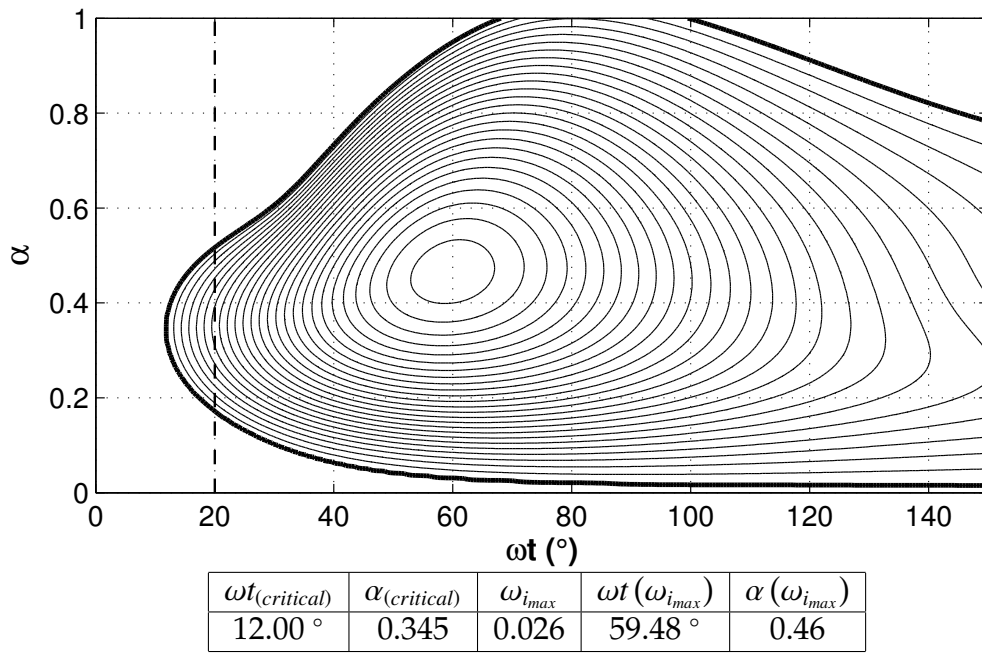


Figure 4.14: Growth contour of $\omega_i > 0$ for $Re_\delta = 1478$ throughout the wave deceleration (thick solid line $\omega_i = 0$, contour value spacing $\Delta\omega_i = 0.001$). Table quantities are as defined in the caption of Fig. 4.1. Vertical dashed line corresponds to $\omega t = 20^\circ$.

asymptotic growth for the base flow profile $\omega t = 20^\circ$, distinguished by a vertical dashed line lies between $0.3 < \alpha < 0.4$ and exactly equal $\alpha = 0.35$. In addition, the critical wave phase for the $Re_\delta = 1478$ case is found to be $\omega t_{(critical)} = 12^\circ$ which means that, from a modal point of view, all base flow, prior to this wave phase, are deemed stable with no growth anticipated for any mode having $\beta = 0$ (in contrast to what has been demonstrated in Fig. 4.11).

4.2.2 Three-dimensional Direct Numerical Simulation of streak formation

In this analysis, the goal is to employ the findings of the quasi-steady transient stability analysis to replicate the formation of the streaks, eventually developing into turbulent spots, for the temporally evolving based flow. As previously done in section 4.2.1, a representative Re_δ case will be explored in detail. In order to complement with the results reported in the previous section 4.2.1, the $Re_\delta = 1478$ case will be adopted hereafter. Additionally, this Re_δ value is susceptible to the formation of the turbulent spots (as per SU10 observation).

Optimum initial noise

The first step to induce the streaks formation is by identifying the optimum initial perturbation that undergoes the maximum energy amplification. The optimum initial perturbation can be identified from the quasi- steady transient analysis for individual profile as described earlier in 4.2.1. This optimum initial perturbation is associated with the critical $(\alpha; \beta)$ combination for a specific ωt profile. However, the persistence of this critical $(\alpha; \beta)$ combination for successive profiles may suggest a cumulative increase similar to what is observed for the two- dimensional asymptotic analysis (more elaboration in 5.2.1). As an additional measure of ensuring such cumulative growth, a linearly combination of four optimum initial perturbation fields will be inserted. Each field of those four is associated with a combination of $(\alpha; \beta)$, specifically $(\alpha = 0; 0.7 \leq \beta \leq 1.0)$. The reasoning behind this approach will be elaborated later in 5.2.1. For the representative case of $Re_\delta = 1478$ shown hereafter, the inserted optimum initial

perturbation field associated with the $\omega t = -25^\circ$ profile is shown in Fig. 4.15.

DNS with optimum initial noise

In order to trigger the streak formation, a DNS simulation is conducted where the predetermined optimum initial disturbance is inserted into the temporally evolving base flow at a specific wave phase. This insertion phase has to be earlier than $\omega t = -25^\circ$ which corresponds to wave phase of the quasi-steady profile adopted in the optimum disturbance calculation. Therefore, it is chosen to insert this optimum initial perturbation into the temporally evolving base flow at $\omega t = -28.8^\circ$ to allow for flow adjustment to such disturbance before the anticipated resonant profile, i.e., $\omega t = -25^\circ$. Additionally, as discussed earlier in 4.1.2, the amplitude of such a disturbance has to be small, relative to the base flow, to avoid any undesirable non-linear response. Accordingly, the maximum initial amplitude of this disturbance, for any of the three velocity component of the disturbance, is of $O(10^{-3})$ with respect to U_{om}^* . Another measure of the perturbation amplitude is the total kinetic energy of perturbation, Ke_{pert} , which is defined as

$$Ke_{pert} = \iiint_V (\tilde{u}^2 + \tilde{w}^2 + \tilde{v}^2) dV, \quad (4.2)$$

where $(\tilde{u}, \tilde{w}, \tilde{v})$ are the perturbation velocity component (see 2.3.1). For this case, the Ke_{pert} at the time of insertion is of order $O(10^{-6})$ with respect of the unperturbed base flow kinetic energy at the time of insertion.

The computational domain adopted for this $Re_\delta = 1478$ case, is of size equal to $61 \times 13 \times 23$ non-dimensional units along (x, y, z) directions, respectively. Following the same approach described earlier in 4.1.3, the grid resolution for this

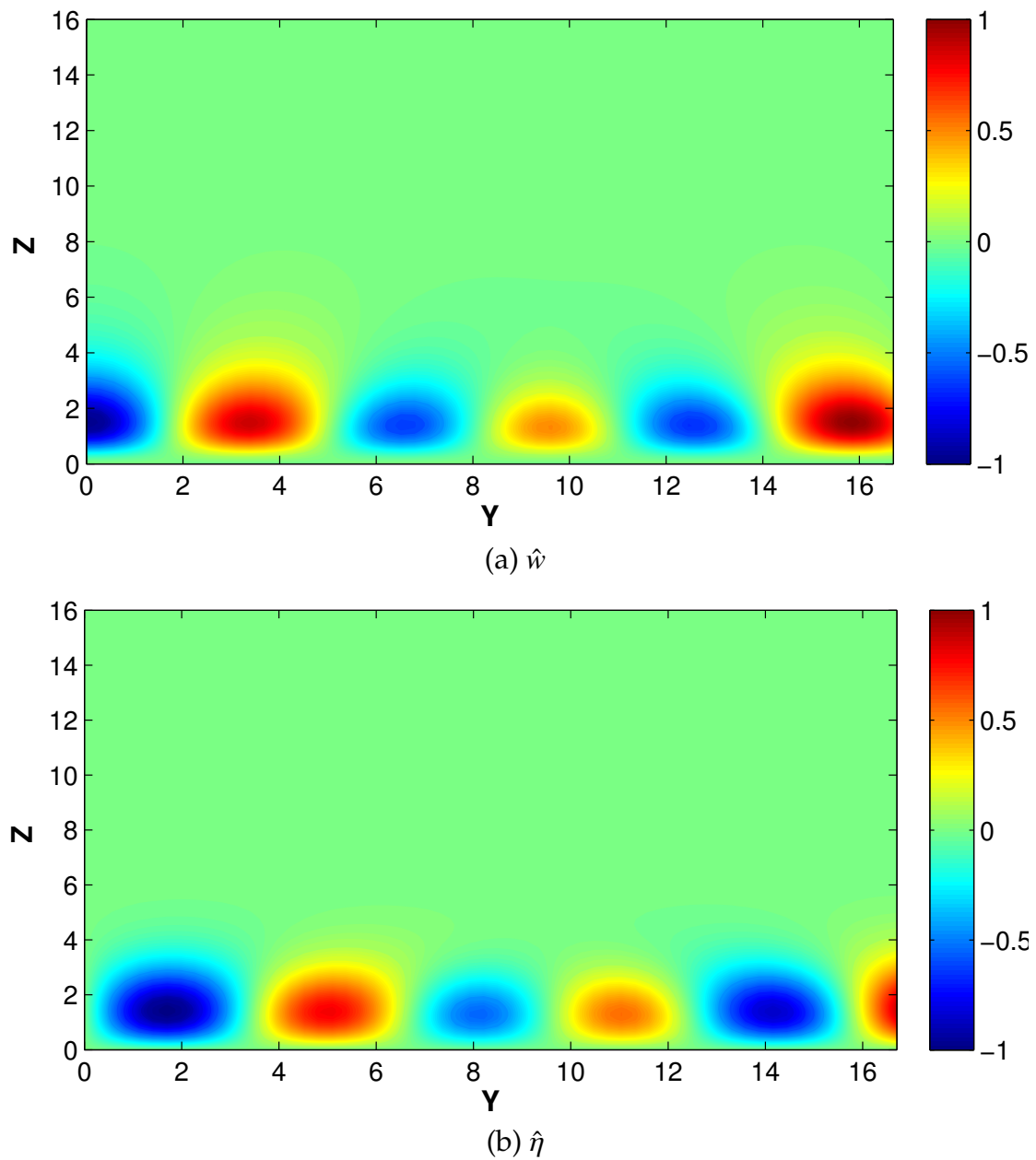


Figure 4.15: Normalized contour plot of the optimum initial disturbance shape in the y - z plane associated with the maximum energy amplification for velocity profile $\omega t = -25^\circ$ for $Re_\delta = 1478$ case. Upper panel (a) shows the wall normal perturbation velocity field \hat{w} , whereas panel (b) shows the wall normal vorticity field $\hat{\eta}$ (see 2.3.3 for definition). The vertical and spanwise coordinates in each panel are normalized by the boundary layer thickness δ .

simulation can be expressed in terms of the wall, $+$, units using the maximum bed shear stress of the counterpart laminar unperturbed case with the same $Re_\delta = 1478$.

Consequently, the grid size in both uniform streamwise and spanwise periodic directions are $\Delta x^+ = 9.8$ and $\Delta y^+ = 8.4$. Whereas in the non-homogeneous wall-normal direction, the minimum grid spacing is $\Delta z^+ = 0.12$, adjacent to the bed, and the maximum spacing is $\Delta z^+ = 9.0$, located at the mid-vertical height of the domain (equivalent to $z^+ \approx 490$). Furthermore, ten points exists within the viscous sub-layer ($z^+ \leq 5$). The order of the Legendre and Fourier filters is 8 & 10, respectively (see section 3.2.3).

Inserting the optimum noise induces the formation of the elongated streamwise streaks as anticipated. However, without a secondary instability, the energy of those streaks eventually diffuses out after it reach the peak. This response is very similar to the outcome of the quasi-steady transient analysis for a steady base profile. In order to destabilize the formed elongated streaks, a secondary instability is a necessity. Therefore, the next step is to introduce a secondary perturbation into the flow field with elongated streaks. For this case, the adopted secondary perturbation is randomly designed with, however, a wall-normal distribution that is analogous to the distribution of the inner-mode identified for the flat plate boundary layer flow (see Zaki,2013). Additionally, the inserted secondary perturbation is localized in streamwise direction with a periodic distribution in the spanwise direction. The distribution of the secondary instability, at the insertion time, is shown in Fig.4.16. Additionally, the three-dimensional distribution of the secondary noise is represented in Fig. 4.17 in terms of λ_2 iso-contours. As illustrated in Fig.4.16, the amplitude of the sec-

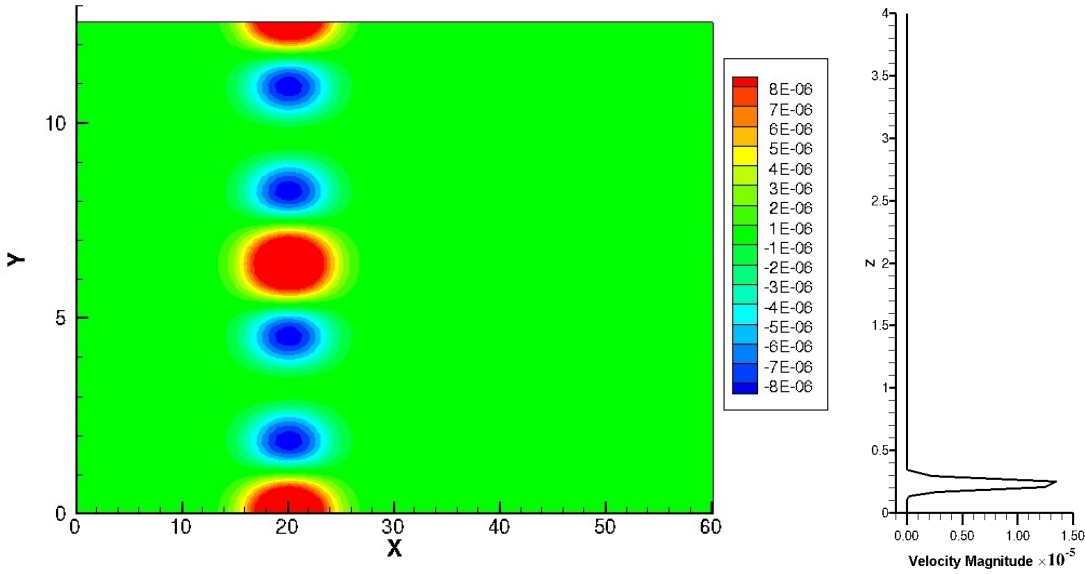


Figure 4.16: Initial distribution of the secondary instability employed in $Re_\delta = 1478$ case. The left panel shows the distribution of the streamwise velocity component of the secondary perturbation on x - y plane located at $z=0.25$. Whereas the vertical distribution of the same quantity at $(X, Y) = (20; 6)$ is shown in the right panel. Coordinates are normalized by the boundary layer thickness δ and velocity amplitude is normalized by the maximum free stream velocity U_{om} .

ondary instability is two orders of magnitude smaller than the primary optimum perturbation inserted at an earlier stage.

In order to compare between the two case, i.e., with and without secondary disturbance, the temporal variation of the energy amplification is presented in Fig.4.18. In this last figure, the energy in both cases is normalized by its initial value which is assumed to be inserted at $t_p = 0$. The point of insertion of the secondary noise is indicated by a dashed vertical line at $t_p \approx 93$ and the wave crest corresponds to $t_p \approx 371$, indicated by a vertical solid black line. It can be observed from thsi figure, that both curve almost collapse for beginning till the

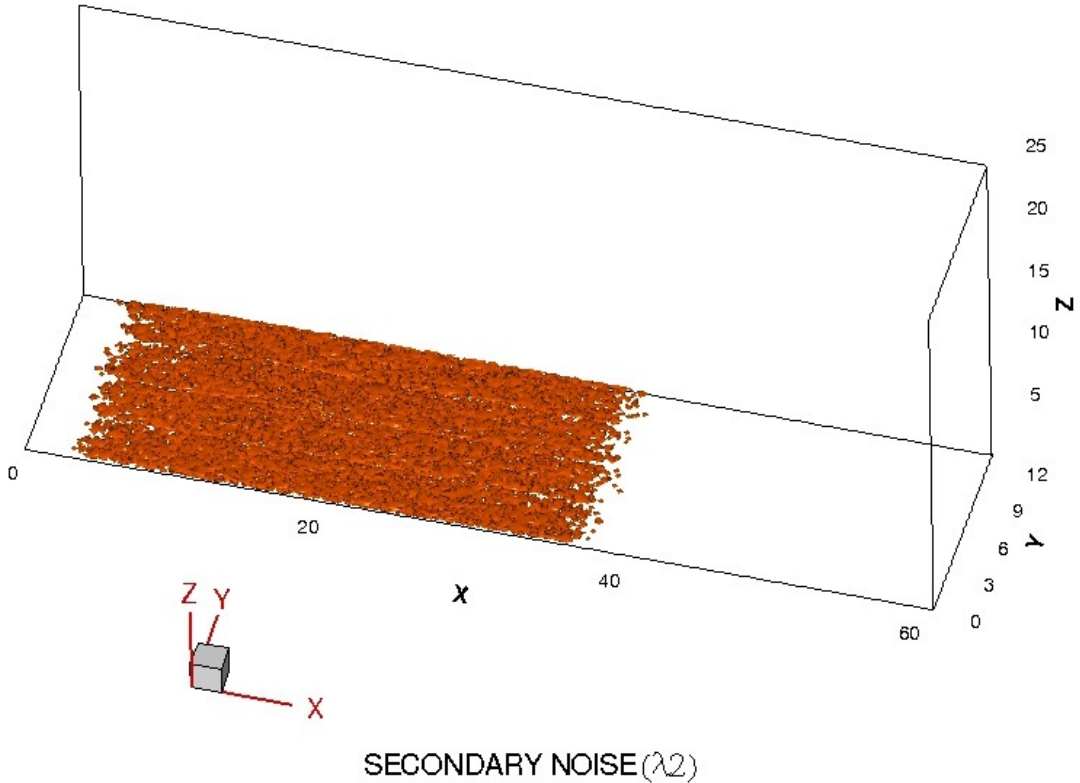


Figure 4.17: Iso-contours of λ_2 of the secondary instability initial distribution employed in $Re_\delta = 1478$ case. Coordinates are normalized by the boundary layer thickness δ .

peak, i.e., $0 \leq t_p < 450$.¹

After the peak, the energy of the simulation with no secondary perturbation starts to decay monotonically similar to the quasi-steady transient analysis of individual profiles. Whereas, the energy of the other simulation starts to increase again at $t_p \approx 475$ suggesting the initiation of the transition. It should be noted here, that the starting time of the second growth, i.e., $t_p \approx 475$, is equivalent to a wave phase $\omega t \approx 7^\circ$ which is earlier than $\omega t_{critical}$ for $Re_\delta = 1478$ case as

¹except the spike which is due some numerical artefact (in the correction process) and doesn't affect the flow as will be shown later.

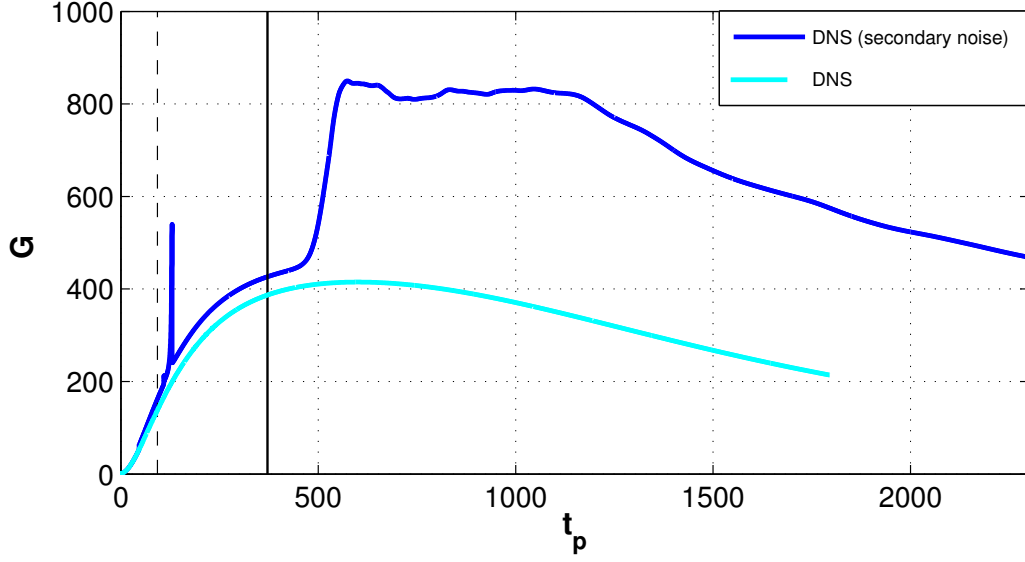


Figure 4.18: Iso-contours of λ_2 of the secondary instability initial distribution employed in $Re_\delta = 1478$ case. Coordinates are normalized by the boundary layer thickness δ .

highlighted in Fig. 4.14.

In order to have a better interpretation of the energy variations, shown in Fig. 4.18, a series of snapshots at different ωt that shows the evolution of λ_2 iso-contours will be shown in Fig. 4.19 for the $Re_\delta = 1478$ case with secondary noise. Fig. 4.19(a) shows the formation of the streamwise elongated streaks. This result is common between the two different simulation set-up, i.e., with and without secondary instability. A snapshot of the λ_2 iso-contours field, just after the insertion of the secondary noise, is shown in 4.19(b). Starting from $\omega t = 0^\circ$, the secondary instability matures to the level that it starts to breakdown the uniform streaks into isolated structures as highlighted in 4.19(c). Afterwards, these isolated structures starts to grow spatially and merges as shown in 4.19(d). This wave phase, i.e., $\omega t = 7^\circ$, corresponds to the start of the second growth of energy stage highlighted earlier in Fig. 4.18. At this point in time, the non-

linearity enhance this growth by transferring energy from large to scale scale events which eventually leads to a chaotic state, as shown in Fig. 4.19(e). The fact that the base flow is evolving continuously and the flow reversal takes place after $\omega t = 30^\circ$, give rise to a larger scale event that starts to steer the chaotic flow with some characteristic streamwise wavelength as shown in Fig. 4.19(e). One can think of this streamwise large event as a residual of K-H billows. However, this last observation needs a more careful deliberation.

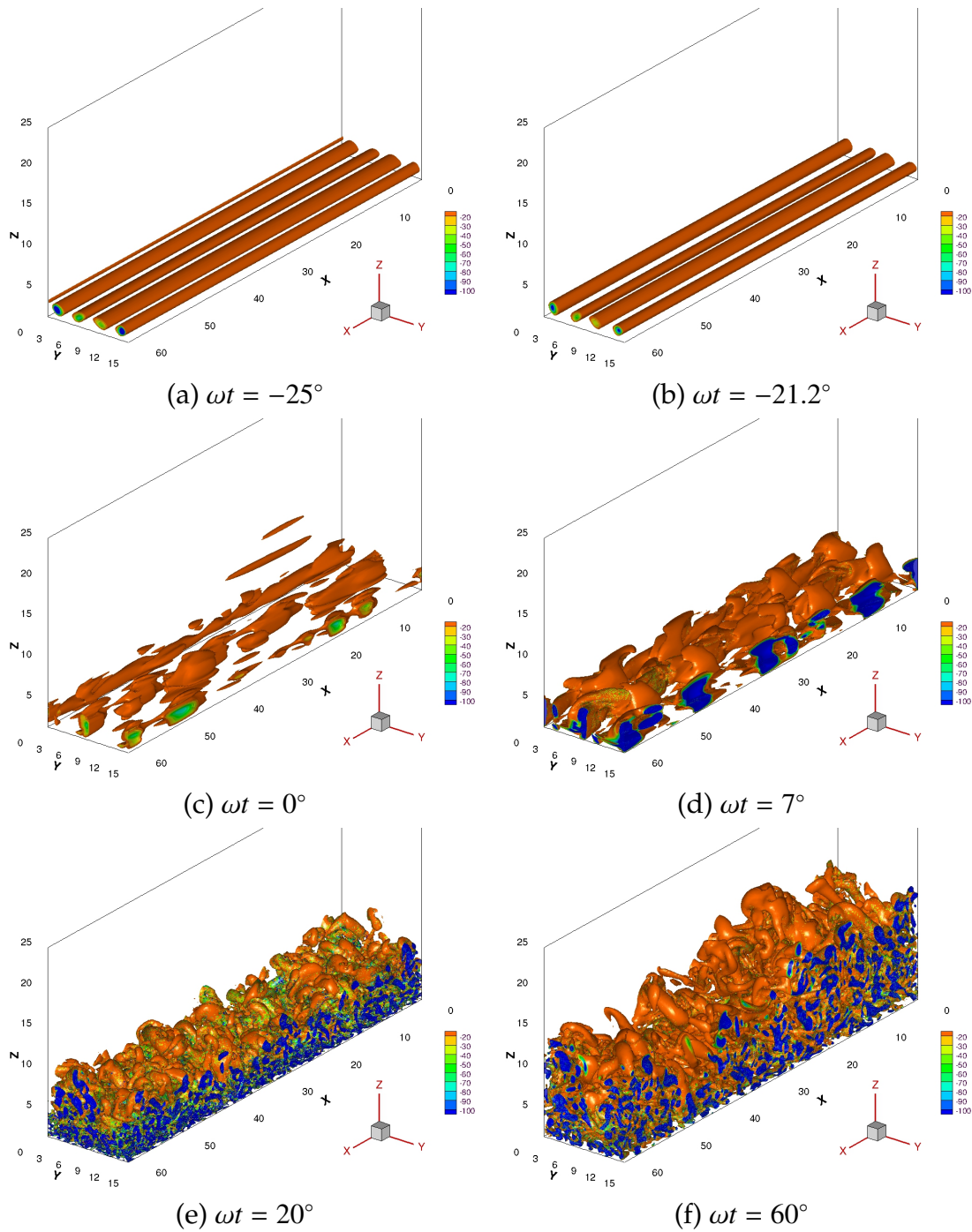


Figure 4.19: Iso-contours of λ_2 for $Re_\delta = 1478$ case at different wave phase (ωt). The horizontal and vertical coordinates in each panel are normalized by the boundary layer thickness δ .

CHAPTER 5

DISCUSSION

5.1 Classical Transition

5.1.1 Mode of instability

As previously discussed, depending on Re_δ , there are two distinct dominant 2D instability modes. The first mode, hereafter regarded as $M1$, is associated with the highest energy growth rate, which consistently takes place after the flow reversal. The wavenumber of this mode is roughly around $\alpha \in [0.47, 0.42]$ which corresponds to a non-dimensional wave length of $\lambda_x \in [13.5, 15]$. Above a certain Re_δ threshold, another mode, hereafter regarded $M2$, is the first to destabilize before the flow reversal and has a wavenumber of roughly $\alpha \approx 0.30$ that corresponds to a non-dimensional wavelength of $\lambda_x \approx 21$. The maximum growth rate of $M2$ is much smaller than the highest energy growth rate associated with $M1$ throughout the BBL evolution. However, as described in 4.1.2 for $Re_\delta > 5000$, $M2$ can grow sufficiently fast such that it prevails over $M1$ as the dominant instability mode.

To further highlight the difference between these two instability modes, the base flow neutral contour curves, i.e., $\omega_i = 0$, are shown in Fig. 5.1 as a function of Re_δ following the calculations of quasi-steady linear stability analysis. In this figure, the locus of centers of the highest growth contour for the different Re_δ is represented as a solid ellipse. For the conditionally unstable regime $450 \lesssim Re_\delta < 1900$, the first destabilized mode is the one with the highest growth

rate and corresponds to $M1$ observed in the two-dimensional DNS (e.g. Fig. 4.8). This numerical observation of $M1$ dominance fits well with the average distance between the successive vortex tubes observed in the SU10 study, i.e., $\lambda_{Sumer} \in [13, 14.5]$, and in previous numerical simulations (e.g. Vittori *et al.*, 2011; Scandura 2013) within this particular Re_δ range. In the first sub-regime of the unconditionally unstable regime, i.e., $1900 < Re_\delta < 5000$, although $M2$ is the first destabilized mode, it does not have enough time to grow to a significant amplitude before the flow reversal and therefore control the formation of the coherent vortex structures. In this Re_δ range, the $M1$ mode, which always has the highest growth rate, is the one that sets the spacing between the vortex tubes formed after the flow reversal. This instability is equivalent to the one reported for the conditionally unstable regime. Consistently with our findings, Ozdemir *et al.* (2013) reported a comparable average distance between the formed vortex tubes, i.e. $\lambda_{Ozdemir} \approx 13.5$ for $Re_\delta = 2000$ and $\lambda_{Ozdemir} \approx 16$ for $Re_\delta = 2500$.

As Re_δ is increased further, the neutral curves start to show a visible protrusion towards a smaller wave-number, that of $M2$. Eventually, this protrusion penetrates into the acceleration phase region. As discussed earlier, for $Re_\delta > 5000$, $M2$ starts to grow at an earlier phase and it can actually overtake the high growth rate of $M1$ that occurs after the flow reversal.

To further illustrate the competition between the two modes, two values of Re_δ , 4000 and 6300, are additionally examined. In Fig. 5.2, the growth contours for $Re_\delta = 4000$ are first plotted. Fig. 5.3 shows the corresponding transient growth rate of G_W for the two modes $M1$ and $M2$. For this latter Re_δ value case, $M2$ has the highest growth rate prior to the flow reversal, i.e., $\omega t < 30$. After the flow reversal takes place, $M1$ dominates, as induced by the increasingly steeper

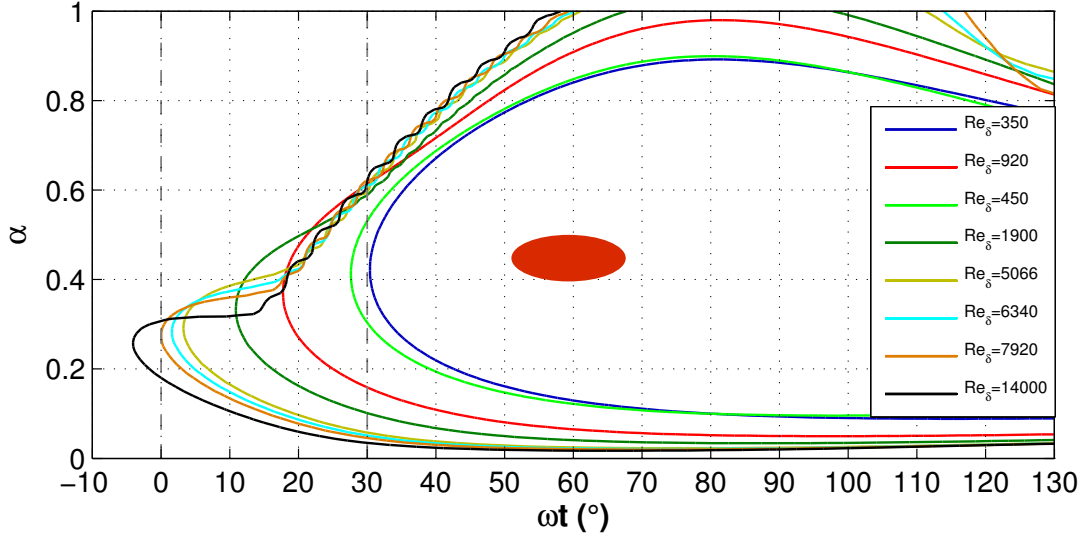


Figure 5.1: Variation of the neutral curves ($\omega_i = 0$) as a function of Re_δ . The solid ellipse represents the locus of centers of the maximum ω_i of the different cases. The two vertical dashed lines correspond to the wave crest (left) and the flow reversal phase (right)

slope, and eventually the generated vortex tubes are spaced in agreement with the quasi-steady instability theory-computed wavelength of $M1$ (i.e., $\lambda_x \approx 15$; see also the left panel of Fig. 5.6 and its discussion).

An additional exercise which further demonstrates the competition between the two instability modes is conducted at $Re_\delta = 6300$ where the perturbation is intentionally inserted at three different wave phases. The growth rate contours of this Re_δ case, obtained from the linear stability analysis, are plotted in Fig. 5.4. Three vertical lines, representing the different insertion phases of perturbation: $\omega t_{ins} = 0^\circ$, 18° and 30° , are also included in this figure.

At the same value of Re_δ , Fig. 5.5 shows the transient variation of G_W for each $M1$ and $M2$ for the three different times of perturbation insertion (i.e., $\omega t_{ins} = 0^\circ$, 18° and 30°) where the initial relative amplitude of the inserted

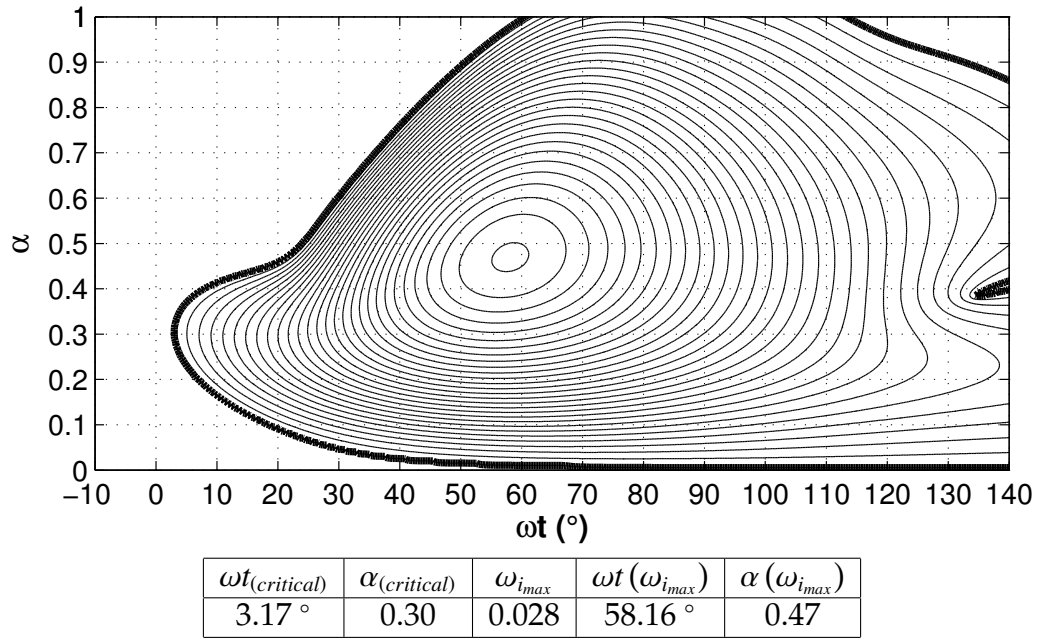


Figure 5.2: Growth contour of $\omega_i > 0$ for $Re_\delta = 4000$ throughout the wave deceleration (thick solid line $\omega_i = 0$, contour value spacing $\Delta\omega_i = 0.001$). Table quantities are as defined in the caption of Fig. 4.1.

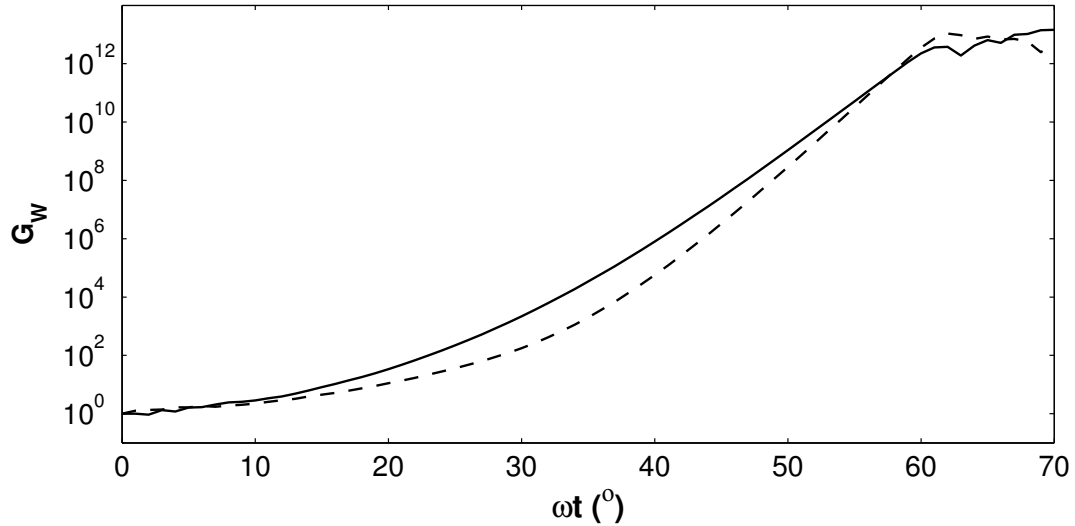


Figure 5.3: Transient growth of G_W for $Re_\delta = 4000$. Dashed lines are for $M1$, i.e., $\lambda_x \approx 15$, whereas solid lines are for $M2$, i.e., $\lambda_x \approx 21$.

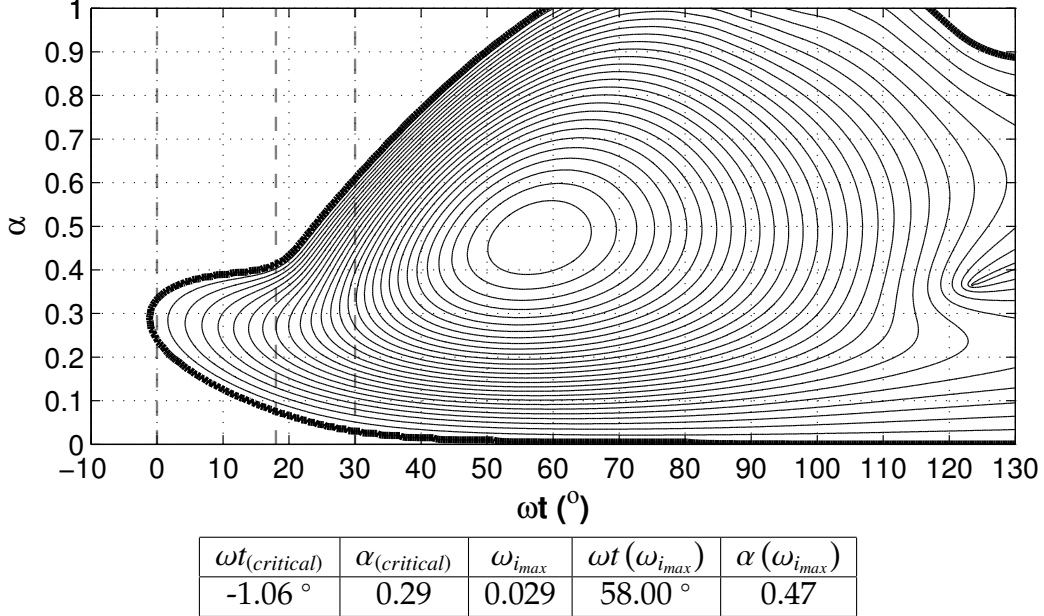


Figure 5.4: Growth contour of $\omega_i > 0$ for $Re_\delta = 6300$ throughout the wave deceleration (thick solid line $\omega_i = 0$, contour value spacing $\Delta\omega_i = 0.001$). The three vertical dash lines mark the different insertion phases. Table quantities are as defined in the caption of Fig. 4.1.

perturbation is $\sim O(10^{-12})$. In the calculation of G_W for the different cases of insertion, the kinetic energy of the vertical velocity component for the particular mode(i.e., $q_W(\omega t)$) is normalized by its initial value at the insertion time $q_W(\omega t_{ins})$. In the left panel of Fig. 5.5, $M2$ starts to grow immediately at $\omega t = 0^\circ$, as the adverse pressure gradient is established, with a relatively high growth rate compared to $M1$. $M1$ picks up around the flow reversal phase , i.e., $\omega t \approx 30^\circ$, but can not overcome the earlier growth of $M2$ (as in the case $Re_\delta = 4000$ Fig. 5.3) provided that the perturbation was inserted prior to flow reversal (i.e., $\omega t \approx 30^\circ$). As the perturbation is inserted closer to the flow reversal phase angle, the most unstable mode changes from $M2$ to $M1$ as shown for the $\omega t_{ins} \approx 30^\circ$ case.

In Fig. 5.6, a comparison between two different Re_δ values, i.e., 4000 (figs.

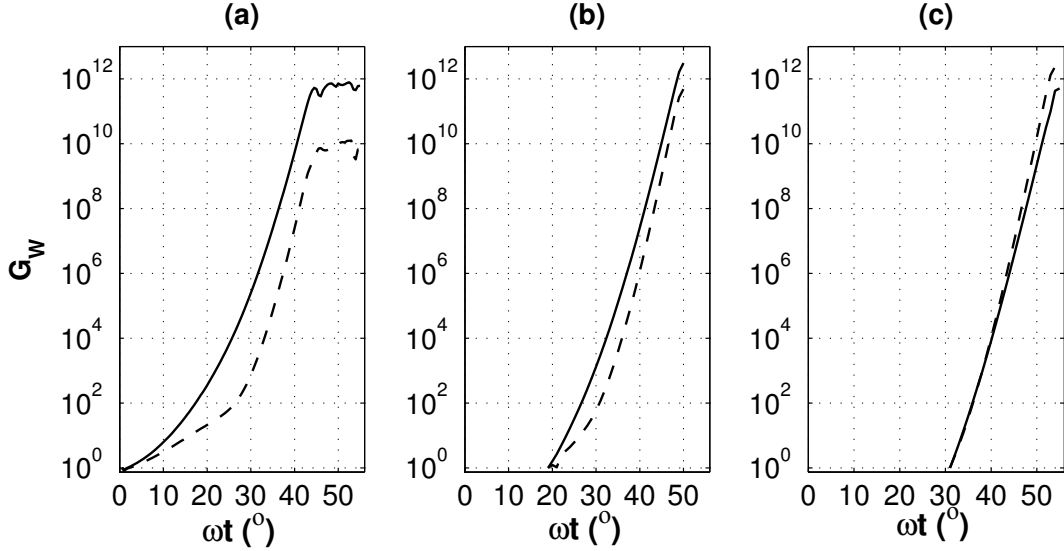


Figure 5.5: Transient growth of G_W for $Re_\delta = 6300$ for three different noise insertion phase cases: $\omega t_{ins} = 0^\circ$ (a), $\omega t_{ins} = 18^\circ$ (b) and $\omega t_{ins} = 30^\circ$ (c). $M1$ is represented by the dashed line whereas solid lines correspond to $M2$.

5.6(a) – (c)) and 8000 (figs. 5.6(d) – (f)), in terms of the spatial structure of instability modes throughout the different development phases of the perturbation, are shown. Stream-depth slices of the perturbation vorticity contour, computed from both linear stability analysis (Figs. 5.6(a) and (d)) and DNS (Figs. 5.6(b), (c), (e) and (f)), are used to highlight the difference between those two Re_δ cases. In each of these contour plots, the vorticity field is normalized by the local maximum at the corresponding phase. Figs (5.6(a) and (d)) represent the vorticity field of the most unstable mode, at the indicated phases, estimated from the linear stability analysis.

The first two rows of Fig. 5.6 indicate a very good agreement between the linear stability analysis and the DNS results in terms of the structure of the perturbation vorticity field. From these first two rows, two shear layers exist on top of each other. The upper layer is similar to the classical $tanh$ -profile shear layer

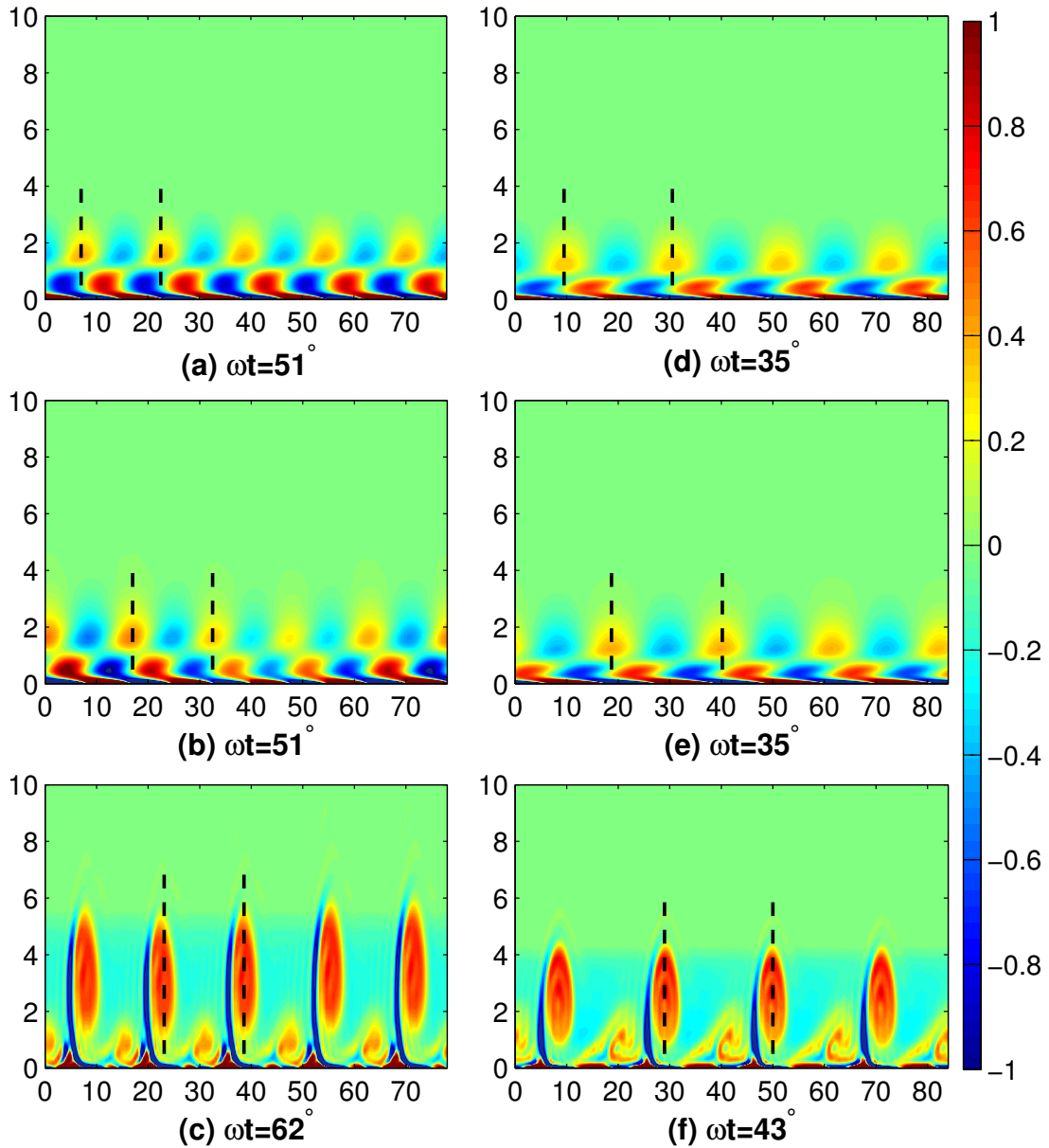


Figure 5.6: Visualization of the perturbation vorticity field (normalized by the corresponding maximum value) for $Re_\delta = 4000$ (Figs. 5.6(a) – (c)) and $Re_\delta = 8000$ (Figs. 5.6(d) – (f)) at different wave phase ωt . First row: linear stability analysis. Second and third rows: DNS results. In the DNS results, only a portion of the computational domain is shown. In the left column $M1$ is the dominant instability mode. In the right column $M2$ dominates. The horizontal and vertical coordinates in each panel are normalized by the boundary layer thickness δ .

whereas the lower one is induced by the no-slip constraint at the wall. As Re_δ increases, the lower layer shape is much sharper, i.e., sheared, and compacted vertically as the perturbation starts to evolve at earlier times. At a later stage of the perturbation evolution, the spacing between the formed vortex tubes is set by the dominant instability as mentioned earlier. $M1$ dominates for $Re_\delta = 4000$ whereas $M2$ is the dominant mode for $Re_\delta = 8000$. The difference in spacing between the resulting vortex tubes can be observed in the two plots of the last row, i.e., Figs 5.6(c) and 5.6(f) where the diameter of the vortex tubes is directly proportional to the thickness of the base flow shear layer at the rolling up phase of the vortices. Hence, for lower Re_δ and late emergence phase, the diameter of the vortex tubes is larger than at higher Re_δ case.

5.1.2 Similarity with instability properties of other wave-driven transient flows

The Re_δ limit below which quasi-steady instability analysis is not applicable may be generalized to different wave-induced flows. In particular, this generalization may be made for flows driven by internal waves, albeit controlled by a different governing parameter. In this regard, both Troy & Koseff (2005) and Barad & Fringer (2010) reported an instability criterion based on the non-dimensional average perturbation growth rate for progressive internal gravity waves and for internal solitary waves respectively. In both cases, the particular instability criterion is satisfied when $\bar{\sigma}_i T_w > 5$, where $\bar{\sigma}_i$ is the growth rate of the instabilities averaged over a time interval T_w during which a parcel of fluid within stratified water is subjected to a wave-driven background verti-

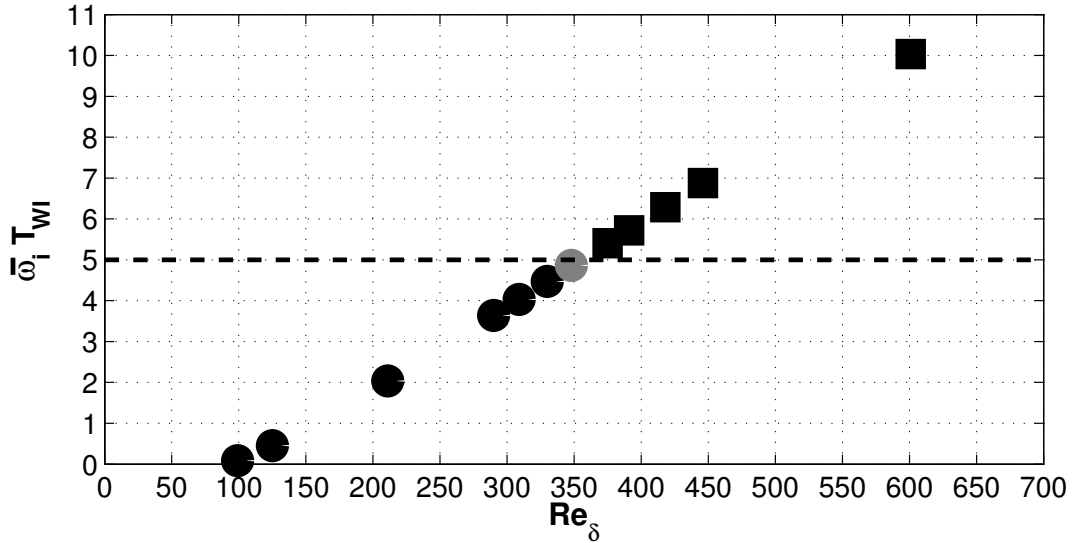


Figure 5.7: Non-dimensional average growth rate variation as a function of Re_δ . Stable, ●; Unstable, ■. Horizontal dash line represents the applicability limit of the quasi-steady linear stability analysis.

cal shear corresponding to Richardson number (see Thorpe 2005 for definition) less than 1/4 and the base flow was assumed to be parallel as in the current study. For the problem at hand, a similar non-dimensional average growth rate $\bar{\omega}_i T_{WI}$ may be calculated where $\bar{\omega}_i$ is average positive growth of the critical wave number, i.e., $\alpha_{(critical)}$, found to always lies within the highest growth rate modes interval (section 4.1.1). Whereas the time scale T_{WI} is defined as the period in which the perturbation growth is positive (i.e., $\omega_i > 0$). The variation of this non-dimensional average growth rate $\bar{\omega}_i T_{WI}$ as function of Re_δ is presented in Fig.5.7. Although the underlying base flows are quite different (instability of a surface wave's BBL vs. instability of internal waves in mid-water), the $Re_\delta = 350$ limit of applicability of the quasi-steady linear stability analysis defined in this study occurs at a value of $\bar{\omega}_i T_{WI}$ remarkably close to that computed by the two studies mentioned above, i.e., Troy & Koseff (2005) and Barad & Fringer (2010).

This agreement between the three different studies suggest that the particular instability criterion may be universal for a wider range of transient base flows.

5.1.3 Breakdown of the two-dimensional coherent structure

The last component related to the classical transition study is the breakdown of the developed two-dimensional coherent structures into a chaotic state. This breakdown is attributed to the manifestation of a secondary spanwise disturbance. In order to simulate this transition process, a fully three-dimensional simulation is required. In this simulation, a secondary random spanwise perturbation is inserted in addition to the streamwise noise. A representative example for this scenario is shown in 4.1.3 for $Re_\delta = 1833$ case. Even though the flow has not developed into a fully turbulent state for $Re_\delta = 1833$ case, the breakdown process of the vortex tubes is indicative and it follows two combined pathways to transition.

The first pathway involves the formation of vortex filaments, i.e., rib vortices, that tangle around the developed spanwise vortex tubes. this scenario is similar to that in free shear mixing layer (e.g. Rogers & Moser, 1992 and 1994). Alternatively, the second pathway is limited to some of these vortex filament have a hairpin vortex-like structure which has some similarity with the zero-pressure gradient flat-plate boundary layer transition (e.g. Head & Bandyopadhyay, 1981; Zhou *et al.*, 1999). In our opinion, the hairpin vortex-like structure shape results from the interaction between the developed vortex tubes and the bottom wall. A sample of this hairpin vortex-like structure is shown in Fig. 5.8 for the

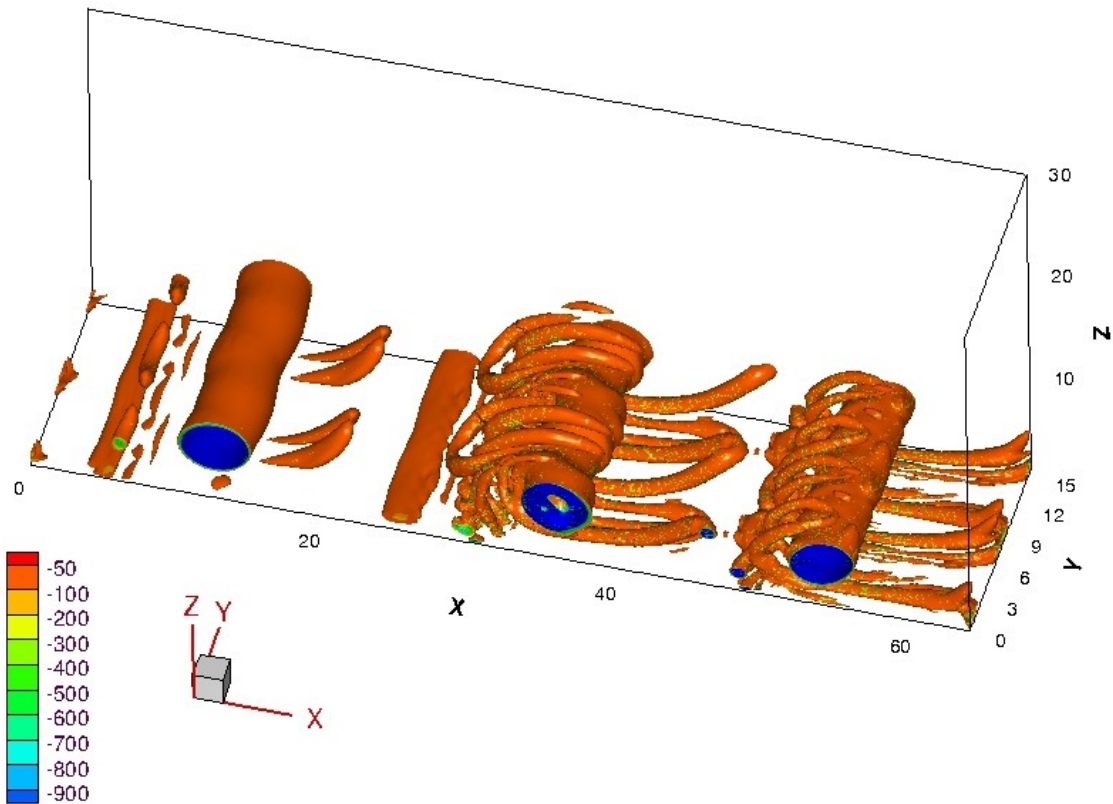


Figure 5.8: Iso-contours of λ_2 with hairpin vortex-like structures for $Re_\delta = 1833$ case at wave phase $\omega t = 75.5^\circ$. The horizontal and vertical coordinates in each panel are normalized by the boundary layer thickness δ .

Ozdemir *et al.* (2013) reported that these two transition paths can take place but however separately. The flat-plate like transition is only reported for a limited range ($1500 < Re_\delta < 2000$), whereas the free-shear layer like transition is dominant for $Re_\delta > 2000$. In their result section, they showed the formation of the hairpin-like structures for $Re_\delta = 2000$ case where the amplitude of the initial inserted perturbation noise is 20% of the maximum free stream velocity. This high initial perturbation amplitude, inserted into the initially quiescent flow field, can induce some non-linear effect close to the bottom bed. This non-linear secondary effect may explain the formation of the hairpin-like vortex structures

separately from the main vortex tubes. Further work is needed to verify this conjecture.

5.2 Bypass Transition

5.2.1 Maximum amplification modes

At this point, it has been proven that the largest transient growth takes place for perturbations, i.e., modes, with no streamwise dependence, i.e., $\alpha = 0$. As manifested in section 4.2.1, specially in Figs. (4.11 - 4.12), the modes with the higher transient growth are characterized by a streamwise wave number $\alpha = 0$ and spanwise wave number β ranging from 0.7 to 1.0 for the different successive ωt -profiles. Despite this variation in β of the highest growing mode, summarized in Fig. 4.12, modes identified by $\alpha = 0$ and $\beta \in [0.7, 1.0]$ have a comparable high growth rate for a specific ωt -profile. This persistent of the most critical $(\alpha; \beta)$ combination may hint a possible cumulative growth effect for the temporally varying base flow as shown for the classical modal analysis. To further demonstrate this last remark, the different modes energy growth curves for the particular $\omega t = -10^\circ$ base profile are shown in Fig. 5.9 as a sample case. As illustrated in this figure, the variation, in terms of maximum growth amplification, among the different β is less than 5%. This finding along with the observations from Fig. 4.11; lead to the conclusion that the maximum amplification is always encountered for modes characterized by $\alpha = 0$ and any $\beta \in [0.7; 1.0]$ regardless of the different ωt .

The next step is to explore the relation between the maximum amplification,

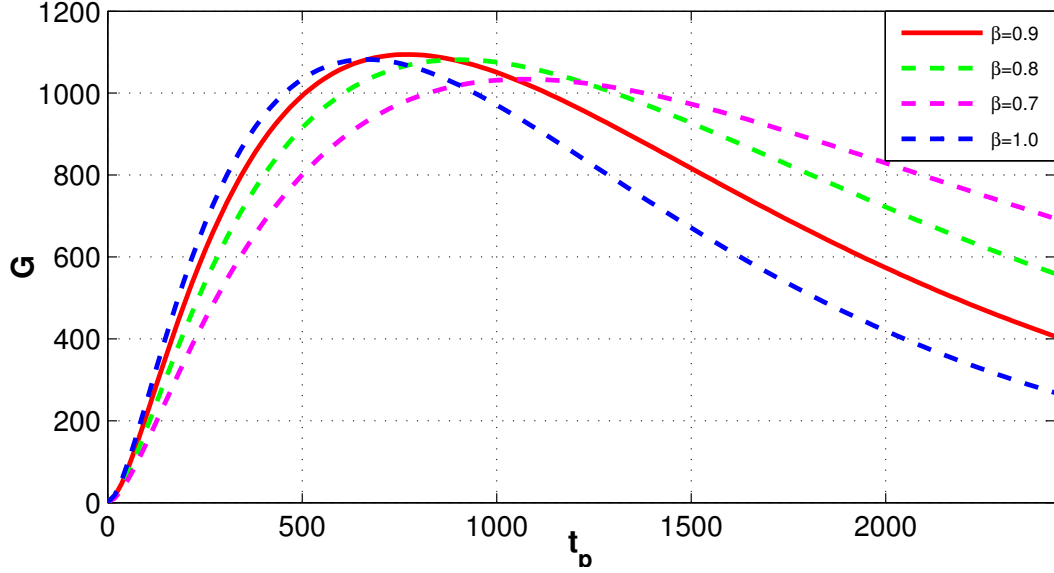


Figure 5.9: Temporal variation of the amplification function $G(t_p)$ of four different modes with no streamwise dependence $\alpha = 0$ and the different β are shown in the figure legend. The base flow profile corresponds to the wave phase $\omega t = -10^\circ$ of $Re_\delta = 1478$ case. The solid red line corresponds to the critical $(\alpha; \beta)$ combination.

i.e., G_{max} and the base flow Re_δ for the different ωt -profiles. For a single ωt -profile, distinguished by the same colour, the calculated G_{max} for the 4 modes $(\alpha; \beta) = (0; 0.7 : 1.0)$ are plotted against Re_δ in Fig. 5.10. As discussed earlier, Fig. 5.10 emphasises the fact that the maximum amplification slightly varies among the modes characterized by $\alpha = 0$ and $\beta \in [0.7; 1.0]$ at a given Re_δ . The curve that best fit the scatter data of G_{max} versus Re_δ , i.e., the dashed lines in Fig. 5.10, satisfies $G \propto Re_\delta^2$ relation. This relation agree with what is reported by Trefethen *et al.* (1993).

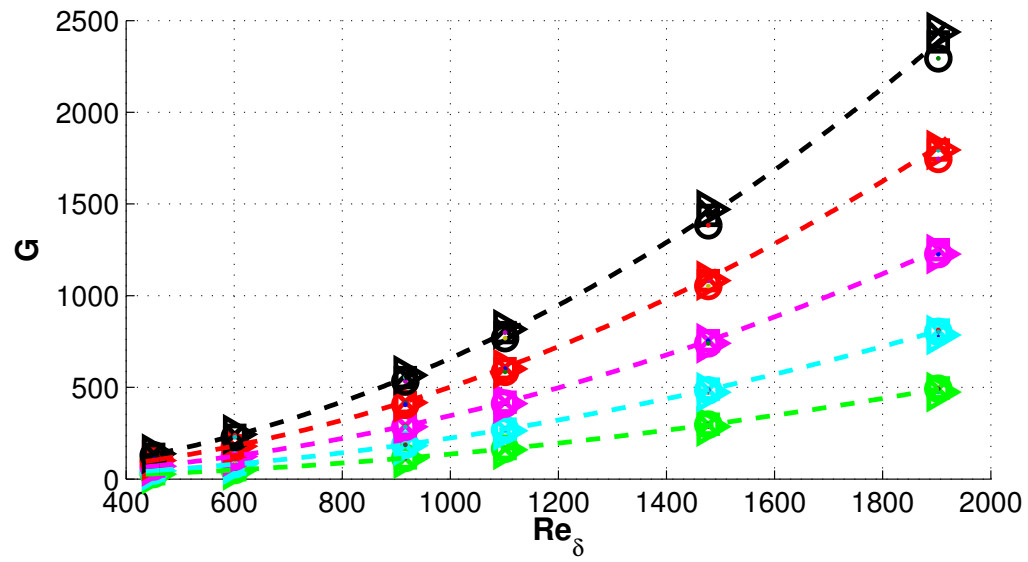


Figure 5.10: Max. growth amplification as a function of Re_δ . Different colours refer to different base flow ω_t : -40° ; -30° ; -20° ; -10° & 0° . Symbols corresponds to modes with $\alpha = 0$ & different β : 0.7 (\blacksquare); 0.8 (\triangleright); 0.9 (\circ) & 1.0(\times). Fitting dashed lines comply with $G \propto Re_\delta^2$ relation.

CHAPTER 6

CONCLUSION AND FUTURE WORK

In this study, the two possible mechanisms of transition to turbulence, i.e., classical and bypass transitions, are investigated for the bottom boundary layer (BBL) under a solitary wave. The BBL under solitary wave was approximated by a flow in an oscillating water tunnel driven by a soliton-like wave induced pressure gradient similar to Sumer *et al.*, 2010(referred to as SU10). Such an investigation is founded on a carefully designed linear stability analysis complemented by a fully non-linear two- and three-dimensional simulations, using high-order accuracy numerical methods, for the temporally varying base flow. The classical transition consists of the breakdown of the developed two-dimensional coherent structure, i.e., vortex tubes, triggered by a secondary spanwise disturbance. Alternatively, an earlier transition, i.e., prior to the formation of the vortex tubes, can take place in the form of isolated patches/spots of turbulence that expand spatially leading eventually to a full turbulent transition. Those spots are the manifestation of an optimum initial disturbance with no streamwise dependence, i.e., $\alpha = 0$. Additional work is needed, however, to extrapolate the findings of this study to the actual physical tsunami event.

6.1 Classical transition

This part of the study focused on the two-dimensional investigation of the asymptotic stability, leading to the classical transition, of the BBL flow under solitary waves using both linear and non-linear approaches. A temporal instability map of the bottom boundary layer (BBL) under a solitary wave has been constructed. In this map, the connections between experimental observations,

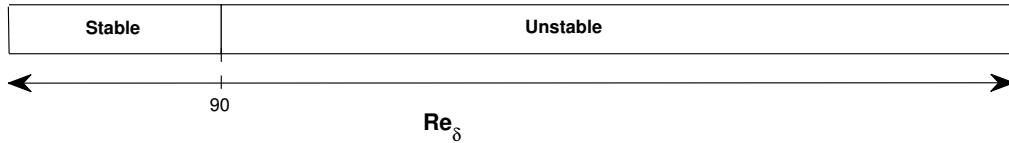
classical stability analysis and fully non-linear numerical simulations have been established. Both quasi-steady/transient linear stability analysis and fully non-linear two- and three-dimensional simulations are carried out using high-order accuracy numerical methods.

The quasi-steady linear stability analysis has been employed to give an insight into the growth rate of the individual modes for each velocity profile according to a “momentary” criterion of instability as proposed Blondeaux *et al.* (2012). The Re_δ threshold above which the quasi-steady assumption holds is when the perturbation recovers its initial amplitude within the wave event. To formally identify this threshold, a transient linear stability analysis approach is adopted, which is also verified using fully non-linear direct numerical simulations (DNS). This lower Re_δ limit corresponds to the case where the base flow is first destabilized before the flow reversal takes place.

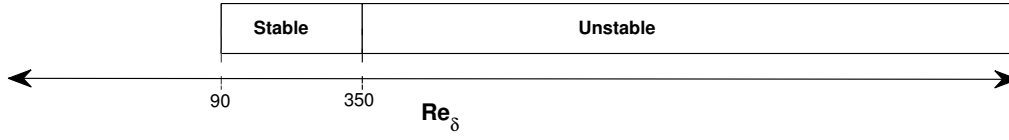
The average perturbation growth rate corresponding to the above applicability threshold is then compared to the average growth rate associated with a similar instability criterion reported in the literature, albeit for different base flows, i.e., those driven in mid-water for progressive and solitary internal waves (Troy & Koseff, 2005; Barad & Fringer, 2010). Good agreement is found across all studies considered which suggests a possible universality of the particular instability criterion for a wider range of transient base flows.

After identifying the lower Re_δ limit of applicability of quasi-steady linear stability analysis, two-dimensional fully non-linear DNS have been used to classify the base flow into three possible regimes: unconditionally stable or laminar, conditionally unstable and unconditionally unstable. Crucial to this classification, is an alternative definition of “stability” which does not rely on pertur-

Quasi-steady Asymptotic Analysis



Transient Linear Stability Analysis



Fully Non-Linear Analysis

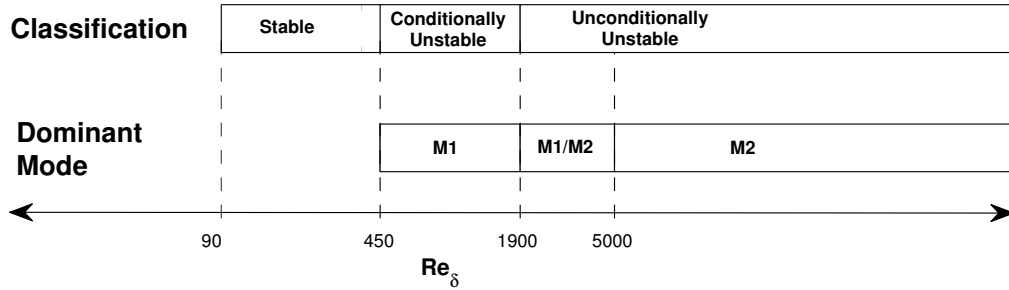


Figure 6.1: Instability map of the BBL flow under solitary waves. The flow is classified in accordance to four criteria: quasi-steady steady linear stability analysis (upper bar), transient linear stability analysis (second bar from top), appearance of the vortex tubes (third from top) and dominant mode of instability (bottom bar).

bation growth rates. Instead, it is more qualitatively/visually-based according the laboratory observations of (SU10). The map of instability illustrating the possible classifications of the base flow is shown in Fig. 6.1.

What is regarded as “stability” in the alternative, more visually-oriented, flow classification approach is the ability of the perturbation to sufficiently grow in amplitude such that it can alter the base flow. In other words, the perturbation amplitude will be amplified, through linear instability, to the same order of magnitude of the base flow within the time scale of the wave. Vortex tubes then emerge as a result of the non-linear interaction of this amplified most unstable

mode with the base flow. The critical Re_δ for the appearance of the vortex tubes, i.e., lower limit of the conditionally unstable regime, is investigated in more detail and the discrepancy with the experimental proposed limit is discussed. For a specific Re_δ case in the conditionally unstable regime, a very good agreement was found between numerical simulations and the SU10 measurements in terms of the bed shear stress and the characteristics, i.e., spacing and time of formation, of the formed vortex tubes. This lower limit of the unconditionally unstable regime is found to match the Re_δ limit for the transition to turbulence identified by Ozdemir *et al.* (2013).

The variation of the shape of the neutral curves with increasing Re_δ is also addressed in this study. An immediate consequence of such a variation is the existence of two primary modes of instability: post- ($M1$) and pre-($M2$) flow reversal modes. The dominance of either of these modes and is reflected in the resulting streamwise spacing between the generated vortex tubes. The post flow reversal mode, which is related to the instability of the developed shear layer, is characterized by the highest growth rate and dominates for relatively low Re_δ flows , i.e in the conditionally unstable regime. As the Re_δ is increased and the flow enters the second sub-regime of the unconditionally unstable regime, the $M2$ mode, which is longer in wavelength, destabilizes first and can grow sufficiently fast to dominate, leading to another type of instability different than the traditional shear layer instability. As Re_δ is increased further, $M2$ establishes a distinct signature within the the neutral curve which starts to protrude into the acceleration phase. No inflection point exists within the base flow velocity profiles during this stage in flow evolution, which suggests a viscous origin of the instability linked to $M2$.

At the lower end of the Re_δ range where $M2$ is dominant when low initial amplitude perturbation perturbations are inserted at $\omega t = 0^\circ$, a competition between the two modes takes place if one pushes further in time the above time of perturbation injection. If perturbation insertion is sufficiently delayed, the high growth of $M1$ can overcome the early destabilization of $M2$ and it is what sets the spacing between the generated vortex tubes. Effectively, another layer of base flow classification is therefore introduced, as shown in Fig. 6.1. For sufficiently high Re_δ , $M2$ always dominates regardless of perturbation insertion time. Finally, for the unconditionally unstable regime, increase of the amplitude of the insertion perturbation can lead to a non-linear transition to turbulence well before the flow reversal.

The previously proposed, experimentally-based, classification of the base flow as function of its Reynolds number has been revisited in a more detailed manner combined with an extension to larger values of this governing parameter. Another aim of this study is to focus on establishing a connection between the linear/non- linear analysis and the experimental observation from the point of view of the classical transition (two to three-dimensional) transition to turbulence, as observed in most free shear flows (Drazin, 2004). Finally, a complete classical transition case is presented in which the developed two-dimensional coherent structures breaks down into chaotic state due to a spanwise secondary instability.

6.2 Bypass transition

The second part of this study, focused on the three-dimensional investigation of the short-term transient energy growth for the BBL flow under solitary waves using both linear and non-linear approaches. This high initial growth can lead to the formation of elongated streamwise streaks. These streaks, after being subjected to a secondary instability, develop into isolated patches of turbulence; "turbulent spot". Upon formation, these spatially distinct spots keep expanding spatially and finally merge into a single energetic patch/region. This scenario, referred to as bypass transition, takes place prior to the formation of coherent structures and leads to an early transition to turbulence. Both linear stability analysis and DNS are employed to investigate such a transition scenario. The linear stability analysis is, however, reformulated in the non-modal frame where the three-dimensional aspect of the base flow perturbation is considered.

Similarly to the previously discussed modal analysis, a quasi-steady linear transient stability analysis is performed for the individual velocity profiles for different Re_δ . This non-modal analysis has revealed two main outcomes:

- The critical $(\alpha; \beta)$ combination leading to maximum energy amplification, where α and β are the stream- and spanwise perturbation wave numbers.
- The optimum spatial distribution of the initial perturbation that induces the maximum transient energy amplification associated with the critical $(\alpha; \beta)$ combination.

This analysis reveals that the largest transient growth is achieved for perturbation with no streamwise dependence, i.e., $\alpha = 0$. This agrees well with

what has been reported for similar physical flows (e.g., Poiseuille flow, etc.). In terms of β , the maximum amplification always takes place for $\beta \in [0.7, 1.0]$ range for all velocity profiles. Furthermore, the amplitude of the maximum amplification slightly varies for β within this narrow range, i.e., $\beta \in [0.7, 1.0]$. This self-similarity of the critical $(\alpha; \beta)$ combination suggests a cumulative growth for the temporally evolving base flow. It is worth mentioning here that this finding agrees with the characteristics of the streaks observed in SU10 experiments for the same base flow. In addition to all of the above, a correlation between the amplitude of the maximum amplification and the base flow Re_δ is established for the flow of interest. It is found that the amplitude of the maximum amplification is proportional to the square of the base flow Re_δ .

Afterwards, fully three-dimensional DNS is carried out aiming to reproduce the turbulent spots. The base flow in those simulations is perturbed using the optimum initial disturbance identified from the quasi-steady non-modal analysis. In the DNS simulations, two approaches are followed. The first approach consists of perturbing the base flow using the optimum initial disturbance that corresponds to a base profile in the wave acceleration phase where the base flow is deemed asymptotically stable. This first approach simulates the formation of the streaks successfully and the energy growth calculated from the DNS is comparable with the one estimated from the quasi-analysis for the specific profile. However, the energy decays monotonically after reaching its peak value and the streaks diffuse over time similar to transient analysis outcomes.

Alternatively, in order to reproduce the turbulent spots and, mainly, the bypass transition, a second approach is followed. In such an approach, a secondary instability is inserted after the streak formation similarly to the flat plate

boundary layer (e.g. Zaki, 2013). The results for this second approach is shown for a representative $Re_\delta = 1478$ case where the base flow experiences transition to turbulence before the critical wave phase, $\omega t_{(critical)}$, determined from the asymptotic analysis.

6.3 Future work

Future work will focus on two main directions. The first one concerns the extension of this study towards answering and clarifying some open questions related the BBL flow transition under surface solitary wave. The second aspect, which is a topic of longer-term study, is the implication of the developed instability, and eventually transition to fully turbulent BL, for the near-bed sediment suspension and morphology (e.g. Chou & Fringer, 2010). Also, the similarities between the results of this study and the near-bed instability under the internal solitary wave of elevation [72, 73], the internal analogue of a surface solitary wave, can be an additional area of future investigation.

Focusing on physics of BBL transition, with regards to classical transition, a possible correlation between the wavelength of the coherent structure, linked to the dominant mode of either $M1$ or $M2$, and the resulting streamwise turbulence length scales is worth investigating. In terms of the bypass transition and spot formation, a numerous potential aspects need to be explored in greater details. A short list of those possible aspects is given hereafter:

- Simulate the formation of initially isolated streaky patches by localizing the optimum initial disturbance within the computational domain. This replicates the actual bypass transition scenario.

- Try to identify an accurate optimum initial perturbation distribution for the temporally evolving base flow rather than using the outcome of the quasi-steady transient analysis for an individual profile as an approximation. A suitable approach would consist of solving the adjoint equations for the system¹(see Luchini & Bottaro, 2014 for more details).
- Identify the distribution of the optimum secondary instability of the streaks for the base flow under consideration.

¹The adjoint formulation is useful when one is seeking to obtain one or a few outputs of a system for a wide range of possible inputs.

APPENDIX A
**ANALYTICAL SOLUTION FOR VISCOUS BOUNDARY LAYER FLOWS
 UNDER WEAKLY NONLINEAR TRANSIENT WAVE**

This section summarizes the analytical solution of Liu & Orfilla (2004) for the viscous boundary layer flow under weakly nonlinear transient wave at a fixed location, i.e., $x = 0$. They showed that the rotational component of the boundary layer velocity can be written, in the dimension form, as follows

$$u^*(z^*, t^*) = -\frac{z^*}{\sqrt{4\pi}} \int_0^{t^*} \frac{u_w^*(\tau)}{\sqrt{(t^* - \tau)^3}} \exp\left[\frac{-z^{*2}}{4\nu^*(t^* - \tau)}\right] d\tau, \quad (\text{A.1})$$

where u_w^* denotes the free-stream velocity at the outer edge of the boundary layer (in this study, $u_w^*(t)$ is simply $U_0^*(t^*)$ in 2.1), z^* is the vertical coordinate normal to the bed pointing upward and ν^* is the fluid kinematic viscosity. The corresponding laminar bed shear stress, τ_b^* , can be calculated as follows

$$\frac{\tau_b^*(t^*)}{\rho} = \sqrt{\frac{\nu^*}{\pi}} \int_0^{t^*} \frac{\partial u_w^*(\tau)/\partial \tau}{\sqrt{(t^* - \tau)^3}} d\tau, \quad (\text{A.2})$$

where ρ is the fluid density.

APPENDIX B

PERTURBATION KINETIC ENERGY AND NORMS

As elaborated upon earlier in 2.3.3, the non-modal analysis is founded on the non-orthogonality of the eigenfunction for the linear operator. An appropriate inner product, used to compute the angle between the eigenfunctions, provides a norm to measure the size of the variable vector, i.e., velocity perturbation variation. For the temporal evolution of disturbances in incompressible shear flow, the perturbation kinetic energy is deemed a reasonable choice (Schmid & Henningson, 2001; Schmid (2007). Therefore, in this appendix, the relation between the perturbation kinetic energy and the chosen variables, which fully describe the flow field, the wall-normal velocity and vorticity, is highlighted for the sake of completeness (For more details, see Schmid & Henningson, 2001).

The kinetic energy E of a disturbance described by the state vector q , defined earlier in Eq. (2.33) as

$$q = \begin{bmatrix} \hat{w} \\ \hat{\eta} \end{bmatrix}. \quad (\text{B.1})$$

can be written in terms of the Fourier coefficients of the disturbance variables as follows (Gustavsson, 1986)

$$E = \int_{\alpha} \int_{\beta} E_d d\alpha d\beta \quad (\text{B.2})$$

$$= \int_{\alpha} \int_{\beta} \frac{1}{k^2} \int_{z_1}^{z_2} [|D_z \hat{w}|^2 + k^2 |\hat{w}|^2 + |\hat{\eta}|^2] dz \quad (\text{B.3})$$

where E_d is the energy density in Fourier space. This energy density can be related to the weighted inner product of the state vector as follows

$$E_d = \frac{1}{k^2} \int_{z_1}^{z_2} \left[\begin{pmatrix} \hat{w} \\ \hat{\eta} \end{pmatrix}^H \begin{pmatrix} k^2 - D_z^2 & 0 \\ 0 & 1 \end{pmatrix} \begin{pmatrix} \hat{w} \\ \hat{\eta} \end{pmatrix} \right] dz \quad (\text{B.4})$$

$$= \frac{1}{k^2} \int_{z_1}^{z_2} q^H M q dz = \|q\|^2, \quad (\text{B.5})$$

where M is the positive definite weight matrix defined earlier in Eq. 2.35 as follows

$$M = \begin{bmatrix} D_z^2 - k^2 & 0 \\ 0 & 1 \end{bmatrix}. \quad (\text{B.6})$$

It is more convenient to work with the standard L_2 -norm instead of the weight matrices based norm. Therefore, the matrix M is decomposed, following Cholesky decomposition, into $M = F^H F$. Consequently, Eq. B.5 can be written as follows

$$\|q\|^2 = \frac{1}{k^2} \int_{z_1}^{z_2} q^H F^H F q dz = \frac{1}{k^2} \int_{z_1}^{z_2} (qF)^H F q dz. \quad (\text{B.7})$$

Consequently, the maximum amplification factor $G(t)$ (see Eq. 2.38) can be written as

$$G(t) = \max_{q_0} \frac{\|q(t)\|^2}{\|q_0\|^2} = \max_{q_0} \frac{\|Fq(t)\|^2}{\|Fq_0\|^2} = \max_{q_0} \frac{\|F \exp(\hat{L} t) q_0\|^2}{\|Fq_0\|^2} \quad (\text{B.8})$$

$$= \max_{q_0} \frac{\|F \exp(\hat{L} t) F^{-1} F q_0\|^2}{\|Fq_0\|^2} = \|F \exp(\hat{L} t) F^{-1}\|^2. \quad (\text{B.9})$$

Defining the linear operator L , mentioned in 2.3.3, as $L = F \hat{L} F^{-1}$. Consequently, the L_2 -norm and the L_2 inner product can be used conveniently and the maximum amplification $G(t)$ can be written as in Eq. (2.39) in

$$G(t) = \|\exp(L t)\|^2. \quad (\text{B.10})$$

BIBLIOGRAPHY

- [1] P. Andersson, M. Berggren, and D. S. Henningson. Optimal disturbances and bypass transition in boundary layers. *Physics of Fluids (1994-present)*, 11(1):134–150, 1999.
- [2] M. F. Barad and O. B. Fringer. Simulations of shear instabilities in interfacial gravity waves. *J. Fluid Mech.*, 644:61–95, 2010.
- [3] P. J. Blennerhassett and A. P. Bassom. The linear stability of flat stokes layers. *J. Fluid Mech.*, 464:393–410, 2002.
- [4] P. Blondeaux, J. Pralits, and G. Vittori. Transition to turbulence at the bottom of a solitary wave. *J. Fluid Mech.*, 709:396–407, 2012.
- [5] J. P. Boyd. Two comments on filtering (artificial viscosity) for Chebyshev and Legendre spectral and spectral element methods: Preserving boundary conditions and interpretation of the filter as a diffusion. 143:283–288, 1998.
- [6] J. P. Boyd. *Chebyshev and Fourier spectral methods*. Courier Dover Publications, 2013.
- [7] K. M. Butler and B. F. Farrell. Three-dimensional optimal perturbations in viscous shear flow. *Physics of Fluids A: Fluid Dynamics (1989-1993)*, 4(8):1637–1650, 1992.
- [8] S. Carstensen, B. M. Sumer, and J. Fredsøe. Coherent structures in wave boundary layers. part 1. oscillatory motion. *J. Fluid Mech.*, 646:169–206, 2010.
- [9] S. Carstensen, B. M. Sumer, and J. Fredsøe. A note on turbulent spots over a rough bed in wave boundary layers. *Physics of Fluids (1994-present)*, 24(11):115104, 2012.
- [10] I. Chan and P. L.-F. Liu. On the runup of long waves on a plane beach. *J. Geophys. Res.-Oceans*, 117, 2012.
- [11] Y. Chou and O. Fringer. A model for the simulation of coupled flow-bed form evolution in turbulent flows. *J. Geophys. Res.-Oceans*, 115(C10), 2010.

- [12] W. O. Criminale, T. L.r Jackson, and R. D. Joslin. *Theory and computation of hydrodynamic stability*. Cambridge University Press, 2003.
- [13] M. O. Deville, P. F. Fischer, and E. H. Mund. *High Order Methods for Incompressible Fluid Flow*. Cambridge University Press, 2002.
- [14] P. J. Diamessis, J.A. Domaradzki, and J.S. Hesthaven. A spectral multidomain penalty method model for the simulation of high reynolds number localized incompressible stratified turbulence. *J. Comput. Phys.*, 202(1):298–322, 2005.
- [15] P. J. Diamessis and L. G. Redekopp. Numerical investigation of solitary internal wave-induced global instability in shallow water benthic boundary layers. *J. Phys. Oceanogr.*, 36(5), 2006.
- [16] J. A. Domaradzki, Z. Xiao, and P. Smolarkiewicz. Effective eddy viscosities in implicit large eddy simulations of turbulent flows. 15:3890–3893, 2002.
- [17] W. S. Don, D. Gottlieb, and J. H. Jung. A multidomain spectral method for supersonic reactive flows. 192:325–354, 2003.
- [18] P. G. Drazin and W. H. Reid. *Hydrodynamic stability*. Cambridge university press, 2004.
- [19] H. W. Emmons. The laminar-turbulent transition in a boundary layer-part i. *Journal of the Aeronautical Sciences*, 18(7), 1951.
- [20] F. Fedele, D. L. Hitt, and R.D. Prabhu. Revisiting the stability of pulsatile pipe flow. *European Journal of Mechanics-B/Fluids*, 24(2):237–254, 2005.
- [21] M. Gad-El-Hak, R. F. Blackwelderf, and J. J. Riley. On the growth of turbulent regions in laminar boundary layers. *Journal of Fluid Mechanics*, 110:73–95, 1981.
- [22] D. Gottlieb and J. S. Hesthaven. Spectral methods for hyperbolic problems. *J. Comput. Appl. Math.*, 128(1):83–131, 2001.
- [23] R. Grimshaw. The solitary wave in water of variable depth. part 2. *J. Fluid Mech.*, 46(03):611–622, 1971.
- [24] H. Gustavsson. Excitation of direct resonances in plane poiseuille flow. *Studies in Applied Mathematics (Malden)*, 1986.

- [25] P. Hall and K.H. Parker. The stability of the decaying flow in a suddenly blocked channel. *J. Fluid Mech.*, 75(02):305–314, 1976.
- [26] M.R. Head and P. Bandyopadhyay. New aspects of turbulent boundary-layer structure. *Journal of Fluid Mechanics*, 107:297–338, 1981.
- [27] T. Herbert. Parabolized stability equations. *Annual Review of Fluid Mechanics*, 29(1):245–283, 1997.
- [28] J. S. Hesthaven. A stable penalty method for the compressible Navier-Stokes equations: II. One-dimensional domain decomposition schemes. *SIAM J. Sci. Comput.*, 18(3):658–685, 1997.
- [29] J. S. Hesthaven and D. Gottlieb. A stable penalty method for the compressible Navier-Stokes equations: I. Open boundary conditions. *SIAM J. Sci. Comput.*, 17(3):579–612, 1996.
- [30] J. Høeppner, L. Brandt, and D. S. Henningson. Transient growth on boundary layer streaks. *Journal of Fluid Mechanics*, 537:91–100, 2005.
- [31] R.G. Jacobs and P.A. Durbin. Simulations of bypass transition. *Journal of Fluid Mechanics*, 428:185–212, 2001.
- [32] J. Jeong and F. Hussain. On the identification of a vortex. *Journal of fluid mechanics*, 285:69–94, 1995.
- [33] G. E. Karniadakis, M. Israeli, and S. A. Orszag. High-order splitting methods for the incompressible navier-stokes equations. *J. Comput. Phys.*, 97(2):414–443, 1991.
- [34] J. M. Kendall. Studies on laminar boundary-layer receptivity to freestream turbulence near a leading edge. In *Boundary layer stability and transition to turbulence*, volume 1, pages 23–30, 1991.
- [35] P. S. Klebanof. Effect of free-stream turbulence on a laminar boundary layer. In *Bulletin of the American Physical Society*, volume 16, page 1323. AMER INST PHYSICS CIRCULATION FULFILLMENT DIV, 500 SUNNYSIDE BLVD, WOODBURY, NY 11797-2999, 1971.
- [36] M.T. Landahl. A note on an algebraic instability of inviscid parallel shear flows. *Journal of Fluid Mechanics*, 98(02):243–251, 1980.

- [37] J. G. Levin, M. Iskandarani, and D. B. Haidvogel. A spectral filtering procedure for eddy-resolving simulations with a spectral element ocean model. *137*:130–154, 1997.
- [38] P. L.-F. Liu, P. Lynett, H. Fernando, B. E. Jaffe, H. Fritz, B. Higman, R. Morton, J. Goff, and C. Synolakis. Observations by the international tsunami survey team in sri lanka. *Science*, 308(5728):1595–1595, 2005.
- [39] P. L.-F. Liu and O. Orfila. Viscous effect on transient long-wave propagation. *J. Fluid Mech.*, 520:83–92, 2004.
- [40] P. L.-F. Liu, Y. S. Park, and E. A. Cowen. Boundary layer flow and bed shear stress under a solitary wave. *J. Fluid Mech.*, 574:449–463, 2007.
- [41] Y. Liu, T. A. Zaki, and P. A. Durbin. Boundary-layer transition by interaction of discrete and continuous modes. *Journal of Fluid Mechanics*, 604:199, 2008.
- [42] P. Luchini and A. Bottaro. Adjoint equations in stability analysis. *Annual Review of fluid mechanics*, 46(1):493, 2014.
- [43] J. Luo and X. Wu. On the linear instability of a finite stokes layer: Instantaneous versus floquet modes. *Phys. Fluids*, 22(5):054106, 2010.
- [44] P. A. Madsen, D. R. Fuhrman, and H. A. Schäffer. On the solitary wave paradigm for tsunamis. *J. Geophys. Res.-Oceans*, 113(C12), 2008.
- [45] M. Mazzuoli, G. Vittori, and P. Blondeaux. Turbulent spots in oscillatory boundary layers. *Journal of Fluid Mechanics*, 685:365–376, 2011.
- [46] P. Meunier, S. Le Dizès, and T. Leweke. Physics of vortex merging. *Comptes Rendus Physique*, 6(4):431–450, 2005.
- [47] M. V. Morkovin. On the many faces of transition. In *Viscous drag reduction*, pages 1–31. Springer, 1969.
- [48] K.P. Nolan and E.J. Walsh. Particle image velocimetry measurements of a transitional boundary layer under free stream turbulence. *Journal of Fluid Mechanics*, 702:215–238, 2012.
- [49] W. M. Orr. The stability or instability of the steady motions of a perfect liquid and of a viscous liquid. part ii: A viscous liquid. In *Proceedings of*

the Royal Irish Academy. Section A: Mathematical and Physical Sciences, pages 69–138. JSTOR, 1907.

- [50] S. A. Orszag. Accurate solution of the orr–sommerfeld stability equation. *J. Fluid Mech.*, 50(04):689–703, 1971.
- [51] C. E. Ozdemir, T.-J. Hsu, and S Balachandar. Direct numerical simulations of instability and boundary layer turbulence under a solitary wave. *J. Fluid Mech.*, 731:545–578, 2013.
- [52] Y. S. Park, J. Verschaeve, G. K. Pedersen, and P. L.-F. Liu. Boundary-layer flow and bed shear stress under a solitary wave: revision. *J. Fluid Mech.*, 753:554–559, 2014.
- [53] O. M. Phillips. Shear-flow turbulence. *Annual Review of Fluid Mechanics*, 1(1):245–264, 1969.
- [54] F. J. Poulin, G. R. Flierl, and J. Pedlosky. Parametric instability in oscillatory shear flows. *Journal of fluid mechanics*, 481:329–353, 2003.
- [55] S. C. Reddy, P. J. Schmid, and D. S. Henningson. Pseudospectra of the orr–sommerfeld operator. *SIAM Journal on Applied Mathematics*, 53(1):15–47, 1993.
- [56] B. Rehill, E. J. Walsh, L. Brandt, P. Schlatter, T. A. Zaki, and D. M. McEligot. Identifying turbulent spots in transitional boundary layers. *Journal of turbomachinery*, 135(1):011019, 2013.
- [57] J. J. Riley and M. Gad-el Hak. The dynamics of turbulent spots. In *Frontiers in Fluid Mechanics*, pages 123–155. Springer, 1985.
- [58] M. M. Rogers and R. D. Moser. The three-dimensional evolution of a plane mixing layer: the kelvin–helmholtz rollup. *Journal of Fluid Mechanics*, 243:183–226, 1992.
- [59] M. M. Rogers and R. D. Moser. Direct simulation of a self-similar turbulent mixing layer. *Physics of Fluids (1994-present)*, 6(2):903–923, 1994.
- [60] M. M. Sadek, L. Parras, P. J. Diamessis, and P. L.-F. Liu. Two-dimensional instability of the bottom boundary layer under a solitary wave. *Physics of Fluids (1994-present)*, 27(4):044101, 2015.

- [61] P. Scandura. Two-dimensional vortex structures in the bottom boundary layer of progressive and solitary waves. *J. Fluid Mech.*, 728:340–361, 2013.
- [62] P. Schlatter, L. Brandt, H.C. De Lange, and D. S. Henningson. On streak breakdown in bypass transition. *Physics of Fluids (1994-present)*, 20(10):101505, 2008.
- [63] P. J. Schmid. Nonmodal stability theory. *Annu. Rev. Fluid Mech.*, 39:129–162, 2007.
- [64] P. J. Schmid and D. S. Henningson. *Stability and transition in shear flows*, volume 142. Springer, 2001.
- [65] G. B. Schubauer and P.S. Klebanoff. Contributions on the mechanics of boundary-layer transition. *NACA-TR-1289*, 1956.
- [66] G. Seminara and P. Hall. Linear stability of slowly varying unsteady flows in a curved channel. *Proceedings of the Royal Society of London. A. Mathematical and Physical Sciences*, 346(1646):279–303, 1975.
- [67] S.F. Shen. Some considerations on the laminar stability of time-dependent basic flows. *AIAA Journal*, 28:397–404, 1961.
- [68] D. Sipp and L. Jacquin. Widnall instabilities in vortex pairs. *Physics of Fluids (1994-present)*, 15(7):1861–1874, 2003.
- [69] D. N. Slinn and J. J Riley. A model for the simulation of turbulent boundary layers in an incompressible stratified flow. 144:550–602, 1998.
- [70] A. Sommerfeld. Ein Beitrag zur hydrodynamischen Erklärung der turbulenten Flüssigkeitsbewegung. *Atti Congr. Int. Math. 4th*, 1908.
- [71] H. B. Squire. On the stability for three-dimensional disturbances of viscous fluid flow between parallel walls. *Proceedings of the Royal Society of London. Series A, Containing Papers of a Mathematical and Physical Character*, pages 621–628, 1933.
- [72] M. Stastna and K. G. Lamb. Vortex shedding and sediment resuspension associated with the interaction of an internal solitary wave and the bottom boundary layer. *Geophys. Res. Lett.*, 29(11):7–1, 2002.

- [73] M. Stastna and K. G. Lamb. Sediment resuspension mechanisms associated with internal waves in coastal waters. *J. Geophys. Res.-Oceans*, 113(C10), 2008.
- [74] J.C. Stettler and A.K.M. Hussain. On transition of the pulsatile pipe flow. *Journal of fluid mechanics*, 170:169–197, 1986.
- [75] B. M. Sumer, P. M. Jensen, L. B. Sørensen, J. Fredsøe, P. L.-F. Liu, and S. Carstensen. Coherent structures in wave boundary layers. part 2. solitary motion. *J. Fluid Mech.*, 646:207–231, 2010) (Referred to in text as SU10.
- [76] C. Thomas, A. P. Bassom, P.J. Blennerhassett, and C. Davies. The linear stability of oscillatory poiseuille flow in channels and pipes. In *Proceedings of the Royal Society of London A: Mathematical, Physical and Engineering Sciences*, volume 467, pages 2643–2662. The Royal Society, 2011.
- [77] S. A. Thorpe. *The turbulent ocean*. Cambridge University Press, 2005.
- [78] L. N. Trefethen. Pseudospectra of linear operators. *SIAM review*, 39(3):383–406, 1997.
- [79] L. N. Trefethen and M. Embree. *Spectra and pseudospectra: the behavior of nonnormal matrices and operators*. Princeton University Press, 2005.
- [80] L. N. Trefethen, A. Trefethen, S. Reddy, and T. Driscoll. Hydrodynamic stability without eigenvalues. *Science*, 261(5121):578–584, 1993.
- [81] C. D. Troy and J. R. Koseff. The instability and breaking of long internal waves. *J. Fluid Mech.*, 543:107–136, 2005.
- [82] N. J. Vaughan and T. A. Zaki. Stability of zero-pressure-gradient boundary layer distorted by unsteady klebanoff streaks. *Journal of Fluid Mechanics*, 681:116–153, 2011.
- [83] J. C.G. Verschaeve and G. K. Pedersen. Linear stability of boundary layers under solitary waves. *J. Fluid Mech.*, 761:62–104, 2014.
- [84] G. Vittori and P. Blondeaux. Turbulent boundary layer under a solitary wave. *J. Fluid Mech.*, 615:433–443, 2008.
- [85] G. Vittori and P. Blondeaux. Characteristics of the boundary layer at the bottom of a solitary wave. *Coast Eng.*, 58(2):206–213, 2011.

- [86] C. H Von Kerczek. The instability of oscillatory plane poiseuille flow. *Journal of Fluid Mechanics*, 116:91–114, 1982.
- [87] K. B. Winters and E. A. D' Asaro. Two-dimensional instability of finite amplitude internal gravity wave packets near a critical level. 94 no. C9:12,709–12,719, 1989.
- [88] I.J. Wygnanski and F.H. Champagne. On transition in a pipe. part 1. the origin of puffs and slugs and the flow in a turbulent slug. *Journal of Fluid Mechanics*, 59(02):281–335, 1973.
- [89] H. Yeh, M. Francis, C. Peterson, T. Katada, G. Latha, R.K. Chadha, J.P. Singh, and G. Raghuraman. Effects of the 2004 great sumatra tsunami: Southeast indian coast. *J. Waterw. Port C.-ASCE*, 133(6):382–400, 2007.
- [90] T. A. Zaki. From streaks to spots and on to turbulence: exploring the dynamics of boundary layer transition. *Flow, turbulence and combustion*, 91(3):451–473, 2013.
- [91] T. A. Zaki and P. A. Durbin. Mode interaction and the bypass route to transition. *Journal of Fluid Mechanics*, 531:85–111, 2005.
- [92] T. A. Zaki and P. A. Durbin. Continuous mode transition and the effects of pressure gradient. *Journal of Fluid Mechanics*, 563:357–388, 2006.
- [93] M. Zhao, M.S. Ghidaoui, and A.A. Kolyshkin. Perturbation dynamics in unsteady pipe flows. *Journal of Fluid Mechanics*, 570:129–154, 2007.
- [94] J. Zhou, R. J. Adrian, S. Balachandar, and T.M. Kendall. Mechanisms for generating coherent packets of hairpin vortices in channel flow. *Journal of Fluid Mechanics*, 387:353–396, 1999.